Particle-identification capability of the straw tube tracker and feasibility studies for open-charm production with PANDA

Apostolou, Alexandros

university of groningen

Particle-identification capability of the Straw Tube Tracker and feasibility studies for open-charm production with $\bar{\text{P}}$ANDA

PhD Thesis

to obtain the degree of PhD at the
University of Groningen
on the authority of the
Rector Magnificus Prof. E. Sterken
and in accordance with
the decision by the College of Deans.

This thesis will be defended in public on
Friday 6^{th} of April 2018 at 14:30 hours

by

Alexandros Apostolou
born on 21^{st} of September 1985
in Thessaloniki, Greece

Supervisors
Prof. N. Kalantar-Nayestanaki
Prof. J. Ritman

Co-supervisors
Dr. J.G. Messchendorp
Dr. P. Wintz

Assessment committee
Prof. A. van den Berg
Prof. P. Salabura
Prof. X. Shen

ISBN: 978-94-034-0497-4 (Printed version)
ISBN: 978-94-034-0498-1 (Electronic version)

Printing and layout by: ProefschriftMaken —— www.proefschriftmaken.nl

To my father

There are men who struggle for a day and they are good.
There are men who struggle for a year and they are better.
There are men who struggle for many years, and they are better still.
But there are those who struggle all their lives:
These are the indispensable ones.

- B. Brecht -

Contents

Chapter 1

Preface

Since at least 2500 years ago, mankind has started to ask questions about nature and how it works. Through the years, this general questioning has been more precisely expressed at which fundamental forces exist, what are the underlying processes and the elements from which everything is made. In order to give solid answers to the questions mentioned above, one should study the inner structure of the objects composing the matter. A major breakthrough in the study of matter happened already more than 100 years ago, when Thompson discovered the electron. Soon after, Rutherford, with his famous scattering experiment, set the basis for the knowledge of the lightest atom, and a few years later, Bohr, proposed the model of the atom which remains to be part of the accepted fundamental concept of nuclear physics.

Until about 80 years ago, protons, electrons and neutrons were considered to be the most fundamental particles in universe. However, this changed in the 1960's, when quarks were introduced as the smallest massive particles which make up matter. This was the breakthrough point for the establishment and development of the theory describing the elementary particles in the universe, which is called the modern theory of the Standard Model (SM).

Currently, many years after the discovery of the quarks and the formulation of the SM, the research for understanding the interactions of the particles and at the same time the search for new particles is more exciting than ever. It is widely accepted within the scientific community, that even though the SM can successfully describe many physics phenomena, it cannot describe various highly complex, self-interacting systems. The proton and neutron, the building elements of nuclei, are key examples of such systems. In order to be able to interpret these systems and formulate theoretical models, extensive measurements of composite particles, such as hadrons, have to be performed.

Today, these measurements take place in large-scale experiments using sophisticated machines, which are able to detect various types of radiation, reconstruct the composite particle of interest, study their properties and decay processes with the goal to provide sensitive information to reveal their nature.

The antiProton ANnihilation in DArmstadt ($\bar{\text{P}}$ANDA) experiment, which is being set up in Darmstadt, Germany, is a state-of-the-art experiment for hadron physics. It is part of the larger Facility for Antiproton and Ion Research (FAIR) project, which will cover a broad range in physics. The focus of the $\bar{\text{P}}$ANDA experiment is hadron physics, with the goal to give answers to many open questions about strong interactions and physics described by Quantum ChromoDynamics (QCD). It will operate at a center-of-mass energy up to $\sqrt{s} = 5.5$ GeV, with antiprotons annihilating on a proton or nuclear target. The uniqueness of $\bar{\text{P}}$ANDA will offer opportunities for unprecedented studies of bound states of particles, such as mesons and baryons, especially in the charm and open-charm sector. Of particular interest are the open-charm mesons, bound states of a charm and a light (up, down or strange) quark. Several of these states have been predicted and discovered, but there are many of them which have been predicted but not discovered, or vice versa. Moreover, there are still many open questions about the dynamics of such systems, their excitation states as well as their masses and widths. $\bar{\text{P}}$ANDA will be able to produce an abundance of open-charm states, which together with the sophisticated detector system and the high-resolution antiproton beam, will allow for extensive and precise measurements.

In the energy range in which $\bar{\text{P}}$ANDA will operate, the physics signatures of interest are mixed with a large number of background processes, since they both have the same signature. For this reason, the ability to distinguish signal events out of this huge background is of crucial importance. The tools needed are a sophisticated detector system together with a novel and flexible data acquisition system. There are several sub-detectors in the $\bar{\text{P}}$ANDA experiment, each one playing an important role in the detection of the event topologies of interest. Tracking detectors will perform vertex and track reconstruction of the particles, electromagnetic calorimeters will measure the energy deposition of neutral particles, and muons will be detected by the corresponding detectors. One of the main tracking detectors is the Straw Tube Tracker (STT), a cylindrical-shaped detector consisting of gas-filled tubes. It surrounds the interaction point, and its main tasks are the track reconstruction of charged particles, thereby determining their momenta, and the Particle IDentification (PID).

This thesis presents the first tests performed with a prototype STT detector in order to investigate the performance for both track reconstruction and PID as well as to eventually decide upon the readout of the detector. In addition, Monte Carlo (MC) simulations are presented that were performed to investigate the ability of $\bar{\text{P}}$ANDA to measure open-charm reactions in proton-antiproton annihilation reactions.

The structure of the thesis is as follows:

In chapter 2, the SM is outlined. In addition, a general overview of the QCD is given together with theoretical models describing the open-charm production and the dynamics of these states.

Chapter 3 is devoted to the description of the FAIR facility and the $\bar{\text{P}}$ANDA physics program. A detailed overview of the detector system is also given.

In chapter 4, two different tests performed with a prototype STT are presented. Experimental setup, readout concept, results and conclusions along with a discussion are included.

Chapter 5 includes the analysis of the process $\bar{p}\,p \rightarrow D^0\,\overline{D}^0 \rightarrow \pi^+K^-\pi^-K^+$ in $\bar{\text{P}}$ANDA. The results of the MC simulation are shown. The analysis uses both inclusive (single D meson) and exclusive (D meson pair) reconstruction of the final state. Background studies are also present.

Finally, chapter 6 concludes the work of this thesis, summarizes the results and includes an outlook.

Chapter 2

The structure of charmed hadrons from a theoretical perspective

QCD is generally considered to be the theory that can describe the physical phenomena of the strong interactions very well at high energies. However, there are many open questions in the low-energy regime, where perturbation methods do not work, in contrary to the high-energy regime where asymptotic freedom is dominant. The quark model, which can explain most of the established and discovered states of particles, cannot explain many states found in the charm sector.

As an example, figure 2.1 shows the mass spectrum of the open-charm meson (D_s) candidates with the predictions of two relativistic quark models from two groups, Godfrey and Igsur [1] and Di Pierro and Eichten [2]. One may notice that the quark model describes the masses of the two lowest-lying states rather well and the predictions made are correct. For states with larger masses, the theoretical predictions are far from the experimentally measured values. Therefore, it is obvious that there are still open questions about the dynamics of these open-charm (heavy-light) systems. Moreover, at present, the lifetimes of many of these states are not well determined. Measuring the natural width with high precision, will allow us to test particular models, and thereby, get an insight to the structure of these states. Thus, the production and the high-precision measurement of the widths, is the key to unlock the mystery of the open-charm states.

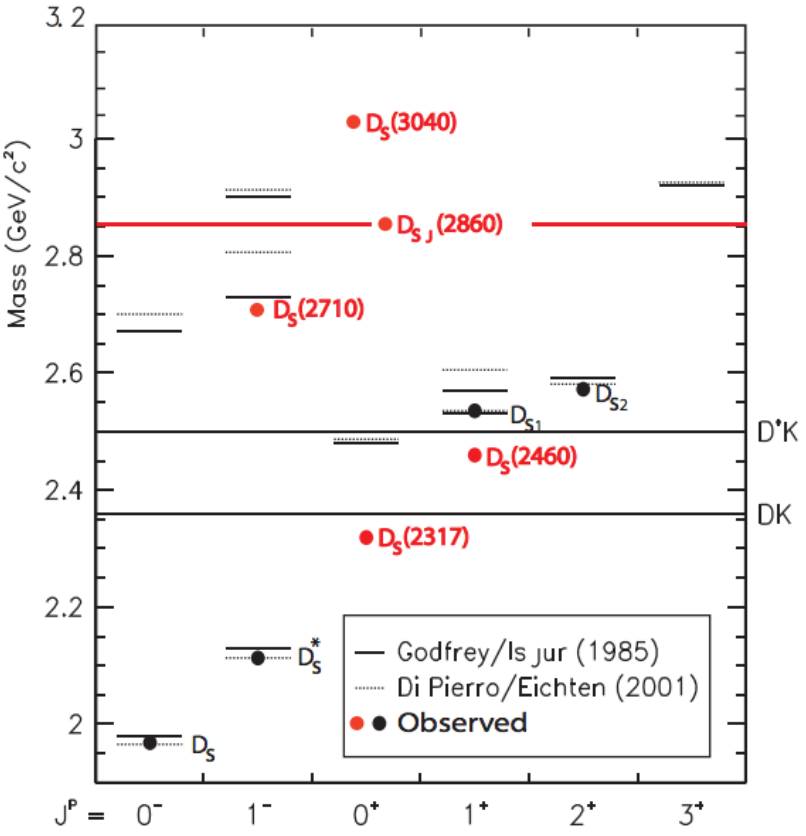

Figure 2.1: D_s spectrum predicted by two different quark models. Black dots refer to old measured states and red dots to newly discovered. For mesons with a larger mass (around and above the DK - or the D^+K - thresholds, which are shown with the black horizontal lines), the theoretical predictions of the quark models do not match the measured experimental values [3].

Experiments using $p\bar{p}$ annihilations are very well suited to carry out precision studies of the masses and width of the open-charm states. The precondition is, however, that these states are produced in abundance. At present, the production cross section of open-charm states in $p\bar{p}$ has not been measured yet and, from a theoretical perspective, the production dynamics are not very well understood. In particular, a model-independent approach, e.g. based on first principles, is only capable of making predictions on the mass spectrum, but not on the production dynamics in $p\bar{p}$ annihilation. There are various approaches and models that attempt to describe the production and structure of open-charm mesons. This chapter will review various theoretical approaches that are capable of making predictions for the open-charm production. Moreover, we discuss the

ab-initio approach based on Lattice Quantum ChromoDynamics (LQCD) which leads to promising predictions of the mass spectrum of heavy-light systems that go beyond the naive quark model. In the next two sections, the SM of particle physics is briefly described followed by a short reference to the basics of the QCD. In section 2.3, an extensive description of a theoretical model describing the meson-baryon dynamics and providing predictions for the production cross section of D mesons is presented. The last part of this chapter describes LQCD calculations that are deployed to make rigorous predictions of the masses and widths of open-charm states.

2.1 The SM of particle physics

The theoretical model summarizing the fundamental particles and describing their interactions in the universe is called the SM. It combines three main parts: the fundamental forces, the exchange particles which mediate these forces and the elementary particles themselves. The SM includes three fundamental forces: the weak, the electromagnetic and the strong force. The first two combined are described by the ElectroWeak Theory (EWT), while the theory describing the strong interactions of the particles is called QCD.

Figure 2.2 shows the SM particles, which include fermions with spin 1/2, bosons with spin 1 and the Higgs boson (spin 0). The fermions are divided into two categories: the leptons and the quarks. There are in total 18 particles in the SM together with their corresponding anti-particles and in the case of the quarks, their color-charge partners. The leptons are elementary particles with integer electric charge. They only interact through weak and electromagnetic interactions (neutrinos only through the weak force). There are three lepton flavors that come in doublets, which form the three generations. The first one includes the electron (e) and the corresponding electron neutrino (ν_e), the second generation includes the muon (μ) and the muon neutrino (ν_μ) and the third includes the tau (τ) and the tau neutrino (ν_τ). On the other hand, the quarks, which have a fractional electrical charge in units of 1/3e, interact via all three forces, including the strong force. The quarks carry a so-called color charge, usually labeled as red, green, blue. There are six quark flavors divided into three generations of quarks. In the first generation, one can find the nearly massless up and down quarks (u,d), in the second the charm and strange quarks (c,s) and in the third, the top and the bottom quarks (t,b). The charm, top and bottom quarks, are considered the "heavy" quarks, due to their large mass (> 1 GeV/c^2).

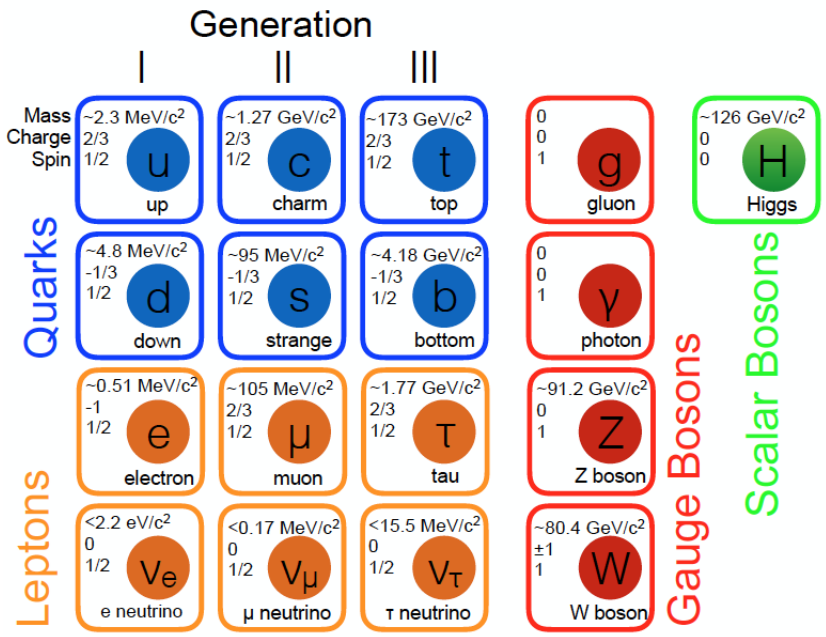

Figure 2.2: The particles in the Standard Model: Leptons, quarks, gauge bosons and the Higgs boson are included.

The gauge bosons, are the mediators of the interactions between the particles. The photons (γ) are particles with zero mass and mediate the electromagnetic interactions between the electrically-charged particles. The weak interaction is mediated by the heavy W^+, W^- and Z^0 bosons. The gluons, similar to photons, are massless particles, which mediate the strong interaction between color-charged particles. The gluons have a unique feature; they can interact with each other. Another boson is the Higgs boson (H), a spin-less particle with a mass of approximately 125 GeV/c^2. The Higgs boson plays a very important role in the SM since it mediates the Higgs field which is the source of the mass generation of the fundamental particles in the SM. The existence of the Higgs particle was predicted more than 50 years ago [4–6] and it was discovered recently by two experiments operating at the Large Hadron Collider (LHC) in Switzerland [7–9]. The discovery of the Higgs boson, lead to the Nobel Prize to the two main authors of references [4, 5], P. Higgs and F. Englert in 2013. Quarks can only appear in color-neutral combinations, also known as hadrons. The phenomena that excludes hadrons (or any other composite particle) to carry a color is called (color) confinement [10–13], which also lead to a Nobel prize in 2004. Figure 2.3 shows some of the bound states of quarks and gluons as predicted by QCD.

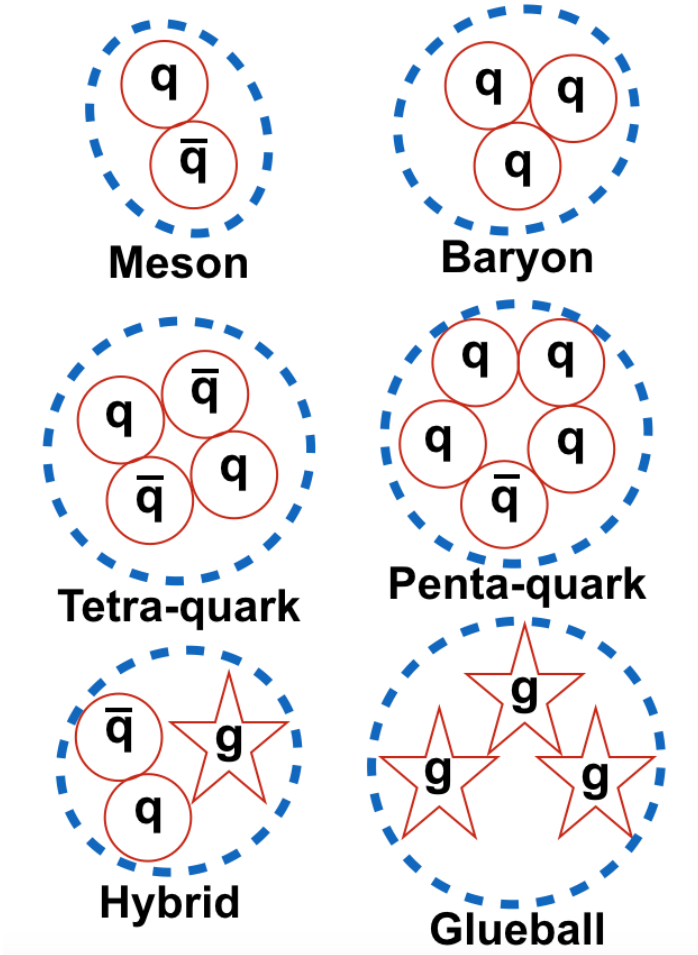

Figure 2.3: Possible bound states predicted by QCD. All these states can be found in a color-neutral configuration, obeying the confinement rule of QCD.

The two simplest states are well established and studied. These are the mesons, which consist of a quark and an anti-quark pair, and the baryons, states with three quarks. The confinement of QCD allows for the existence of other states composed of 4 or 5 quarks, as well as states which consist only of gluons, the glueballs, and states consisting of a gluon and a quark-antiquark pair, which are hybrids. There are several tetraquark, pentaquark and glueballs candidates observed by experiments, but they are not firmly and unambiguously understood yet. Mesons (π, K, etc.) and baryons (p, n, etc.) are often called "ordinary" matter, while glueballs and hybrids are labelled as "exotic" matter.

2.2 Theoretical approach of QCD

QCD is the SU(3) gauge field theory of the strong interaction. The concept of QCD is based on the interactions between quarks and gluons according to the laws of non-abelian strong fields between the color charges.

The equation describing QCD is given by the gauge-invariant QCD Langrangian

$$\mathcal{L} = \bar{\psi}_q^i (i\gamma^\mu)(D_\mu)_{ij}\psi_q^j - m_q \bar{\psi}_q^i \psi_{qi} - \frac{1}{4} F_{\mu\nu}^a F^{a\mu\nu}, \tag{2.1}$$

where ψ_q^i denotes a four component Dirac spinor with color index i, γ^μ is a Dirac matrix that expresses the vector nature of the strong interaction, μ is a Lorentz vector index, m_q is the quark mass, $F_{\mu\nu}^a$ is the tensor of the gluon field for a gluon with color a, and D_μ is the covariant derivative in QCD,

$$(D_\mu)_{ij} = \delta_{ij}\partial_\mu - i g_s t_{ij}^a A_\mu^a, \tag{2.2}$$

with g_s the strong coupling (related to coupling constant α_s by $g_s^2 = 4\pi\alpha_s$), A_μ^a the gluon field with color index a, and t_{ij}^a is proportional to the Hermitian and traceless Gell-Mann matrices of SU(3)[1]. The first term in equation 2.1 corresponds to the kinetic energy of the quarks and the dynamics between quarks and gluons. The second term holds the information for the masses of the fermions while the third term corresponds to the gauge-invariant term describing the dynamics of the massless gluon fields.

QCD has two very specific properties, the asymptotic freedom and the color confinement. These two properties characterize and determine the behavior of quarks and gluons in particle reactions at all energy scales. QCD is well established at high energies, where the strong coupling constant is very small, and, therefore, perturbative methods can be applied leading to an accurate description of interactions. On the other hand, in the low energy regime, QCD is not well understood. This is due to the non-abelian property of QCD which makes a

[1]The Gell-Mann matrices in the conventional representation are:

$$\lambda^1 = \begin{pmatrix} 0 & 1 & 0 \\ 1 & 0 & 0 \\ 0 & 0 & 0 \end{pmatrix}, \ \lambda^2 = \begin{pmatrix} 0 & -i & 0 \\ i & 0 & 0 \\ 0 & 0 & 0 \end{pmatrix}, \ \lambda^3 = \begin{pmatrix} 1 & 0 & 0 \\ 0 & -1 & 0 \\ 0 & 0 & 0 \end{pmatrix}, \ \lambda^4 = \begin{pmatrix} 0 & 0 & 1 \\ 0 & 0 & 0 \\ 1 & 0 & 0 \end{pmatrix}$$

$$\lambda^5 = \begin{pmatrix} 0 & 0 & -i \\ 0 & 0 & 0 \\ i & 0 & 0 \end{pmatrix}, \ \lambda^6 = \begin{pmatrix} 0 & 0 & 0 \\ 0 & 0 & 1 \\ 0 & 1 & 0 \end{pmatrix}, \ \lambda^7 = \begin{pmatrix} 0 & 0 & 0 \\ 0 & 0 & -i \\ 0 & i & 0 \end{pmatrix}, \ \lambda^8 = \begin{pmatrix} \frac{1}{\sqrt{3}} & 0 & 0 \\ 0 & \frac{1}{\sqrt{3}} & 0 \\ 0 & 0 & \frac{-2}{\sqrt{3}} \end{pmatrix}$$

perturbative approach impossible at large-distance scales or low energies. Thus, the strength of the interactions among quarks and gluons is energy (or distance) dependent. One fundamental parameter of the QCD is the coupling constant α_s. The coupling constant depends on the energy scale (or the momentum transfer Q) and can be expressed by the following equation:

$$\alpha_s(Q^2) = \frac{1}{b_0 \ln \frac{Q^2}{\Lambda^2}}, \tag{2.3}$$

where Λ is the QCD scale ($\sim$ 200 MeV) and represents the scale at which QCD can be considered as a perturbative theory, b_0 is a factor depending on the number of quarks and gluons in the interaction and Q is the energy scale.

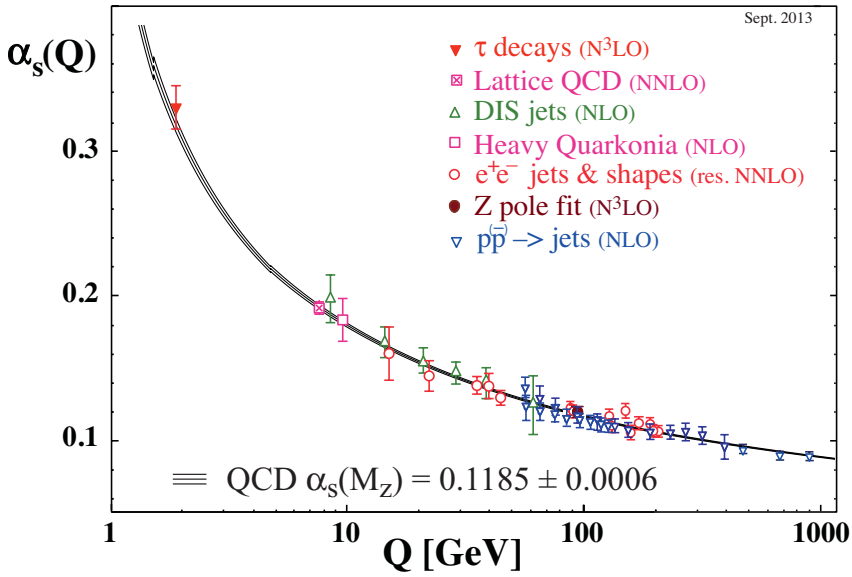

Figure 2.4: The QCD running coupling constant The QCD running coupling constant as a function of the momentum transfer Q. The data points represent the values extracted from different Effective Field Theory (EFT) approaches. The black line is a fit to the data points, the width of which represents the uncertainty [14].

Figure 2.4 shows the running of the coupling constant as a function of the energy scale. Usually, α_s is evaluated at the scale of the mass of the Z boson, $M_Z = 91.2$ GeV/c^2. It can be seen that for high energies, the strength becomes small (asymptotic freedom) and the opposite happens for low energies, especially below the Λ scale (color confinement). The non-perturbative region of the QCD corresponds to the region where the formation of the hadrons (such as protons and neutrons) takes place. Hence, hadron physics is primarily focused

towards the non-perturbative region. The study of charm-rich mesons and their excitations will allow a systematic study and give answers to the open questions regarding this region.

2.3 Meson-baryon dynamics in the nucleon-antinucleon system

In this section, a theoretical approach describing the nucleon-antinucleon interaction is presented [15–22]. The basis of this approach is the Bonn meson exchange model for the nucleon-nucleon interaction [23]. Although this meson-baryon-exchange model is able to describe the production of several mesons and baryons, for the scope of this thesis only the production of D mesons from a proton-antiproton interaction will be discussed.

The starting point of the model, is the total Hamiltonian written as the sum of the free Hamiltonian H_0 and an interaction term W

$$H = H_0 + W, \tag{2.4}$$

with the free Hamiltonian as

$$H_0 = \sum_{\alpha\beta\gamma} (E_\alpha \alpha_\alpha^\dagger \alpha_\alpha + \omega_\gamma b_\gamma^\dagger b_\gamma + E_\beta \bar{\alpha}_\beta^\dagger \bar{\alpha}_\beta + \omega_\gamma \bar{b}_\gamma^\dagger \bar{b}_\gamma), \tag{2.5}$$

and the interaction term with the generalized form

$$\begin{aligned} W = \sum_{\alpha\beta\gamma} (&W_{\alpha\beta\gamma} \alpha_\alpha^\dagger \alpha_\beta b_\gamma + W_{\alpha\beta\gamma} \bar{\alpha}_\alpha^\dagger \bar{\alpha}_\beta b_\gamma + W_{\alpha\beta\gamma} \alpha_\alpha^\dagger \bar{\alpha}_\beta^\dagger b_\gamma + \\ &W_{\alpha\beta\gamma} \bar{\alpha}_\alpha \alpha_\beta b_\gamma) + h.c. + (b_\gamma \to \bar{b}_\gamma). \end{aligned} \tag{2.6}$$

In these equations, α_α, $\bar{\alpha}_\alpha$ are the operators for the baryon and anti-baryon, b_γ, $\bar{b}_\gamma$ for the meson and anti-meson, and E, ω are the kinetic energies of baryons and mesons respectively. The notation α, β, and γ refers to the first baryon, second baryon and (exchange) meson, respectively. In the case of the production of D mesons from the proton-antiproton interaction, the exchange particle is not a meson, but a baryon. The sum in both equations (2.5 and 2.6) runs over all quantities describing the system, i.e., the spin, momentum, isospin and type of particle.

The next step is the calculation of the amplitudes of the interaction studied based on the Hamiltonian of equation 2.4 which will include the scattering amplitude and the annihilation amplitude.

Both are found by the following equations:

$$T^{\bar{N}N,\bar{N}N} = V^{\bar{N}N,\bar{N}N} + V^{\bar{N}N,\bar{N}N} G^{\bar{N}N} T^{\bar{N}N,\bar{N}N}, \tag{2.7}$$

$$T^{\bar{D}D,\bar{N}N} = V^{\bar{D}D,\bar{N}N} + V^{\bar{D}D,\bar{N}N} G^{\bar{N}N} T^{\bar{N}N,\bar{N}N}, \tag{2.8}$$

where T stands for the amplitudes, V for the potential and G is the Green's function of the particles. The second equation, which includes both the transition and the initial-state interaction, is a Distorted Wave Born Approximation (DWBA) applied to the model. In the case of the annihilation to D mesons, one has to take into account the final-state interaction of the mesons, since the mass of the D meson is significantly larger than that of the proton. For this reason, equation 2.8 has to be modified into the following (this is not needed if for example the annihilation is to two kaons):

$$T^{\bar{D}D,\bar{N}N} = (T^{\bar{D}D,\bar{D}D} G^{\bar{D}D} + 1) V^{\bar{D}D,\bar{N}N} (1 + G^{\bar{N}N} T^{\bar{N}N,\bar{N}N}). \tag{2.9}$$

The $V^{\bar{N}N,\bar{N}N}$ potential consists of an elastic part and an annihilation part. The elastic part can be obtained from a G-parity transformation of a one-boson-exchange NN potential (extension of the original Bonn model, for details see [24]) while the annihilation part is an optical potential of Gaussian form

$$V_{opt}^{\bar{N}N,\bar{N}N} = (U_0 + iW_0) e^{-\frac{r^2}{2r_0^2}}. \tag{2.10}$$

The values of the parameters of the optical potential (r_0, W_0 and U_0) are obtained by a fit to nucleon-antinucleon data obtained from experiments in the energy range relevant for the reaction.

The transition potential $V^{\bar{D}D,\bar{N}N}$ (see figure 2.5) has the general form

$$V^{\bar{D}D,\bar{N}N} \sim \sum_{Y=\Lambda_c,\Sigma_c} \frac{f_{YND}^2 F_{YND}^2}{\omega_D(\sqrt{s} - E_N - \omega_D - E_Y)}, \tag{2.11}$$

where f_{YND} stands for the coupling constant, F_{YND} for the form factor and $\sqrt{s}$, E_N, ω_D, E_Y is the center-of-mass energy, the energy of nucleon, D meson and

exchange baryon, respectively. The form factors enter the potential to account for the effects from the extended hadron structure in addition to the point-like vertices, and are parametrized in the following way

$$F_{YND} = \left(\frac{\Lambda^4 + m^4}{\Lambda^4 + k^4} \right), \tag{2.12}$$

where k and m are the four momentum and the mass of the exchange baryon, respectively, while Λ is the cut-off mass depending on the baryon type. The value of the cut-off mass is obtained (like the parameters of the optical potential in equation 2.10) from a fit to nucleon-antinucleon data.

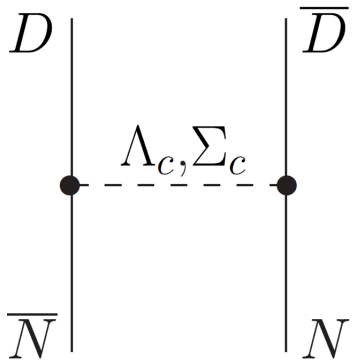

Figure 2.5: Feynman diagram for the $N\bar{N} \to D\bar{D}$ via the exchange of charmed baryons.

Figure 2.6, shows the cross section of the reaction $p\bar{p} \to D\bar{D}$ obtained from the model as described earlier. Figure 2.7 shows the complete set of diagrams that are accounted for including the ones with an intermediate $\psi(3770)$ resonance, as well as those when the coupling to $D_s^+ D_s^-$ is included without the presence of a $\psi(3770)$ resonance. In figure 2.8, the contribution of the intermediate $\psi(3770)$ resonance is demonstrated. This resonance is seen as a pronounced structure in e^+e^- experiments. Moreover, its mass is located only 35 MeV/c^2 above the $D\bar{D}$ production threshold and it has a favourable decay to $D\bar{D}$ with a branching fraction in the order of 93%. An increase on the cross section is seen especially for excess energies more than 100 MeV above the $D\bar{D}$ production threshold. The cross section values obtained from the meson-baryon exchange model is in the order of 30-40 nb, while when the intermediate $\psi(3770)$ resonance is included the values increase to 30-120 nb with a pronounced resonance behavior. Thus, the contribution of the resonance is in the order of 80 nb, depending on the excess energy above the $D\bar{D}$ threshold.

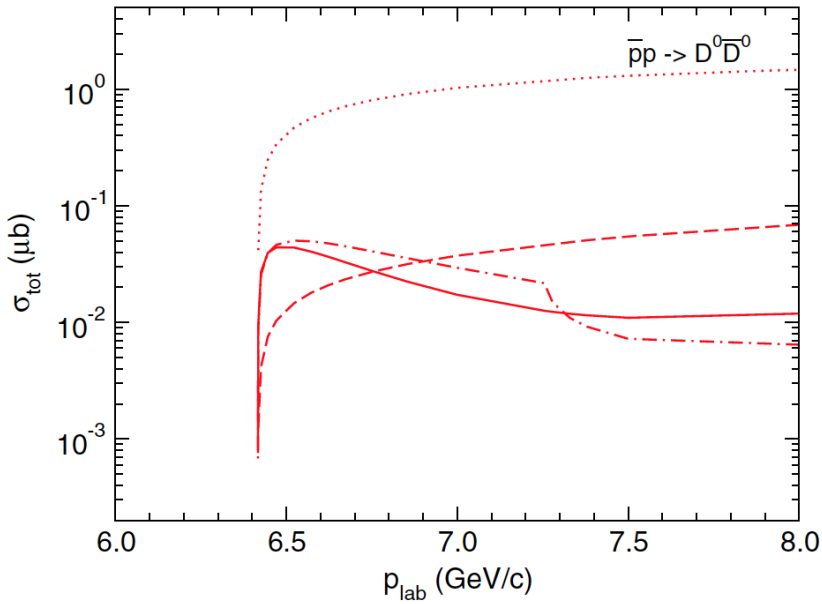

Figure 2.6: Total cross section for the $p\bar{p} \to D\bar{D}$ reaction using a meson-baryon exchange model. The dotted line represents the result obtained from a first-order Born approximation. The dashed line is the DWBA excluding final state interaction, while the solid line represents the same result including the final-state interaction. The dashed-dotted line includes the coupling of $D\bar{D}$ to $D_s^+ D_s^-$, where threshold effects due to the larger mass of D_s^+ and D_s^- are visible [22].

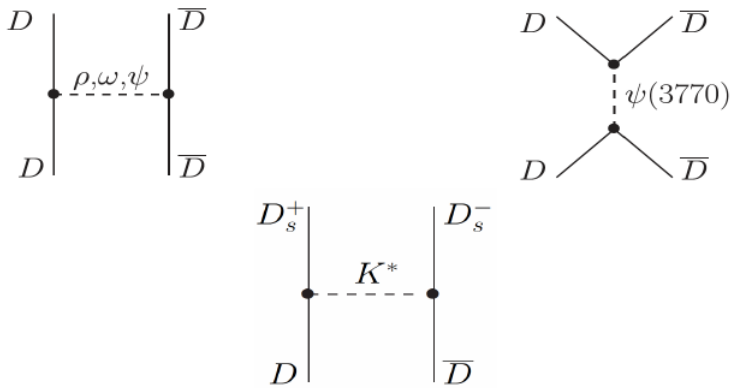

Figure 2.7: Diagrams of various final-state interaction contributions. Upper left: Including final-state interaction with a meson present. Upper right: Including final-state interaction with a $\psi(3770)$ resonance present. Lower: Including coupling to $D_s^+ D_s^-$ without the presence of a $\psi(3770)$ resonance.

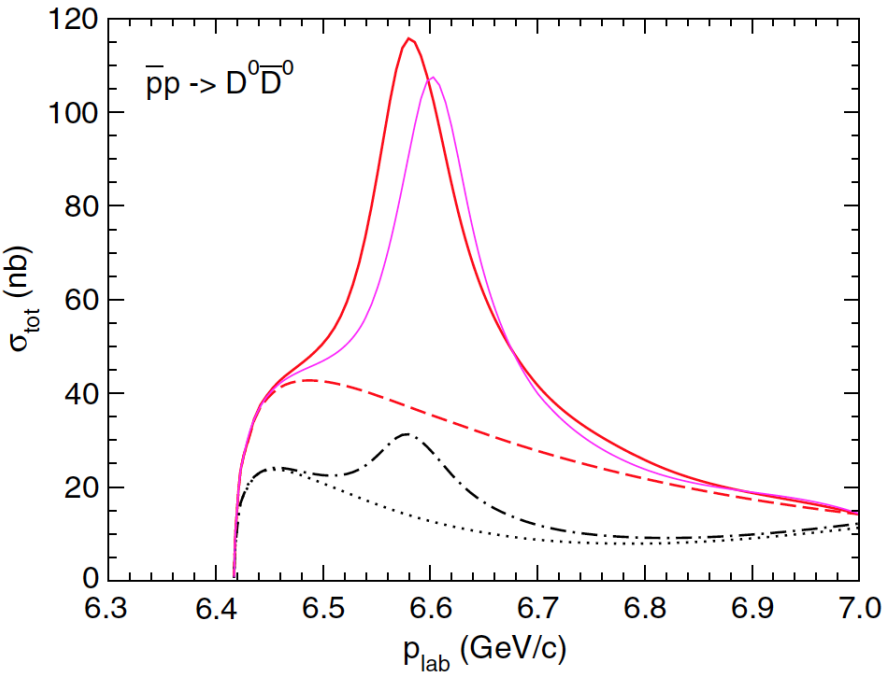

Figure 2.8: Total cross section for the $p\bar{p} \to D\bar{D}$ reaction with the inclusion of an intermediate $\psi(3770)$ resonance using a meson-baryon exchange model. The dashed line is the same as the solid line in figure 2.6. The solid red line refers to the cross section when the $\psi(3770)$ is taken into account. The magenta colored line shows the cross section when the final-state interaction is fitted to a higher $\psi(3770)$ mass of 3779 MeV/c^2, due to the uncertainties in its mass and width. The black lines represent results for the cross section (the dotted line without and the dashed-dotted line with a $\psi(3770)$ resonance present) using a different variant of the elastic part of the $V^{\bar{N}N,\bar{N}N}$ potential in the initial-state interaction [25].

It is important to mention here that there are a few other models that provide a calculation of the cross section of the $p\bar{p} \to D\bar{D}$ reaction. One of these models is based on a quark-gluon string model where the strong baryon-meson coupling constants are calculated from QCD light cone sum rules [26]. Figure 2.9 shows the calculated cross section as a function of the antiproton momentum in the lab frame. The obtained cross section of this model is in the order of 100 nb, which is larger than the one in the meson-baryon exchange model. The meson-baryon model assumes an SU(4) symmetry, which is - as is well known - not very realistic, however it accounts for final-state interactions. On the other hand, the quark-gluon string model is based on a SU(3) symmetry, which is rather well tested, but does not consider final-state interactions. It is clear that each of these models gives significantly different results which shows that the dynamics behind the open-charm production is not very well understood.

P̄ANDA can shed light on the questions related to open-charm physics, since it will use $p\bar{p}$ interactions, which will allow for the production of an abundance of open-charm states. By measuring the cross sections and confronting them with the predictions from the various models, one can learn a lot about them. Last but not least, as shown in figure 2.9, the cross section value of the reaction $p\bar{p} \to D^0\bar{D}^0$ is 4-5 orders of magnitude higher than the one for the $p\bar{p} \to D^+D^-$ reaction. This is the reason behind the selection and study of the $D^0\bar{D}^0$ pair in chapter 5 of this thesis, since in "phase-1" period of P̄ANDA we will have a limited luminosity, and, therefore, it is more advantageous to look at this stage for channels with the highest cross section.

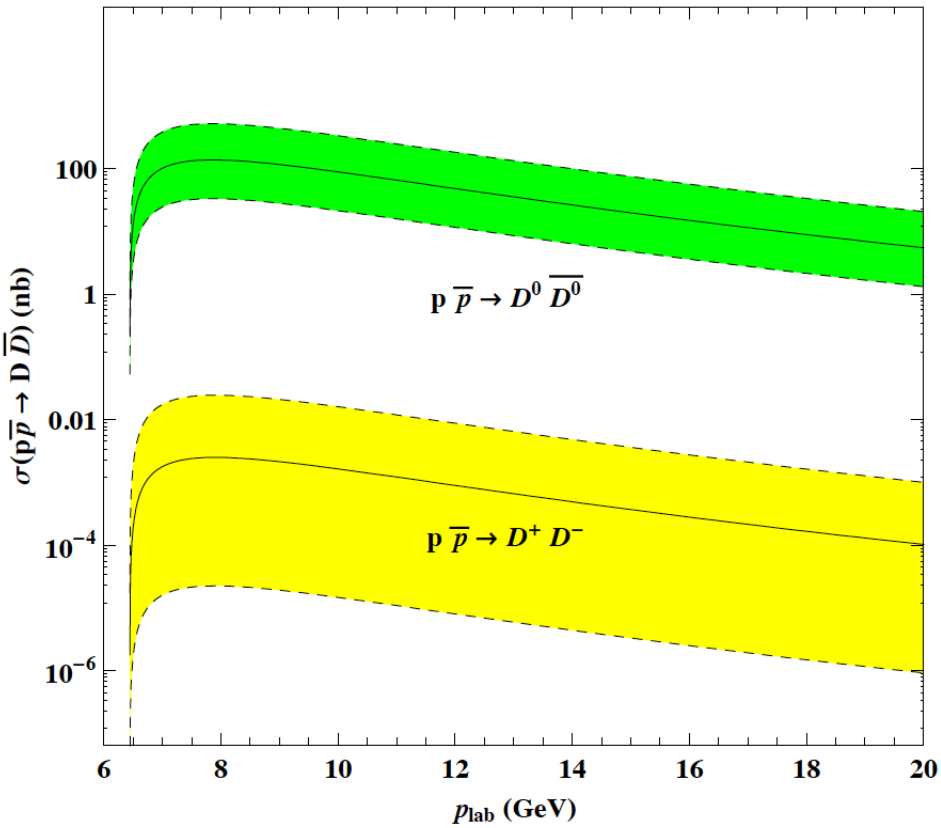

Figure 2.9: Total cross section for the $p\bar{p} \to D\bar{D}$ reaction using a quark-gluon string model. The dashed lines show the uncertainties introduced by the strong coupling constants obtained from QCD light-cone sum rules [26].

2.4 Lattice QCD

LQCD was first proposed by K. Wilson [27] and presently, it is widely used for QCD calculations. It is a non-perturbative numerical method to study QCD at low energies, where the strong coupling constant $a_s \approx 1$ and the perturbative methods are not valid anymore. LQCD is formulated in a discrete space-time lattice where the parameters that can be tuned are the strong coupling constant a_s and the bare masses of the quarks [28]. As in every quantum field theory, the interactions of the particles in QCD are described by a Lagrangian (see equation 2.1). In LQCD calculations, the main goal is to quantize the Lagrangian, which is done by calculating the Feynman's path integral. In principle, this calculation should be done in the continuous space-time, but unfortunately this is not possible. For this reason, one must break up the space-time into a 4-dimensional grid of points (a lattice), and calculate the integral. The first step is to express the quantity of interest as the matrix element of an operator, $\boldsymbol{\mathcal{O}}$, which will be the product of the quark and gluon fields. This can be done by using the Euclidean space [28, 29]

$$\langle 0|\boldsymbol{\mathcal{O}}|0\rangle = \int [d\psi]\,[d\bar{\psi}]\,[dA_\mu]\,\boldsymbol{\mathcal{O}}[\psi,\overline{\psi},A]e^{-S}\int [d\psi]\,[d\bar{\psi}]\,[dA_\mu]e^{-S}, \tag{2.13}$$

where S is the QCD action in the 4-dimensional space-time, given as:

$$S = \int \mathcal{L}\, d^4x, \tag{2.14}$$

where $\mathcal{L}$ is the Lagrangian.

Equation 2.13 integrates over all quark and gluon fields values (ψ and A) at every point in space-time. The calculation of the integral is not possible in the continuous space-time and thus, the number of space-time points has to be finite. In this way, the continuous space-time (x,t) converts to a 4-dimensional grid, (x_i,t_i) or (an_i,an_t) where a is called lattice spacing (see figure 2.10). The quark fields are then defined at the lattice sites $\psi(x,t) \rightarrow \psi(n_i,n_t)$. The fields of the Lagrangian are replaced with fields at the lattice sites and the derivatives are replaced with finite differences of these fields. The calculation of the Lagrangian over the whole space-time is now a sum over all lattice sites: $\int d^4x \rightarrow \sum_n a^4$. The lattice Lagrangian only matches the continuous space-time Lagrangian at $a = 0$. At any non-zero a point, there are additional terms in the lattice Lagrangian which are proportional to powers of a.

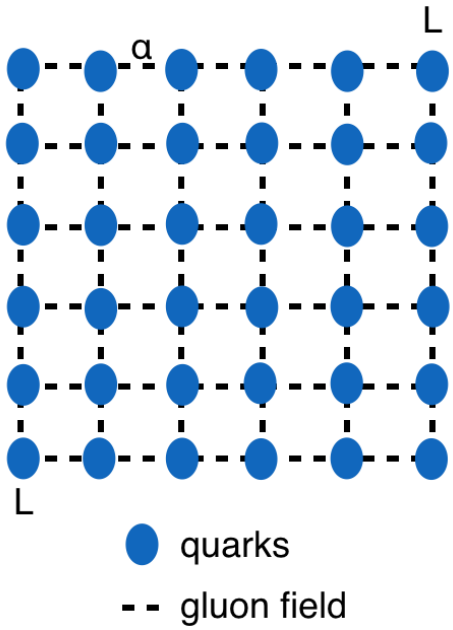

Figure 2.10: The lattice QCD plaquette shown in a 2D representation.

The role of the gluon field is to transport the color, and thus, in the lattice, the gluon fields are located on the links connecting the quarks fields as shown in figure 2.10. The gluon field is also expressed differently on the lattice compared to the continuous space-time. The lattice gluon field, $U_\mu(n_i, n_t)$, where μ reflects the direction of the quark field, and n_i, n_t refer to the starting lattice point, is related to the gluon field as follows

$$U_\mu = e^{iagA_\mu}, \tag{2.15}$$

where A_μ is the gluon field, a is used to make it dimensionless and the coupling g is used by convention. This form of a gluon field preserves the local gauge invariance. The gluonic action of the lattice, which is derived from the continuous space-time QCD action, is called Wilson plaquette action and it is calculated as follows

$$S_{\text{latt}} = \beta \sum_p \left(1 - \frac{1}{3}\Re\{Tr(U_p)\}\right); \quad \beta = \frac{6}{g^2}. \tag{2.16}$$

Here, U_p is the closed 1×1 loop formed by multiplying four gluon links together and $\Re\{Tr\}$ is the real part of the trace.

For performing LQCD calculations, fast computational tools are needed. The steps to perform the calculations are the following: the gluon fields are generated which will subsequently allow to calculate the quark propagators for each of the gluon configurations. The obtained quark propagators are combined in all possible combinations to form the hadronic correlators. These calculations are performed several times so that the continuous space-time limit is reached. The extraction of the hadron masses is performed by fitting the correlators to their experimental values. The results are then transformed to physical quantities (e.g. mass differences) to compare with the experimental values. Next, the pion mass is calculated, which is used as a substitute to the light quark masses. Due to the long time needed for the calculations, an un-physically large mass is used. The calculations have to be performed several times with different lattice spacing, in order to make sure that there are independent of α. The smaller the spacing, the more steps are needed and thus, the slower the calculation. Figures 2.11 and 2.12 show one of the latest QCD predictions for the masses of the D- and D_s- meson spectrum, respectively [30].

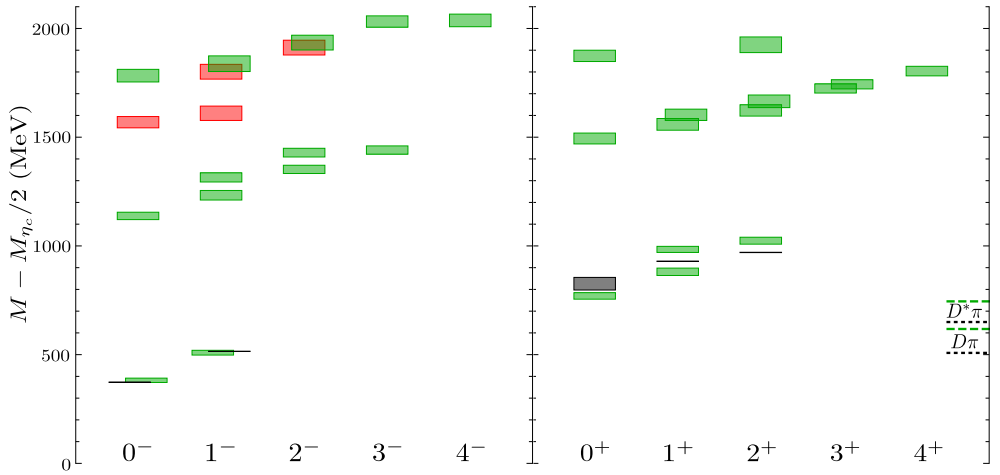

Figure 2.11: D meson spectrum predicted by LQCD. Left and right panels show the negative and positive parity states, respectively. Red and green boxes are the masses computed from the LQCD calculations. Red shows states identified as the lightest hybrid multiplets and green as the lightest conventional multiplets. Black boxes/lines are the experimental values from the PDG tables. The vertical size of the boxes indicates the 1σ statistical/experimental uncertainty on either side of the mean [30].

These results were calculated with a pion mass of 240 MeV/c^2 and a lattice spacing of 0.12 fm. The results of the LQCD calculations are showed in green, while the experimental values taken from Particle Data Group (PDG) [31] are indicated in black. The vertical size of the boxes represents the one-sigma statistical (or experimental) uncertainty with respect to the mean value. The red boxes correspond to hybrid mesons which are grouped to super-multiplets. These mesons do not follow the $n^{2S+1}L_J$ pattern predicted by the quark-model potential [32, 33], where J is the total spin of the meson, L the relative orbital angular momentum, n the radial quantum number and S the quark-antiquark spin. It can be seen that below the open-charm threshold, the results are in very good agreement with the experimental values. The effect of the pion mass and the finite lattice spacing will give larger uncertainties the higher the masses are. As a conclusion, one can say that LQCD provides the tools for the calculation of the masses and widths of particles but at the moment cannot provide calculations for the cross sections of the $p\bar{p}$ reaction to open-charm states. In addition to this, the width resolution that will be achieved in $\bar{\text{P}}$ANDA, will be a powerful tool to test these models and get insight to the dynamics of these systems.

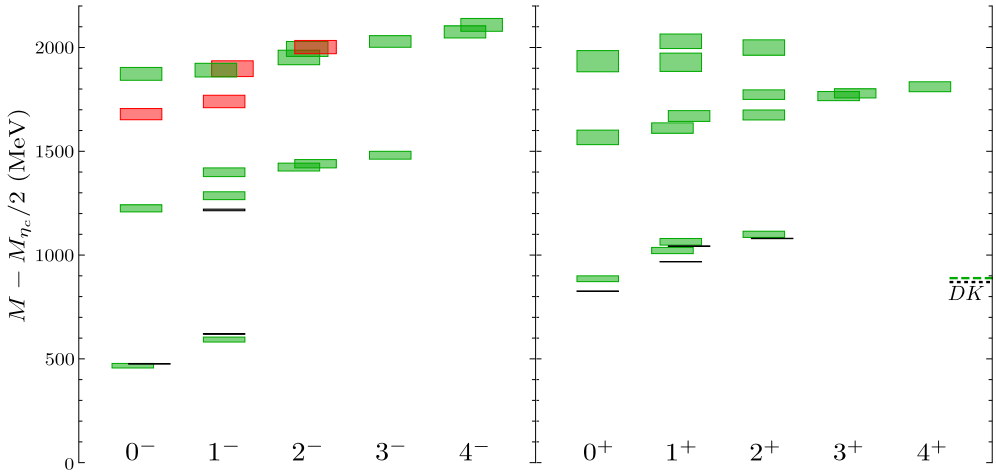

Figure 2.12: Same as figure 2.11 but for the D_s meson [30].

Chapter 3

The $\bar{\text{P}}$ANDA experimental facility

The $\bar{\text{P}}$ANDA experimental facility is presented in this chapter. Today, QCD, the theory of the strong interactions, is well understood and describes phenomena at high energies, where perturbative methods can be used. However, at low energies, in the non-perturbative regime of QCD, there are still many questions to be answered. Many of these questions, can be investigated at low energies via extensive theoretical and experimental studies. The latter requires facilities which operate with low energy and able to produce the states of interest and at the same time detect them. $\bar{\text{P}}$ANDA is such an experiment, which will contribute to the understanding of the phenomena in the non-perturbative regime of QCD. The physics program of $\bar{\text{P}}$ANDA is described below. The individual parts and sub-detectors of the experiment are in section 3.2, while the data acquisition system and software are the topic of the section 3.3. In the last part, the accelerator complex, FAIR, is described.

3.1 Hadron physics using antiprotons

The $\bar{\text{P}}$ANDA experimental facility will cover a diverse and broad hadron-physics program. The design of the detector together with the unique high-quality antiproton beam will give the opportunity for extensive studies of the physics of interest. The aim is to broaden our knowledge of the strong interaction and the structure of hadrons. It will also contribute to the existing knowledge of the field by supplying high statistics and improvements to the precision of the measurements (masses and widths), which, in many cases, are the key elements

to get insight into the physics phenomena and confirm theoretical models. The high luminosity for proton-antiproton annihilation will will give in some cases a statistical precision that no other experiment can achieve, such as in the hyperon sector.

The antiproton-proton annihilation enables unique opportunities as all kinds of quantum numbers can be produced. In this interaction, quarks and antiquarks can annihilate into a large number of states with a variety of spin-parity combinations that can couple to different flavored quark-antiquark pairs, thereby, forming a hadron of interest directly. This should be contrasted with e^+e^- colliders, where to first order only states with $J^{PC} = 1^{--}$ can be produced, due to the exchange of an intermediate virtual photon which limits the allowed spin-parity combination. In proton-antiproton annihilation all states with conventional spin-parity quantum numbers can be directly populated. This is in particularly advantageous when a state is very narrow in width or when the interest is to study a very high-spin state. With $\bar{\text{P}}$ANDA, the determination of the line shape of resonances can be performed with high accuracy, since the energy resolution for the resonance scan is excellent (40 - 50 keV). In e^+e^- colliders, resonance scans can only be conducted for $J^{PC} = 1^{--}$ states, and these can only be performed with resolutions on the scale of 1 MeV.

As seen in figure 3.1, the center-of-mass energy of $\bar{\text{P}}$ANDA will be between 2.26 GeV to 5.48 GeV for the antiproton beam momentum in the range of 1.5 GeV/c to 15 GeV/c. This energy range is larger than other experiments, such as the BEijing Spectrometer III (BESIII) [34]. States with heavier masses, such as high-spin charmonium-like resonances, are not accessible by BESIII, but will be in reach with $\bar{\text{P}}$ANDA.

$\bar{\text{P}}$ANDA's initial state is unique, acting complementary to other experiments, and therefore, might be more sensitive to objects not seen by them. For example, the formation of gluon-rich hadrons is expected to be favorable in proton-antiproton collisions due to the annihilation of quarks with antiquarks with the production of gluons.

In the following, we briefly discuss some of the highlight topics that $\bar{\text{P}}$ANDA aims to address. For a more extended overview of $\bar{\text{P}}$ANDA's physics program, see [35].

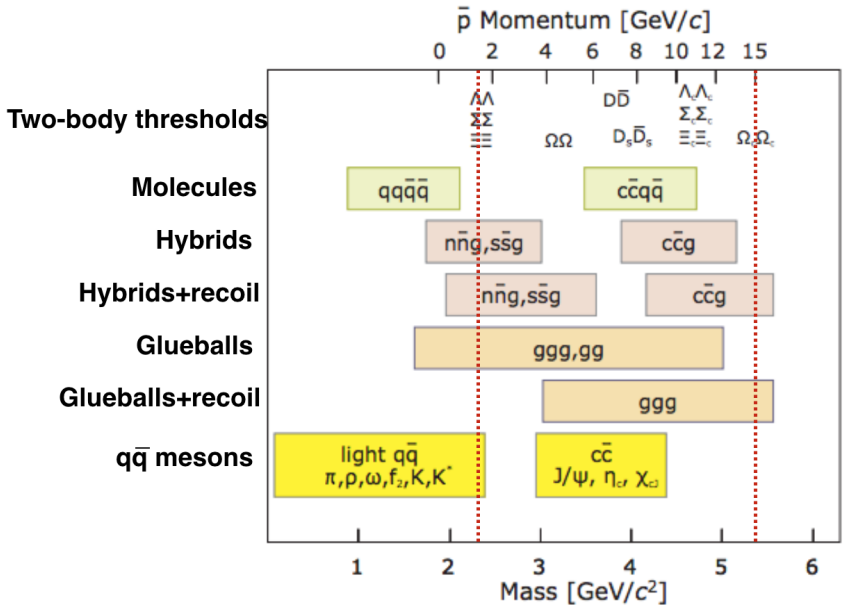

Figure 3.1: Mass range of hadrons accessible with $\bar{\text{P}}$ANDA [36]. The red dotted lines correspond to the antiproton momentum range of $\bar{\text{P}}$ANDA.

3.1.1 Hadron spectroscopy

In the following, we briefly discuss a few of the studies that are foreseen with $\bar{\text{P}}$ANDA in the field of hadron structure. These include studies in the fields of open-charm, charmonium(like), and heavy baryon spectroscopy.

The investigation and measurement of the D and D_s mesons, as well as very narrow $D^*_{sJ}(2317)$ and $D_{sJ}(2458)$ mesons are a few of the goals for $\bar{\text{P}}$ANDA. Existing experiments have observed these states [37], but these studies triggered intense discussions since they appear at unexpected locations (large mass shift compared to the theoretical predictions [38]) which raise questions on whether these states are pure mesonic particles or if they posses an exotic component. The system of a heavy quark, c, and a light quark, u or d, is similar to a hydrogen atom, which consists of a proton and an electron. The heavy quark can be considered as stationary and the strong force effects can be described by the presence of the light quark. The threshold production of D mesons in $\bar{\text{P}}$ANDA, which will allow little phase space for additional hadrons, together with the mass resolutions expected (of the order of 100 keV) due to the high antiproton beam momentum resolution ($\Delta p/p \sim 4 \times 10^{-5}$) will provide us with the tools for unprecedented production and investigation of open-charm mesons.

Regarding the charmonium states, the discovery of the J/ψ meson [39, 40] opened the way for the understanding of the strong interaction in terms of QCD. Even though the discovery of the J/ψ meson happened over 40 years ago, charmonium physics has still many interesting aspects to be investigated and questions to be answered [41]. For example, the mass and width of the ground state of charmonium η_c have been measured from many experiments but still the differences are large [42,43]. Moreover, with a close look at the charmonium spectrum (figure 3.2), one can see that all eight states below the $D\bar{D}$ threshold are established. On the other hand, the dozens of states above the threshold (the so-called XYZ states) are either discovered but far from the predictions or predicted but not yet discovered. $\bar{\text{P}}$ANDA will add a major contribution with its high-precision resonance scans, luminosity, and detector capabilities. At full luminosity, $\bar{\text{P}}$ANDA will be able to produce thousands of charmonium states (like the J/ψ) within few minutes of operation, and measure masses with an accuracy of 100 keV and widths (in some cases) of 10% or better.

In $\bar{\text{P}}$ANDA, baryon states with strangeness, like Λ, Ξ, Ω, will also be measured. These states, with strangeness as an additional degree of freedom, are hard to be interpreted, and the questions about their excitation spectra and whether they follow the standard SU(3) flavor symmetry are still open [44, 45]. With the high antiproton momentum of $\bar{\text{P}}$ANDA, he production cross sections are estimated to be large (the ratio of the production of baryonic final states in comparison to mesonic states is more than a factor of 2), and thus copious production of the interesting baryon-antibaryon pairs. In addition, large rates of excited baryons are produced. The analysis of the angular distributions of the produced particles from their decay, allows the spin-parity quantum numbers to be determined. Last but not least, the presence of antiprotons, gives an advantage, since no extra kaons or D mesons are required for the strangeness or charm conservation, which reduces the production threshold for these states.

3.1.2 Gluonic excitations

The gluons, the force-carrying bosons of the strong interaction, act as main components for the formation of the hadrons. The gluons also interact among themselves since they carry a color charge. The formation of gluon-rich matter is, therefore, allowed by the SM. This new type of hadrons can be divided in two main categories: the glueballs and the hybrids. Glueballs are basically states consisting only of gluons while hybrids consist of a quark, an antiquark and gluon. Since the gluons add extra degrees of freedom to a hadron, both glueballs and hybrids can have quantum numbers that are forbidden for a fermion-antifermion pair, such as $J^{PC} = 0^{--}$, 0^{+-}, 1^{-+}, and 2^{+-}. Up to now, the

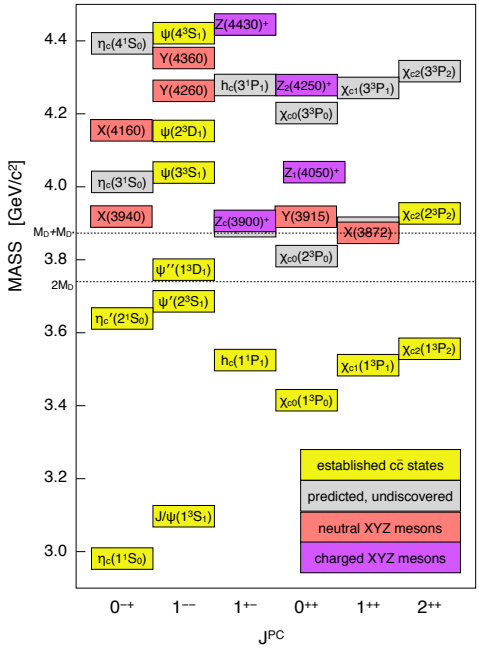

Figure 3.2: The mass spectrum of charmonium(-like) states [46].

efforts have been focused to masses below 2.2 GeV/c^2. P̄ANDA can improve the measurements both in this region but also in higher mass regions due to the expected high cross section (when the width is not very large). Hybrid candidates with exotic quantum numbers 1^{-+} have been observed, first in πN scattering experiments [47, 48] and antiproton annihilations [49, 50]. Their masses are 1400 MeV/c^2 and 1600 MeV/c^2, respectively. The Crystal Barrel experiment discovered a narrow glueball candidate with a mass of 1500 MeV/c^2 in antiproton annihilation, which is considered to be the best candidate of the ground state of $J^{PC} = 0^{++}$ [51–55]. The predictions of the glueball spectrum of one of the lattice QCD calculations are shown in figure 3.3. P̄ANDA covers a large part of the predicted glueball spectrum including states with exotic quantum numbers, such as the 0^{+-} state, which is needed to unambiguously determine the quantum numbers of exotic states, and has not yet been studied. P̄ANDA has a large acceptance, which is needed for the quantum number determination, as it can run in two modes: the production mode, where exotics can appear, and the formation mode for higher mass/widths resolution, where only non-exotic states can be produced. This combination of modes can be used to pinpoint exotic states.

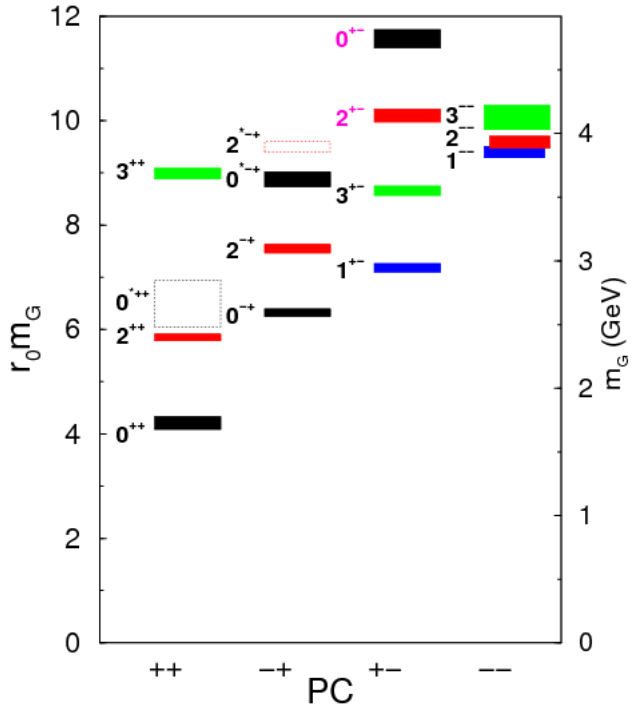

Figure 3.3: Glueball spectrum predicted from LQCD [56, 57]. Left vertical axis represents masses in hadron scale (410 MeV/c^2) and the right axis in GeV. The different color boxes represent different orbital angular momenta L and the vertical size of the boxes indicates the mass uncertainty based on the standard deviation.

3.1.3 Hypernuclei

Hyperons are baryons in which one of the up or down quarks in a nucleon is replaced by a strange quark. They only decay via weak interactions and together with a nucleus, they can form a so-called hypernucleus. In this way, a new quantum number is introduced in the nuclear chart, the strangeness. Up to now, due to experimental limitations, the extra dimension coming from strangeness has been poorly studied. Due to the strangeness, the hyperons, unlike to a proton or neutron, are not restricted by the Pauli principle in the states they can form. Because of this, hyperons can populate the states near the ground state and allow spectroscopy between states where we normally cannot observe transitions. Despite the fact that Λ hypenuclei have been discovered more than 50 years ago [58, 59], today only 6 are known. The presence of a hyperon, usually a Λ particle, inside the nuclear medium, may give a better insight into the structure of the nucleons. $\bar{\text{P}}$ANDA will be able to produce a large number of

hyperons due to the high production cross section of hyperon-antihyperon pairs in antiproton-nuclei. More specifically, bound states of Ξ hyperons will be used to form double-Λ hypernuclei [60]. The two units of strangeness are introduced with the Ξ cascade inside the nucleus that will convert very quickly into the two Λs. The steps of the production of the hypernuclei in $\bar{\text{P}}$ANDA are shown in figure 3.4.

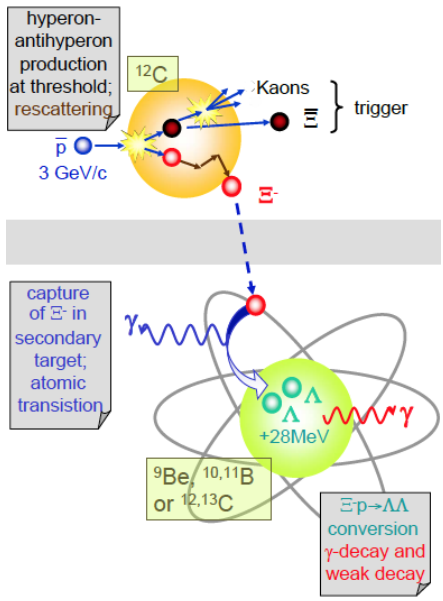

Figure 3.4: The production chain of double hypernuclei in $\bar{\text{P}}$ANDA [35]. The Ξ from the initial reaction will be stopped and captured in a secondary target (such as ^{12}C). It will then decay into a pair of Λs that are bound in the secondary nucleus.

3.1.4 The structure of the nucleon

It is foreseen for $\bar{\text{P}}$ANDA to study processes in the transition region towards perturbative QCD [35]. In the past years, the development of the theoretical framework of the General Parton Distributions (GPD) is remarkable. As a result, it is possible to use the GPD to describe hard processes in lepton scattering experiments and thereby get insight into the internal structure of the nucleon. In the so-called "QCD handbag" approach, the wide-angle Compton scattering ($p\bar{p} \to \gamma\gamma$) can be divided into two parts, the "soft" and the "hard". The amplitudes that parametrize the "soft" part are called Generalised Distribution Amplitudes (GDA). In the "hard" part, where the momentum of the involved photon is quite large, perturbative QCD methods can be used for the calculation of the amplitudes due to the large Q^2 transfer of the exchange photon. The

measurement of the process $p\bar{p} \to \gamma\gamma$ as a function of the s and t variables (s and t are two of the so-called Mandelstam variables which are numerical quantities containing the energy, momentum, and angles information of particles in a scattering process) is quite a challenge due to the very small cross section. $\bar{\text{P}}$ANDA, running in the High-Luminosity (HL) mode, will be able to study this process and probe the nucleon structure. The detector configuration will also play an important role, especially the 4π acceptance of the electromagnetic calorimeters. Another process which can be described by the "QCD handbag" approach and will be studied in $\bar{\text{P}}$ANDA is when one photon is replaced by a pion ($p\bar{p} \to \pi^0\gamma$).

$\bar{\text{P}}$ANDA will also study Drell-Yan processes ($p\bar{p} \to \mu^+\mu^- X$) as well as electron-positron pair and muon-pair processes ($p\bar{p} \to e^+e^-$ and $p\bar{p} \to \mu^+\mu^-$) [35]. In the first case, the study of the momenta of the partons participating in the reaction will provide the insight into the structure of the nucleon, while in the second case, access to the time-like region of the electromagnetic form factor of the proton will be achieved. This will lead to an extraction of the electric (G_E) and the magnetic (G_M) form factors.

3.1.5 Hadrons in nuclear matter

The understanding of the origin of the hadron masses is one of the main goals of $\bar{\text{P}}$ANDA. The interactions that take place in the nuclear medium, affect the properties of mesons or other hadrons. The reason for this, is the spontaneous chiral-symmetry breaking and its partial restoration. Chiral-symmetry breaking leads to a mass shift between the parity partners of hadrons. The largest mass shifts are seen when hadrons are produced with low momenta inside a nucleus. Up to now, many experiments have investigated the light-quark sector [61–64]. $\bar{\text{P}}$ANDA will extend this investigation to the heavier charm sector for hadrons with both open and hidden charm. This will be feasible due to the very high-intensity antiproton beam and the low energies at $\bar{\text{P}}$ANDA. The opportunity of producing high statistics of D mesons at sub-threshold energies, will give a much better insight in the origin of the mass splitting. While for some states, like the J/ψ and η_c, a mass shift of 5-10 MeV/c^2 is observed [65], for D mesons the shift is expected to be 50-100 MeV/c^2 [66, 67].

3.2 P̄ANDA detector system

In order to achieve P̄ANDA's physics objectives, a sophisticated detector system is needed. This system should have almost 4π acceptance, high resolution for tracking, calorimetry and PID, together with high rate capabilities of the detectors and their electronic readout systems. The P̄ANDA detector system, satisfying all these criteria, is about 13 meters long and has a diameter of about 5 meters. The sub-detector systems are divided into two parts: the target spectrometer and the forward spectrometer. A 2 Tesla superconducting solenoid magnet will be around the target area while a large dipole magnet is placed in the forward region. The combination of the magnetic field and the tracking detectors allows to reconstruct the momenta of charged particles. In the coming sections, each individual sub-detector part will be presented together with a detailed overview of the target system since this will be the main focus of this thesis.

3.2.1 Target spectrometer

The target spectrometer (figure 3.5, left part of the dipole magnet) surrounds the interaction point and it has an onion-like structure. The pipe through which the beam particles travel is perpendicular to the pipe that will inject the target material. The barrel part of the target spectrometer covers polar angles $\theta \geq 22^{\circ}$ and the endcap covers polar angles $\theta \geq 5^{\circ}$ in the vertical plane and $\theta \geq 10^{\circ}$ in the horizontal plane.

Targets

Due to the space limitations in the target spectrometer volume, the selection of a suitable target system is challenging. In order to reach the highest luminosity, a target density of about 4×10^{15} hydrogen atoms per cm^2 is required. At the moment, two target systems are under development, the cluster-jet target (which will be used in the initial measurement phase of P̄ANDA) and the pellet target (figure 3.6). For the cluster-jet target, the material used is either hydrogen (H_2) or deuterium (D_2). The clusters (each containing typically 10^5 atoms) are formed when a pre-cooled gas ($\sim$ 30 K) is forced through a nozzle with a very small diameter (10 - 100 μm). A combination of valves for the vacuum and collimators to reduce the spread of the clusters are used to obtain the final density and quality of the clusters needed for P̄ANDA's physics program [69]. The pellet target provides a stream of individual frozen drops with a typical diameter of 20 μm instead of a spray of a large number of small clusters of

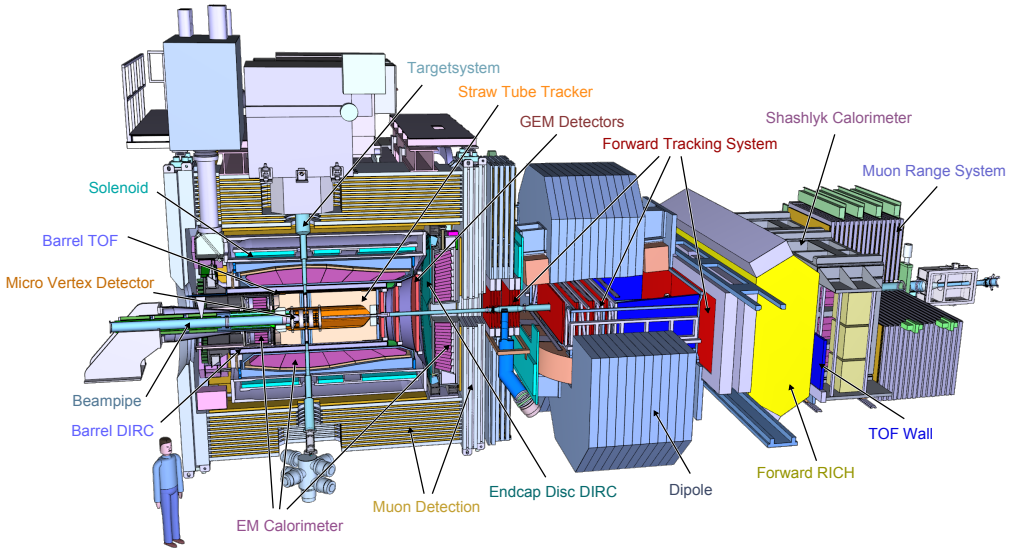

Figure 3.5: CAD view of the P̄ANDA detector system. The antiproton beam enters from the left side [68].

molecules. This kind of target will be the only choice for the high-luminosity mode of High Energy Storage Ring (HESR). The frozen drops are produced as follows: the gas (H_2) is cooled and liquefied in three steps. The first is cooling with liquid N_2. Further cooling by evaporated helium is then performed, and finally, cold helium gas is used in the last cooling stage. The gas is then injected into a triple point chamber through a narrow (10 μm) orifice. The nozzle is vibrated by a piezoelectric device which introduces Rayleigh-Taylor instabilities to the liquid stream, thereby allowing this to break up into uniform size droplets. After the nozzle, there is a chamber filled with the same gas that is held at a temperature and pressure close to its triple-point. The drops then cool down in the triple point chamber by evaporation to below the freezing point. After about 5 cm there is a sluice in which the frozen droplets are accelerated as they proceed into the vacuum. A shaper forms the flux of the pellets before reaching the interaction point [69].

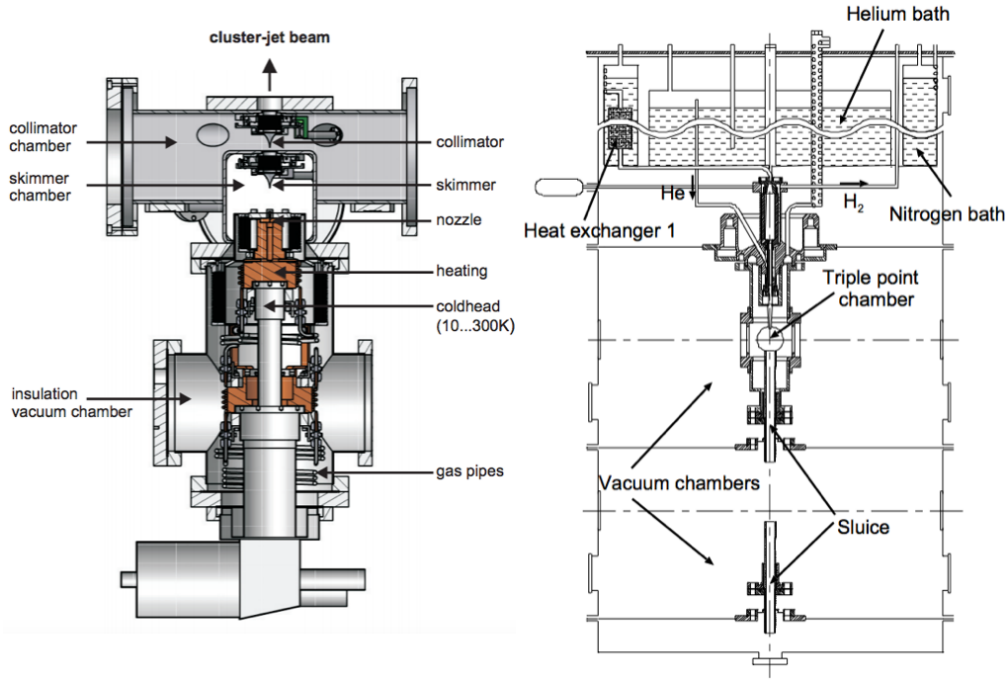

Figure 3.6: The target candidates for P̄ANDA. On the left the cluster-jet target system is shown and on the right the pellet target system [69].

Straw Tube Tracker (STT)

The STT is the main tracking detector of the P̄ANDA target spectrometer. It has two main tasks. The first is to perform a spatial reconstruction with a precision in the order of 150 μm of hits from tracks of charged particles with momenta ranging from a few hundred MeV/c to 8 GeV/c. The reconstruction of the particle trajectories will result in the measurement of the momentum inside the magnetic field. The second task is PID through the specific energy-loss measurements ($\mathrm{d}E/\mathrm{d}x$) in the active volume of the tubes. More specifically, the separation of protons, kaons and pions for momenta below 0.8 GeV/c is of crucial importance.

The forward spectrometer will be responsible for the PID of particles in the very forward angles and the Detection of Internally-Reflected-Cherenkov light (DIRC) (described later in this chapter) for those with larger emission angles. But the DIRC can only perform PID for particles which have momenta higher than the Cherenkov threshold, which is 0.6 GeV/c. Thus, for low momenta, the central tracking system is the only sub-detector able to perform PID. The

detector will use gas-filled drift tubes as the basic detector element. The STT has a cylindrical shape with an inner radius of 150 mm, an outer radius of 420 mm, an overall length of 1650 mm and an angular coverage from 10° to 140° (figure 3.7).

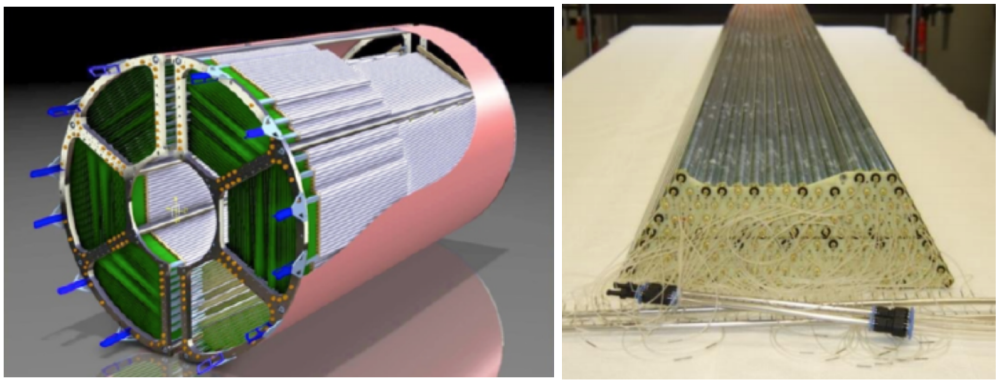

Figure 3.7: On the left, a CAD drawing of the STT is shown [68]. On the right, one of the hexagonal sectors of the STT is shown.

The detector will consist of 4224 straw tubes arranged into 27 layers in radial direction. The layers are positioned in such a way that 19 of them are in parallel with the beam direction and 8 of them are skewed by about ±3° relative to the beam direction. This will allow for a 3D reconstruction of the trajectories of the particles. The total weight of the STT straw tubes adds up to less than 16 kg. In order to keep the material budget and the total weight low, a self supporting structure is used for the tubes [70]. The tubes have an active length of 1400 mm, an inner diameter of 10 mm and are made of double layers of aluminumized Mylar films with a total thickness of 27 μm as cathode. A gold-plated tungsten-rhenium wire with a diameter of 20 μm (figure 3.8) is used as anode inside the tubes. The wire inside the tubes is kept straight by a tension of 50 g that is generated by operating the tubes at 1 bar overpressure (2 bar absolute pressure). A gas mixture of 90% argon (Ar) and 10% carbon dioxide (CO_2) is used. A positive electric field of about 2 kV is applied to the wire to separate the ions and the electrons created when a charged particle passes the gas volume. The electrons drift to the anode wire while the ions move to the wall. An amplification of $5{\times}10^4$ is expected on the signal, which makes it large enough to be processed by the readout system [68].

The readout of the straw signals is performed in three steps. First, an analog Front-End-Electronics (FEE) part is placed close to the detector. This will host the high voltage, preamplifier, amplifier with analog signal shaping and discriminator. The signal after the first step is ready to be translated from an analog to

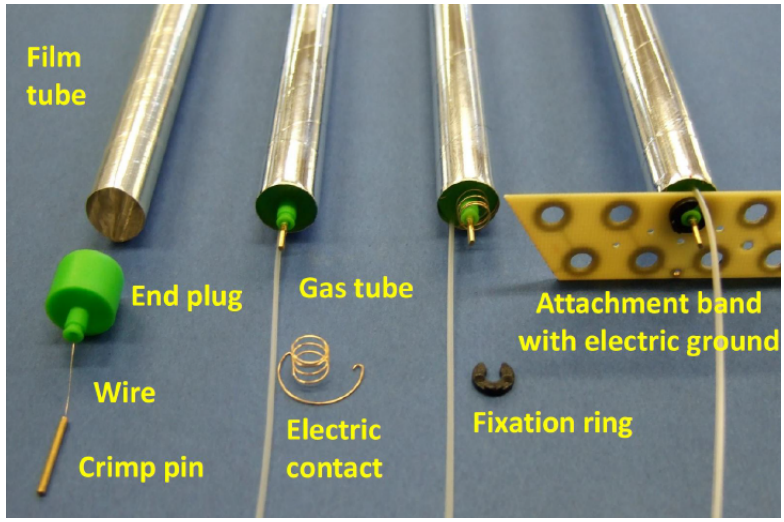

Figure 3.8: The various components of a single straw tube of the STT. The diameter of the tubes is 10 mm [68].

digital format. This is done in the second step which includes the Digital Board (DB), which takes care of the time, amplitude and charge measurements, the hit detection and storage, as well as the data transmission and slow control. At the moment there are two concepts to perform this step: one is based on a Time-to-Digital Convertion (TDC) which uses the time information of the signals within a clock cycle based on a reference time. An Application-Specific-Integrated Circuit (ASIC) is developed to read out the straw signals. The performance of such a readout system is the subject of chapter 4 in this thesis. The second method is based on an Analog-to-Digital Convertion (ADC) technology (here no FEE are present), which is designed to convert the analog information (current or voltage) into binary information. The third step of the readout is the Concentrator Board (CB), which receives and merges all the input from the DBs and sends it to PANDA's Data Acquisition (DAQ) system.

Micro Vertex Detector (MVD)

The location of the Micro Vertex Detector (MVD) is close to the interaction point for the detection of tracks and secondary vertices coming from D meson and hyperon decays. The detector's precise timing information (resolution of about 7 ns) together with the optimized design will result in a transverse position resolution of about 100 μm and a full three dimensional track reconstruction. The detector has two parts. The MVD barrel part consists of 4 layers of which the two inner ones have pixel detectors and the two outer ones double-sided silicon strips.

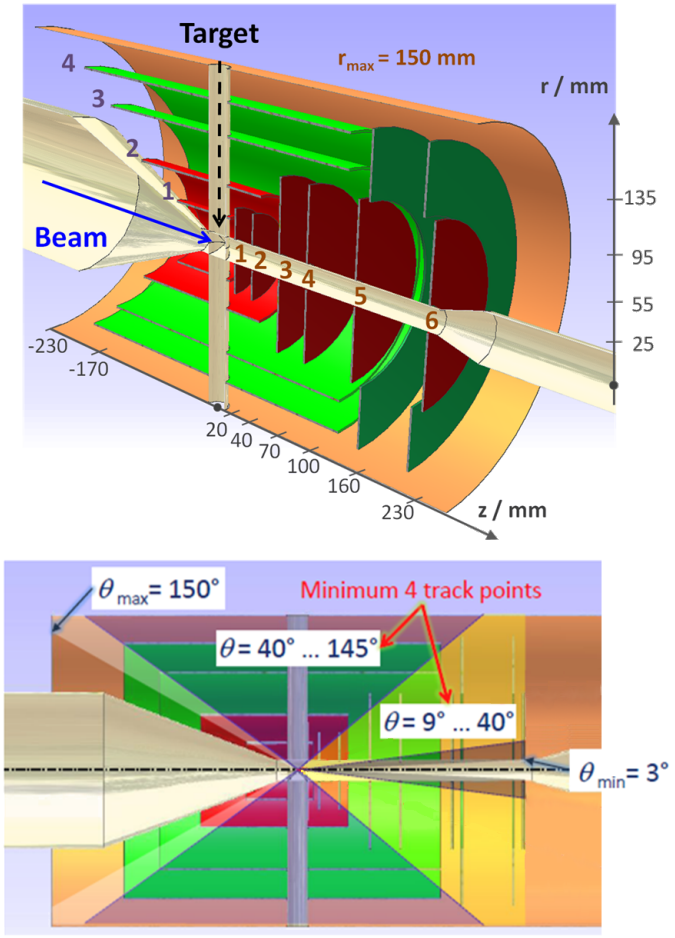

Figure 3.9: Schematic view of the MVD detector [71]. In the upper picture the positions of the pixel sensors (red) and the strip sensors (green) are shown. In the lower picture, the angular coverage of the MVD is indicated.

The forward part of the MVD consists of eight wheels placed perpendicular to the beam direction. In this part, the two layers closest to the interaction region are again made from pixel sensors while the next four are a combination of pixel detectors (close to the beam pipe) and silicon strips (far from the beam pipe). Finally, the last two wheels are entirely made from silicon strips (figure 3.9). The polar angle coverage for the disk part is from 3° to 40° and from 40° to 150° for the barrel part (figure 3.9). The sensor material of the MVD is made from silicon, a low price material, which is radiation hard and has fast response time. The silicon strips have different shapes depending on the place they are located. In the barrel part, rectangular and square shapes are used while in the forward part, trapezoidal shapes are chosen. For the readout of the MVD an ASIC chip is used which offers two important features, namely, a fast timing information and the capability of handling high hit rates.

Gas Electron Multiplier (GEM)

The Gas Electron Multiplier (GEM) detector consists of 3 disks which are located at a distance of 1.1 m, 1.4 m, and 1.9 m downstream from the target [35]. They cover polar angles between 3° and 22°, thereby covering angles complementary to the STT. Gaseous micro pattern detectors based on GEM foils are responsible for the hit detection. A foil is usually a plastic material mounted on a conducting part. The disks are made of double planes with two orthogonal projections per plane. The combination of the two individual projections, can give 2D information on the tracks. The readout uses ASIC chips which are placed in the outer part of the detector.

Barrel and Disc Detection of Internally Reflected Cherenkov Light (DIRC) detectors

Detectors that register Cherenkov light, emitted when particles pass through a medium with a velocity larger than the speed of light in that medium, are installed to contribute to the PID. In DIRC detectors, the active material where the Cherenkov light produced is at the same time the light guide needed to transfer that light to the photosensors. The opening angle of the light cone which contains the information about the velocity of the incident particle, together with the momentum information from the tracking detectors, will be used to calculate the corresponding mass of the particle. $\bar{\text{P}}$ANDA has two DIRC detectors, the barrel DIRC and the disc DIRC. The first will cover polar angles from 22° to 140° and the latter from 5° to 22°. The material used for the detectors is a synthetic fused silica which fulfills the requirements for clean and fast light

transmission and radiation hardness. Figure 3.10 shows schematic images of the two DIRC detectors of P̄ANDA.

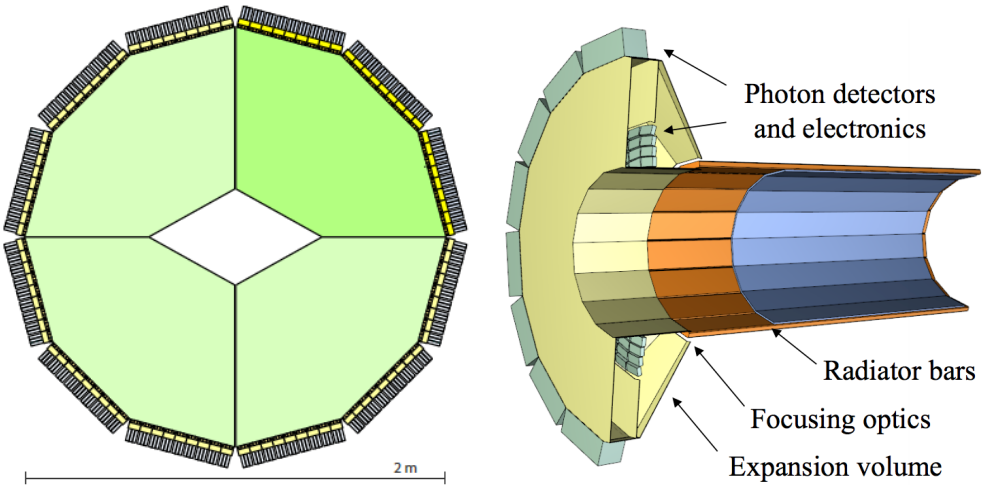

(a) (b)

Figure 3.10: The DIRC detectors of P̄ANDA: (a) A drawing of the Disc DIRC [72]. (b) The Barrel DIRC with its elements [73].

Barrel ElectroMagnetic Calorimeter (BEMC) and EMC endcaps

The Barrel ElectroMagnetic Calorimeter (BEMC), shown in figure 3.11, is responsible for the detection of many particles as well as for the PID. It will measure the total energy deposited by photons and electrons/positrons. It will cover polar angles from 22° to 140°. It has a length of 2.5 m, surrounding the barrel DIRC and Time-Of-Flight (TOF), starting at a radial distance from the beam pipe of 0.57 m and ending at 0.94 m. In total, 11360 crystals will be mounted on the BEMC, for which an energy resolution of $2\%\sqrt{E(GeV)}$ and a time resolution of 150 ps (>1 ns) at energies above 500 MeV (above 60 MeV). The crystals are made of lead tungstate ($PbWO_4$), which is an inorganic scintillator. Each crystal is 20 cm long and it has a mass weight of 0.98 kg [74]. A light yield of 17-20 photoelectrons/MeV at 18°C will allow particles with a few MeV (threshold is at 4 MeV) to be measured. This light yield is enhanced by the fact that the crystals are cooled to −20°, which will result in an increase in light yield by a factor of 2. The readout of each crystal will be performed by two large area (14 mm × 7 mm) avalanche photo diodes.

The BEMC is complemented by two endcaps placed at forward and backward angles. The forward endcap, closes the barrel part in the forward/beam direc-

tion. It is located 2.1 m far from the interaction point and it has a diameter of 2 m. The forward endcap will cover polar angles from 10° to 23.6° horizontally and 5° to 23.6° vertically. The backward endcap will be installed in a distance of -1 m with respect to the interaction point. It will have a diameter of 0.8 m and it will cover polar angles from 151.4° to 169.7°.

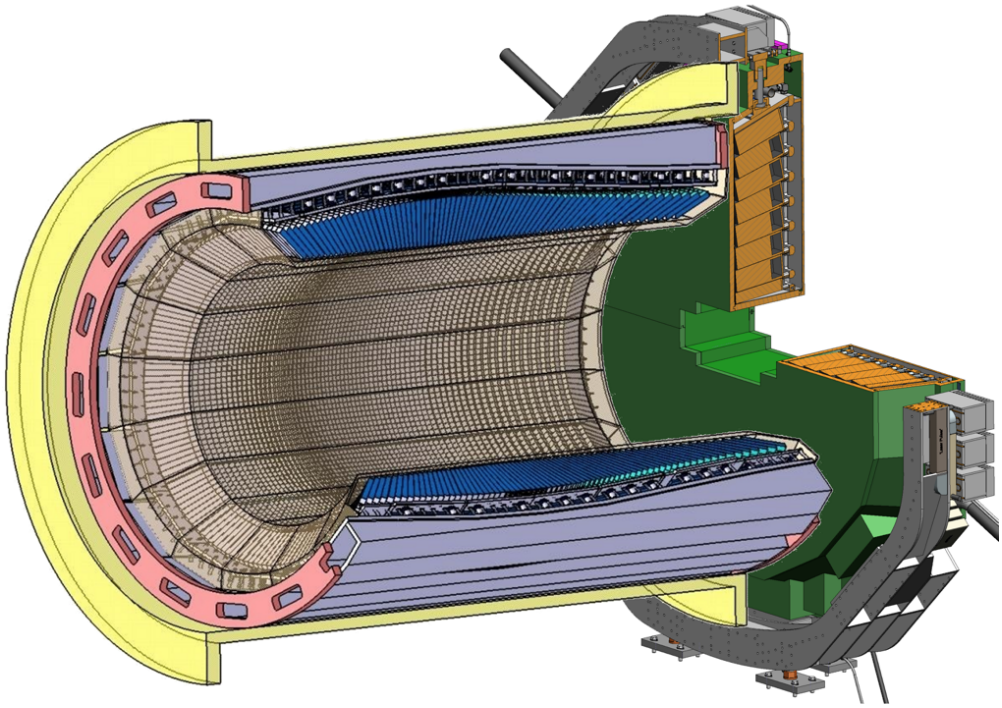

Figure 3.11: 3D view of the EMC of $\bar{\text{P}}$ANDA [75]. The cylindrical part is the BEMC while the segment in green and orange is the forward endcap.

Barrel Time Of Flight (BTOF)

For particles with low velocity and large emission angles, PID will be provided by the information coming form the Barrel Time-Of-Flight (BTOF). It will surround the barrel DIRC and it can also detect photon conversions in the DIRC. The detector will consist of 5760 scintillator tiles of 28.5 mm × 28.5 mm size and 5 mm thickness. This detector will cover polar angles from 22° to 140°. The readout for each of the tiles is performed by two silicon photo-multipliers. The time precision reached will be about 100 ps.

Muon system

The detection of muons is made possible by the so-called muon system of P̄ANDA. Muons play an important role in various physics channels, such as J/ψ and D meson decays, where it is very important to identify muons coming from these decays. However, the muon system of P̄ANDA can only poorly separate prompt muons from secondary muons. The system will use aluminium drift tubes as detector material, which are called Mini-Drift Tubes (MDT). These tubes employ a gold-plated tungsten wire at the center. The simple but robust design provides the required time and space resolution for muons with momenta between 1 to 10 GeV/c to be detected and identified. The muon system in the target spectrometer consists of three parts. The barrel, the endcap and the filter. The barrel has 13 layers of drift tubes in a 3 cm gap between equally thick layers of iron absorber. The endcap has 6 layers of alternating detector and absorber material each 6 cm thick. After the endcap, an extra setup of 4 alternating layers is present, which is identical to the endcap and it is called the filter muon system. In total, 3751 MDTs are present in the muon system of the target spectrometer, covering polar angles from 0° to 140°.

3.2.2 Forward spectrometer

Forward Tracking System (FTS)

The Forward Tracking System (FTS) is responsible for the track reconstruction in the forward direction. The main goal is to measure the deflection of the particle trajectories due to the presence of the dipole magnet. The detector will use straw tubes of the same size, gas mixture and wire as used for the STT but the endplugs will be different to simplify the mass production of the straws to roughly a factor 5 times more straws than for the STT. In total, there will be three FTS stations present, before, within and after the dipole magnet (see figure 3.12). Each station will have two tracking detectors, each one consisting of four double layers [35]. Two of the double layers will be arranged vertically, and two will have a small inclination to provide a two-dimensional position measurement. A position resolution of the order of 150 μm is expected.

Ring Imaging Cherenkov (RICH) detector

Due to the strong Lorentz boost, many particles will have high momentum, and thus TOF will not be very effective for PID for a significant fraction of particles. The Ring Imaging Cherenkov (RICH) detector is one of the two PID detectors

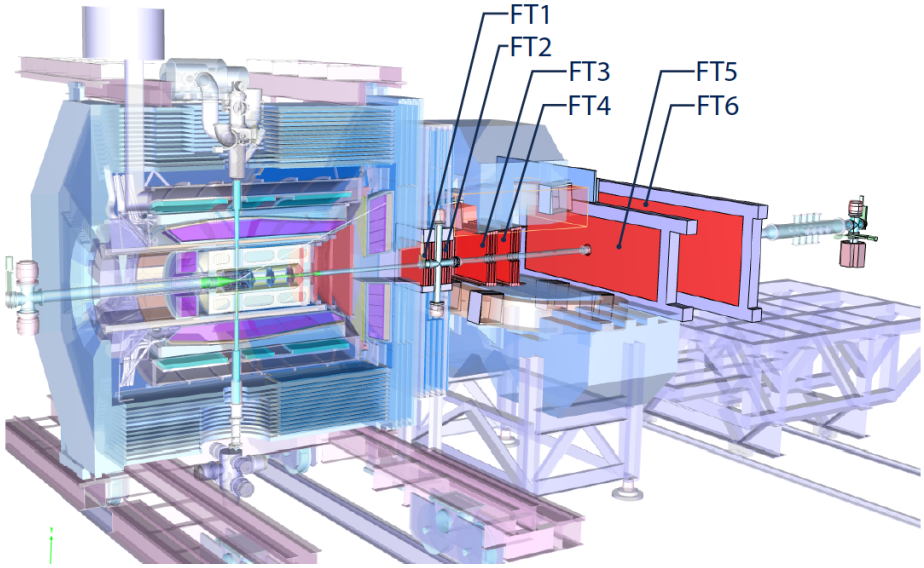

Figure 3.12: Positions of the six FTS stations in the $\bar{\text{P}}$ANDA forward spectrometer [76].

for particles emitted in the forward angles, responsible for the separation of K, π, p in a broad momentum range (2 - 15 GeV/c). It will consist of two radiators, silica aerogel of varying index of refraction and C_4F_{10} gas for the creation of the Cherenkov light [35]. A mirror is installed to focus and guide the light to an array of phototubes for the readout. The RICH is able to detect particles with polar angles $\theta < 10^{\circ}$.

Forward Time Of Flight (FTOF)

After the RICH detector, at a distance of 7 meters away from the interaction point, the Forward Time-Of-Flight (FTOF) is located. The role of the detector is to contribute to the PID of particles emitted in very forward angles. The time resolution of 50 ps will allow for precise time measurements. The detector will consist of vertical scintillator strips of different widths [35]. A separation of 3σ is expected between K/π, p/π and K/p at 4.7 GeV/c.

Forward Electromagnetic Calorimeter (FEMC)

The Forward ElectroMagnetic Calorimeter (FEMC) will perform the same tasks as the BEMC but at very forward polar angles. The calorimeter type is of Shashlyk-type, and it is based on wavelength shifting fibers within the scintillator blocks, which will be 55 mm thick. The readout is performed by photomultipliers coupled to the blocks [35]. A total of 1512 detection blocks create an active area of 2.97 m $\times$ 1.54 m. The expected energy resolution expected is of the order of $4\%\sqrt{E}$.

Forward Muon System (FMS)

For the detection of forward emitted muons, a Forward Muon System (FMS) is installed after the FEMC at a distance of 9 meters downstream from the interaction point. The setup is similar to the muon system of the target spectrometer, but has been reconfigured for higher momenta. The detector operates as a hadronic calorimeter, measuring the energies of neutrons and antineutrons and at the same time discriminating pions from muons, and detecting pion decays [77]. In total 16 double layers are installed with alternating MDT's and absorber layers, each one 6 cm thick.

Luminosity Detector (LMD)

The Luminosity Detector (LMD) is the most downstream detector in P̄ANDA (figure 3.13), which is located around 10.5 meters away from the interaction point. Its purpose is the measurement of the relative luminosity from the elastically-scattered antiprotons in the Coulomb-nuclear interaction region. This will allow the absolute luminosity to be measured with an absolute precision of 5%. The antiprotons are measured in very small polar angles between 3 mrad and 8 mrad. High-Voltage-Monolithic-Active-Pixel Sensors (HV-MAPS) will be employed in four layers which are responsible for the detection of the antiprotons. A cone is present in the front part of the LMD to reduce the influence of the beam pipe. The whole setup will operate in vacuum to minimize the interactions of antiprotons with the air within the detector.

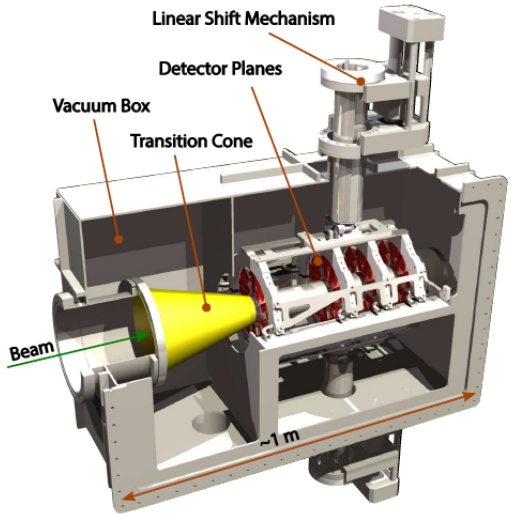

Figure 3.13: A CAD drawing of the LMD detector [78, 79].

In the first years of data taking, a period referred to as "phase-1", not all the detector components will be available. Part of the GEMs, the Disc DIRC, and the forward RICH will not be available. Moreover, the total number of antiprotons in the ring will be limited to 10^{10}, which results in a luminosity that is about one order of magnitude smaller than the design. In the second phase, all detector components are planned to be installed, however, still with a limited luminosity. The full operation including the highest possible luminosity is referred to as "phase-3". The duration of each phase is still under discussion during writing of this thesis.

3.3 Data-acquisition and software

3.3.1 Data-acquisition scheme

As mentioned in the previous chapter, $\bar{\text{P}}$ANDA will have a broad physics program. A large amount of statistics is needed to perform high-precision measurements as well as a smart way to distinguish the desired physics signals from the background. $\bar{\text{P}}$ANDA will operate with a rate of 20 MHz in the high-luminosity mode which will lead to up to 200 GB/s of data that needs to be processed. This data rate needs to be reduced by a factor of up to 1000 to match the data-storage capacity. In contrast to classical experiments, $\bar{\text{P}}$ANDA will not have a regular hardware trigger mechanism. There will be a continuous stream of data and at the same time a continuous search for interesting event topologies.

Due to the similar event topologies of the signal and the background, a reconstruction of the full decay chain will be needed to get sufficient information in order to discriminate signal and background. This requires an intelligent online event selection system. An overview of the data-acquisition scheme of $\bar{\text{P}}$ANDA is shown in figure 3.14.

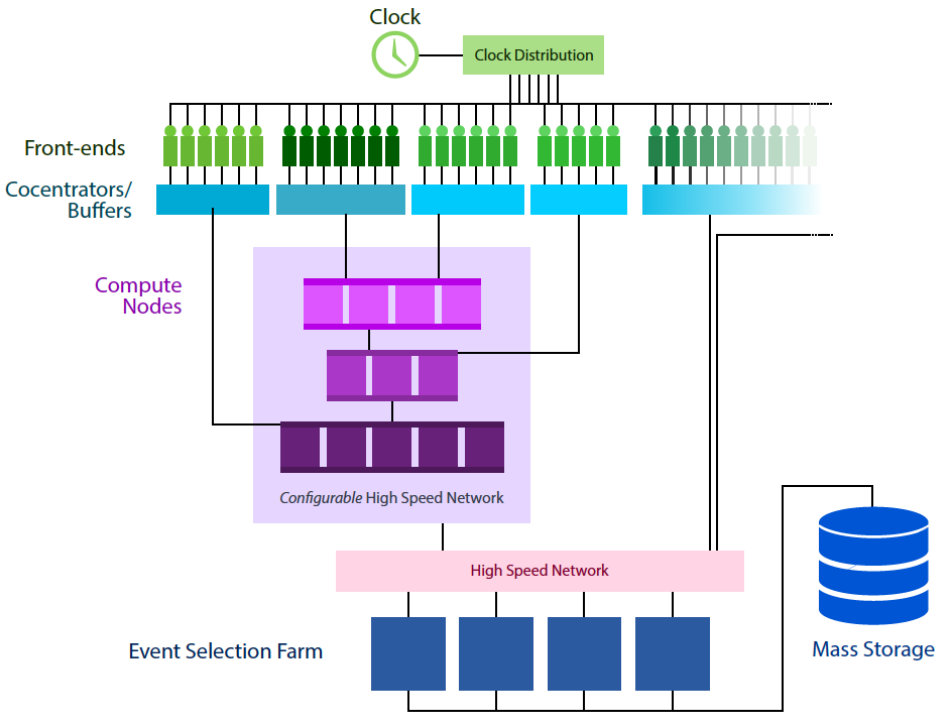

Figure 3.14: Overview of the $\bar{\text{P}}$ANDA data-acquisition scheme [36].

Since the data taking runs continuously, all sub-systems need to be synchronized. A global clock is introduced, giving a time-stamp to every device participating in data collection and processing. The clock system uses the Synchronization-Of-Data Acquisition (SODA) architecture which generates a reference time. This time is transferred to all individual devices and has a precision better than 20 ps [80]. The front-ends in most sub-detectors are responsible to amplify the signal and convert it to digital data. At this stage, noise reduction and zero suppression is applied. Data coming from each sub-detector are concentrated and sent to the buffers. In the buffers, the incoming data are separated into groups according to the time information. After that, the buffers send the data to the compute nodes. They offer a large amount of computing power, and thus this is where the signatures of a physics event are obtained. They can compute and combine information like time-of-flight, PID and track reconstruction. Finally, a high-

speed network will transfer all the information to the event farms, where the actual selection of an event is performed. This is the last step of the chain which leads to the storage of the specific event. The event has almost the complete event topology including quantities such as momenta, energies, invariant masses and vertices. The reason for the online processing, is to decide whether to keep or throw away information. At the same time, pre-processed data will also be stored to process them more efficiently and accurately offline.

3.3.2 Software framework

In order to investigate $\bar{\text{P}}$ANDA's performance, a simulation toolkit is available, called PandaRoot. Currently, this toolkit is used for simulations, but it will also be used during the data taking runs. PandaRoot is a combination of the software frameworks FairRoot [81] and ROOT, all based on the C++ programming language. ROOT is an object-oriented data-analysis package developed at CERN from the late 90s until now [82]. It is used for processing, displaying, analyzing and storing physics related data. PandaRoot, was originally developed for the FAIR experiments. It contains the classes which include detector geometries, magnetic fields and in general algorithms related to $\bar{\text{P}}$ANDA's data structure and output [83]. It is used to perform MC simulations, which are used to model the probability of different outcomes in a physical process where the presence of random variables make them hard to predict. Figure 3.15 shows the steps of the simulation and reconstruction chain of PandaRoot.

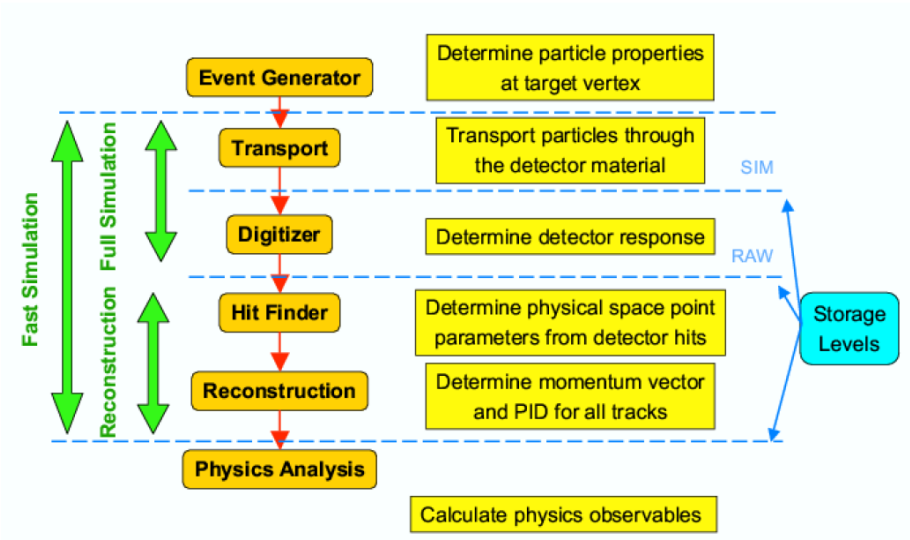

Figure 3.15: Simulation and reconstruction chain of PandaRoot [35].

Event Generators

Event generators produce a stream of events that have been calculated at fixed target or collision experiments according to theoretically-predicted and/or experimentally-proven physics models. The known variables used by the event generators are the masses, momenta, energies, quantum numbers, and lifetimes. PandaRoot mainly includes two event generators, one is called Event Generator (EvtGen) and the other Dual Parton Model (DPM).

EvtGen was developed to simulate events of B decays for experiments like BaBar and Belle [84]. One of the key features of EvtGen is that for an event generation only the amplitudes of the simulated decays are needed. It offers a large number of built-in decay models but also the option for customized decay models. EvtGen is mainly used to generate signal channels and it is the generator used for the analysis presented in chapter 5.

DPM is a generator used to describe high-energy collisions between two hadrons, two nuclei, or a combination of the two [85]. The model used is phenomenologically motivated and can cover non-perturbative as well as semi-perturbative processes at higher energies. DPM is used by the $\bar{\text{P}}$ANDA collaboration to describe background-like events (inelastic and elastic hadronic processes). This is the background model that is used in chapter 5.

Also available in PandaRoot is the Ultrarelativistic Quantum Molecular Dynamics (UrQMD), a model for (ultra)relativistic collisions of heavy ions [86], and the Box Generator (BG), which is used for single particle production depending on angle and momentum.

Particle transport

After the initial reaction has been generated, the particles need to be propagated through the detector and the magnetic field. In PandaRoot, two propagators are available for this purpose: Geometry and Tracking v3 (GEANT3) and Geometry and Tracking v4 (GEANT4). Both are developed by groups involved in CERN experiments but are based on different programming languages: GEANT3 works with Fortran while the more recent GEANT4 is based on C++ [87]. Both propagators include a large number of physics processes to simulate the passage of the particle through materials and the interaction with them. In every step of the particle's path, a calculation of the probability of the physical processes like bremsstrahlung, scattering, decay, etc. is performed.

Digitization, track finding and fitting

The last step in the simulation chain of the detector's response, is the digitization. In each sub-detector, the signals are modified to match the readout characteristics and the goal is to obtain hit information as realistic as possible. Afterwards, track finding is performed, which will form groups of hits that belong to one particle. A track hypothesis is applied in order to find a track candidate. When one is found, a track filter is applied to increase the accuracy of the estimated track parameters. PandaRoot uses the Kalman filter which takes into account the track candidates, the hit information together with the corresponding measurement uncertainty to find the most probable track. The GENFIT package [88], performs all the above steps providing a complete track finding toolkit. GEANE, calculates and handles the error propagation during the tracking process [89]. In addition to that, the particle's type is also determined, by using the combined information provided by different sub-detectors like the $\mathrm{d}E/\mathrm{d}x$ from the MVD and STT, the energy deposited from the EMC, and the Cherenkov light from DIRCs. A probability is then assigned to each one of these particle candidates. Finally, the particles are sorted into lists, which are later used by algorithms to investigate a specific physics channel.

3.4 The FAIR facility

FAIR is an international accelerator facility under construction in Darmstadt. Roughly 3,000 scientists from more than 50 countries are working on the FAIR project. The facility will offer a unique accelerator complex, which will create the opportunity to perform novel experiments with a diverse offering of beams, such as antiprotons, ions, and exotic nuclei. The facility hosts a variety of science-driven communities which are divided into four pillars each one focused on different research areas and scientific topics [90]. The $\bar{\text{P}}$ANDA collaboration is one of the pillars of the new FAIR facility and subject of this thesis. The collaboration aims to study the dynamics of the strong interaction, in particular the structure of hadrons, using the annihilation and scattering of antiprotons with protons and nuclei. The Nuclear Structure Astrophysics and Reactions (NUSTAR) collaboration will investigate stable and short-lived (radioactive) nuclei and reactions amongst them, while the Atomic Plasma Physics and Applications (APPA) collaboration will study atomic and plasma physics as well as material science. Finally, the Compressed Baryonic Matter (CBM) collaboration will study the nuclear-matter phase diagram and the quark-gluon plasma with high-energy heavy-ion beams. Figure 3.16 shows the layout with the various beam lines and the location of the experimental areas dedicated to

the four pillars that form together the FAIR facility.

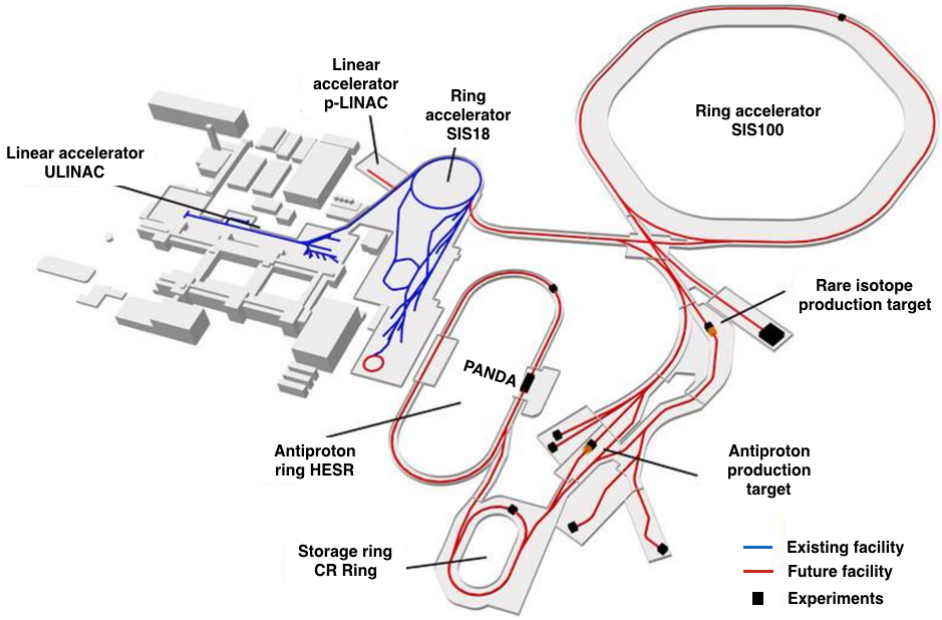

Figure 3.16: The future FAIR facility [91]. On the left the existing GSI infrastructure is shown. Red lines highlight the new accelerator chain and blue the existing ones. The black dots represent various experimental areas. $\bar{\text{P}}$ANDA is located near the center of the figure at the HESR.

The accelerators shown in figure 3.16 will provide different particle and ion beams with different momenta needed for the individual experiments. The initial production of the beam and acceleration will occur in the existing GSI Helmholtz Center for Heavy Ion Research (GSI) facilities. For protons and ions, FAIR will have two distinct linear accelerators, the UNIversal Linear ACcelerator (UNILAC) and the Proton LInear ACcelerator (p-LINAC). Both will inject the particles into the SIS18. UNILAC has been in operation for almost 40 years at GSI, delivering beams with energies between 3-10 AMeV for heavy ions and up to 15 AMeV for light ions. An upgrade of UNILAC will take place in order to fulfil the beam requirements for FAIR. In addition to UNILAC, a new structure for injecting protons will be constructed, the p-LINAC. The protons will be accelerated up to 70 MeV before entering the SIS18. The number of protons injected per cycle will be 7×10^{12}. In total, two synchrotrons will be responsible for the main acceleration of the protons and ions. The first one is the SIS18, already part of the existing GSI accelerator chain, but it will be upgraded for FAIR. It will be able to accelerate light ions up to 2 AGeV, heavy ions up to 1 AGeV and protons to 4.7 GeV. The second in the chain is the SIS100, with a

circumference of 1084 meters, which will be FAIR's main accelerator. The acceleration here will reach 27 GeV for protons and 2.7 AGeV for light ions. In order to use the different beams offered, cooling, storing and extra modifications are needed. All these steps are done in the storage rings [92]. The Collector Ring (CR) will collect antiprotons (which have been created from the interaction of the protons and the target before the CR) and ions from the accelerator rings and perform a stochastic cooling [93]. The $\bar{\text{P}}$ANDA experimental setup will be located in the High Energy Storage Ring (HESR). HESR, is the main working horse for $\bar{\text{P}}$ANDA and thus discussed in more detail below.

3.4.1 Antiprotons in HESR

The HESR (figure 3.17) is a storage ring for high brilliance beams of antiprotons. The high intensity beams will have momenta up to 15 GeV/c and will be phase spaced cooled by both stochastic and electron cooling. It consists of two 180° arc segments and two straight line segments. The total circumference of the ring is 574 meters, while the two straight sections have a length of 125 meters each [94].

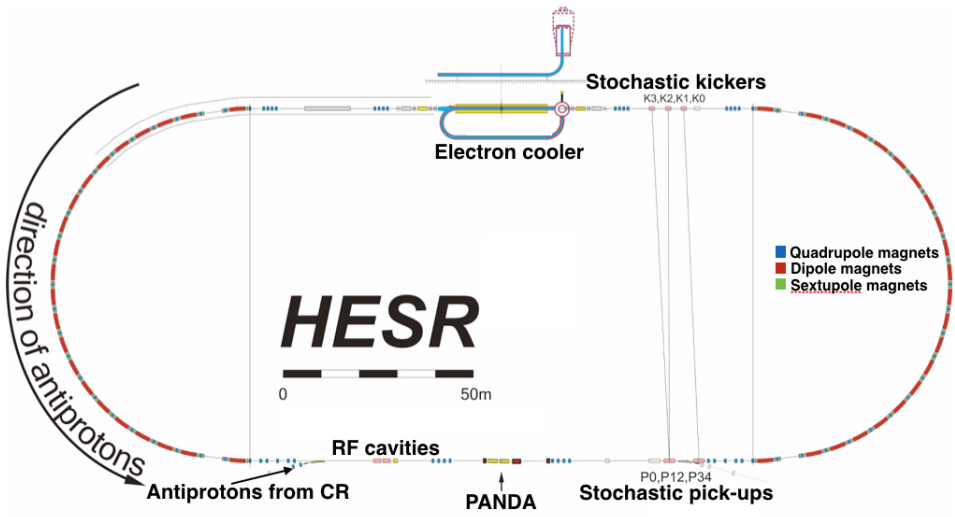

Figure 3.17: Schematic layout of the HESR [95].

There are two operational modes for the ring. The first one is called the High-Resolution (HR) mode, in which the luminosity is in the order of 2×10^{31} cm^{-2} s^{-1} and the antiproton momentum spread is $\sigma_p/p \leq 2 \times 10^{-5}$. The second is called the High-Luminosity (HL) mode, where the luminosity and the momentum spread are 2×10^{32} cm^{-2} s^{-1} and $\sigma_p/p \sim 10^{-4}$, respectively [95]. One of the straight sections is occupied by the electron cooler while the other will host the $\bar{\text{P}}$ANDA experiment and the beam manipulation cavities, injection kickers and septa. The stochastic cooling of HESR will have two parts, the pickup and the kicker [96]. These will be located opposite to each other in the two straight sections and will have a bandwidth of 2 - 4 GHz with an option to upgrade to 4 - 6 GHz. This method of cooling will be used for beam momentum above 3.8 GeV/c. The electron cooling will use an electron beam with energies up to 4.5 MeV. The device will have a longitudinal field of 0.2 T to guide the electrons as they cool the antiproton beam [97]. This feature allows beam cooling for momenta up to 8.9 GeV/c. It is important to mention that, due to time and funding constraints during the first years of data taking, HESR will only operate in the HR mode, meaning that the maximum luminosity reached will be 2×10^{31} cm^{-2} s^{-1} in a momentum range of 1.5 - 9 GeV/c. These two numbers have to be taken into account for the physics cases that are feasible with $\bar{\text{P}}$ANDA during the first years of operation. The open-charm physics and more specifically a measurement of the production cross section of D mesons, which is the subject of chapter 5 in this thesis, is one of the studies that might be able to be performed in the HR mode of HESR.

Chapter 4

Test of the particle-identification capability of a prototype STT detector

One of the main tracking detectors of the $\bar{\text{P}}$ANDA experiment will be the STT. The two main tasks of the STT are the trajectory reconstruction of charged particles and the PID by specific energy-loss measurements, as described in section 3.3.1. Several simulations have taken place in order to examine the performance of the STT [68]. A prototype STT detector was built to test the electronic readout method for the PID, develop the analysis software algorithm and test the performance with beams of different momenta and particle types. In section 4.1, information about the setup will be given. Section 4.2 gives an overview of the beam tests and the hardware settings while sections 4.3 and 4.4 will focus on the results from the individual tests. Finally, in section 4.5 a comparison of the performance from the two tests will be presented together with results along with the discussion.

4.1 Beam tests in Jülich

The development of a prototype STT, along with its performance test, was of crucial importance for the $\bar{\text{P}}$ANDA project. In this direction, the Institut für KernPhysik (IKP) of Forschungszentrum Jülich (FZJ) together with the Akademia Gorniczo Hutnicza (AGH) University in Krakow, combined their ef-

forts to build such a prototype. The contribution of the IKP was mostly to construct the detector part of the prototype and to investigate its performance, while the AGH University was responsible to build and develop the electronics and the readout system of the detector. In the following sections, all the details about the tests performed and the readout system will be discussed.

4.1.1 The prototype STT and experimental setup

In this section, the setup for the two beam tests is presented and discussed. Both tests took place in the COSY-TOF beam area at IKP. The COoler SYnchotron (COSY) provides polarized and unpolarized proton and deuteron beams up to momenta of about 3 GeV/c. For both beam tests, the same prototype STT was used. A photograph of the detector is shown in figure 4.1. The rectangular-shaped prototype consisted of 144 individual tubes, arranged in 6 layers with 24 tubes each, along the beam direction (figure 4.2).

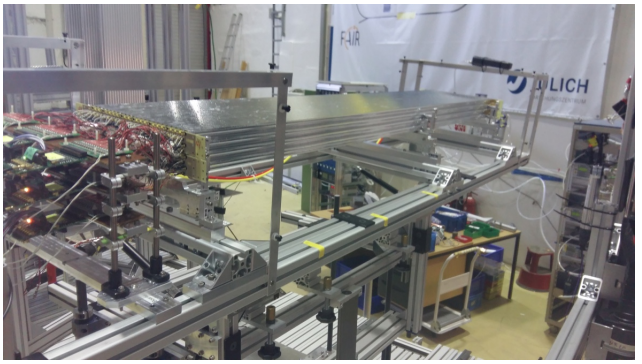

(a)

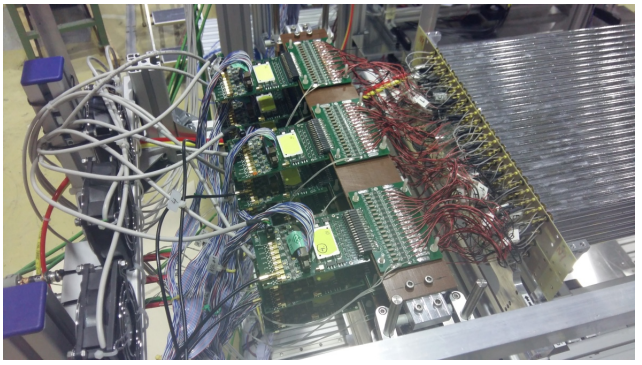

(b)

Figure 4.1: The prototype STT detector. (a) The mechanical frame with the prototype STT. (b) Zoomed view of the prototype STT and front-end electronics.

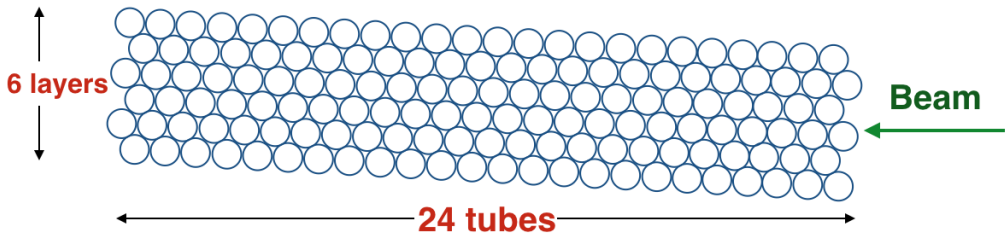

Figure 4.2: Schematic side-view of the STT prototype.

In the two beam tests, conducted in April and December of 2016 (figure 4.3), two different STT prototypes were tested, each one with its own readout system. One was using an ADC readout system (STT2) and the other an ASIC readout system (STT1). The performance of the STT1 system is the subject study of this thesis. A Forward Tracker (FT) prototype for $\bar{\text{P}}$ANDA was also installed, with an ASIC readout system as well. Two drift chambers were mounted in the setup that were used for beam tuning. Four scintillators, labeled as S1, S2, s3, and s4 in figure 4.3, were used as external triggers. Only S1 was used as trigger for the data that were taken for the work presented in this thesis. The timing information from S1 was used as reference time for the readout.

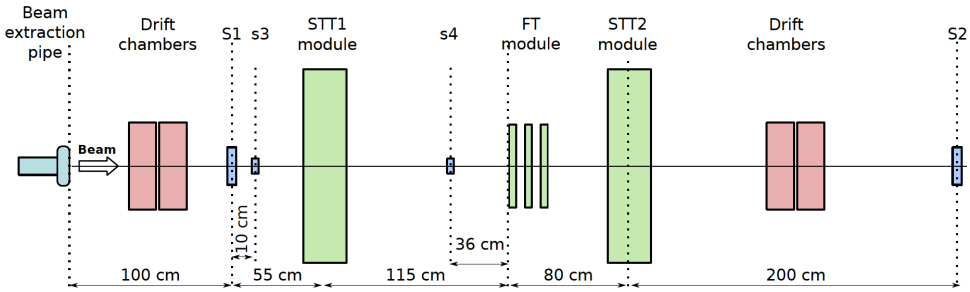

Figure 4.3: Scheme of the experimental setup. The prototype examined in this work is labeled as STT1 [98].

4.1.2 Readout and data acquisition

In this work, the results from the ASIC readout are presented and discussed. The ASIC readout uses the Time-Over-Threshold (TOT) technique [99] in order to measure the energy loss in the straw tubes for the PID by using the signal pulse width. One of $\bar{\text{P}}$ANDA's options is to use the PAnda-STT-REadout-Chip-v1 (PASTTRECv1) for the readout [100], which is an ASIC chip designed for the shaping, discriminating and reading the signals coming from the straw tubes.

The chip with eight input channels has a variable gain (1.8 - 10.5 mV/fC), signal peaking time (10, 15, 20, 35 ns), together with adjustable baseline levels for each individual channel and a common threshold level for all 8 channels. The internal structure of the chip, which can be seen in figure 4.4, consists of an analog and a digital part. The first part is responsible for the signal amplification and shaping while the second part is responsible for the discrimination, the slow control communication and the configuration of the ASIC settings. The digital signal which is the output of the discrimination stage, is further processed and recorded by a follow-up readout system. In our case, the readout system consists of a Time-Readout Board (TRB) which has five Field-Programmable-Gate Arrays (FPGAs) [101]. The central FPGA is responsible for the control of the readout chain and the communication with our data-acquisition computers. The other four "slave" FPGAs are configured to behave as high precision TDCs.

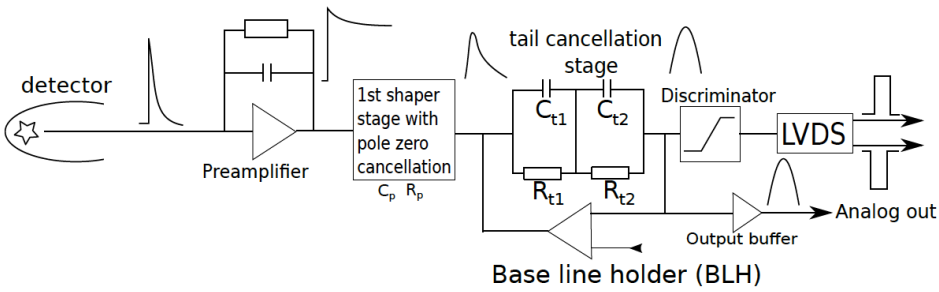

Figure 4.4: The internal structure of the PASTTRECv1 chip. The main components are a preamplifier, a shaper, a tail cancellation circuit and a discriminator [102].

Each one of these TDCs contains 48 channels and it has a time resolution of up to 15 ps (figure 4.5). The digitized signal, coming from the FEE, reaches the TDCs by means of Low-Voltage-Differential-Signaling (LVDS) cables.

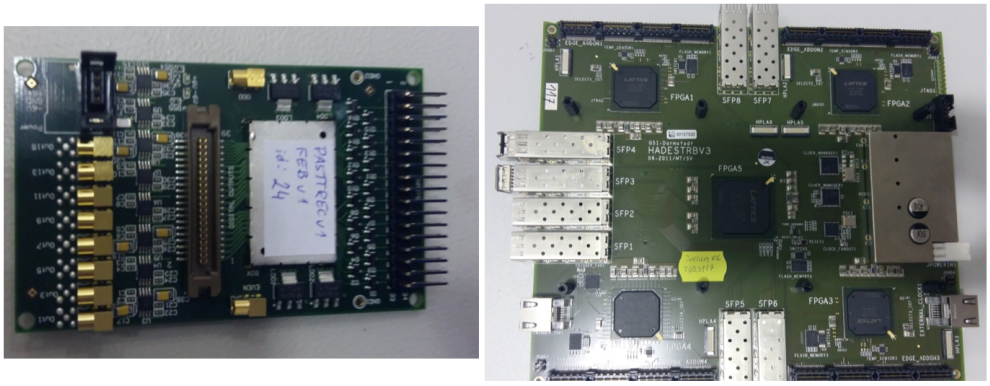

Figure 4.5: Left: FEE with two ASIC chips, which are inside the silver/white box. Right: The TRB3 used during the beam tests. In the corners, the 4 TDCs can be seen.

Figure 4.6 shows the principle of the operation of an individual straw tube when a charged particle is passing through and the basic concept of the readout and data processing. When a charged particle crosses the tube, it ionizes the gas molecules which results in the creation of ion and electron pairs along the path. The electrons drift to the anode wire on positive high voltage in the center of the tube. The first clusters of electrons arriving at the anode wire, and which are registered by the TDCs, will give two values, the leading-edge time and the trailing-edge time. The leading-edge time will be used in the analysis to obtain the so-called isochrone radius, which is basically the closest distance of the track to the straw wire.

As seen in figure 4.6, after setting the common threshold for all channels and the individual baselines of each channel, the leading-edge time is the first point of the signal that is above both values. Similarly, the trailing-edge time is the last point of the signal above both values. The TOT value used for the PID, is simply the difference between the trailing-edge time and the leading-edge time. The TDC ring buffer has a length of 200 μs and can store up to 120 words with 32 bits each. The trailing-edge time and leading-edge time are one word in size as well as the header and the epoch counter used at the ring buffer. The epoch counter is a time counter with a repetition of 10.24 μs. Every time a trigger request arrives (in our case a trigger coming from S1, see figure 4.3), the hits that took place before the trigger are saved and sent by a regular Gigabit Ethernet port to our data-acquisition computers. Since each TDC ring buffer has a length of 120 words, this would mean that it can store up to 60 hits (120 words). However, one word is occupied for the header and since every 10.24 μs we have an epoch counter, in total 200 μs/10.24 μs $\simeq$ 19 epoch counters are

stored. This means that from 120 words, only 100 are available to store hits. In total a maximum of 50 hits can be stored in the ring buffer within the time of 200 μs. This results to a maximum rate of 250 kHz. In $\bar{\text{P}}$ANDA, we expect a maximum rate of 800 kHz per channel in the high-luminosity mode and about a factor of 20 lower rate in the high-resolution mode. The TRB3 will be sufficient for the first years of data taking at $\bar{\text{P}}$ANDA operating in the HR mode. For the nominal $\bar{\text{P}}$ANDA luminosity, an upgrade of the TRB3 hardware will be needed.

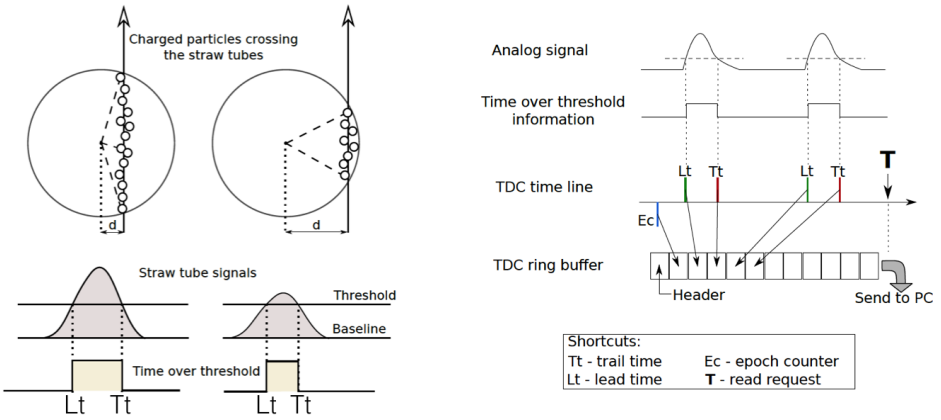

Figure 4.6: Left: The operation principle and readout concept. The parameter d corresponds to the isochrone radius r. Right: The data storing chain of the TDCs [98].

4.2 Overview of the beam tests and hardware settings

The goal of the test was to investigate the performance of the prototype STT, namely the spatial resolution and the PID capability. The prototype STT, the readout system and electronics were described in the previous section. In the first test, proton beams with momenta of 0.55, 0.75, 1.0 and 2.95 GeV/c were used. In the second beamtime, deuteron beams were used. The momentum available was 0.6, 0.75 and 1.5 GeV/c. As mentioned above, the PASTTRECv1 chip can have several settings for the gain and peaking time of the signal [98]. Several different combinations were considered during the beam tests. The results shown in this section correspond to a gain equal to 1.8 and a peaking time (the time needed for the signal to reach the maximum value) equal to 35 ns. Different common threshold levels were also tested, but only results with the threshold set to 20 mV are shown here. The voltage applied was 1800 V, which

is the expected operational value in the $\bar{\text{P}}$ANDA detector. The main results shown are from the lowest momenta of both tests, i.e. 0.55 GeV/c for the proton beam and 0.6 GeV/c for the deuteron beam. In the summary, results from all momenta are given. The values of the settings were selected based on tests made by the group in Krakow. The main criterium for the selection of the settings was the signal shape and more specifically, the minimisation of undershoot or overshoot. The amplitudes of the signals were taken under consideration as well. Results from different gain, threshold and peaking time settings show negligible variations from those that are shown here.
In order to arrive at the final results, several intermediate steps have been performed including calibration and correction of the data and tracking reconstruction. In the next pages, all steps during the data analysis will be described and discussed in detail. Data from the 0.55 GeV/c proton momentum are used for the calibration and analysis. A summary of the results from both tests will be shown in sections 4.3.3, 4.4 and 4.5.

4.3 Data analysis

4.3.1 Calibration procedure

The first check performed is the shape of the leading-edge time distribution. Figure 4.7 shows a typical leading-edge time spectrum where it can be seen that the signal is between -800 to -550 ns. This corresponds to the time window that has been used to select the signal events for further analysis. The peak at -240 ns is the reference time, which in our case is the timing information from scintillator S1 (see figure 4.3).

The signal shape contains information from the settings of the chips, such as the peaking time of 35 ns, since, as one can see, this is the time needed for the signal to reach its highest value. After converting the TDC output into seconds and inverting the time spectrum, the resulting shape, as shown in figure 4.7, is as expected [68].

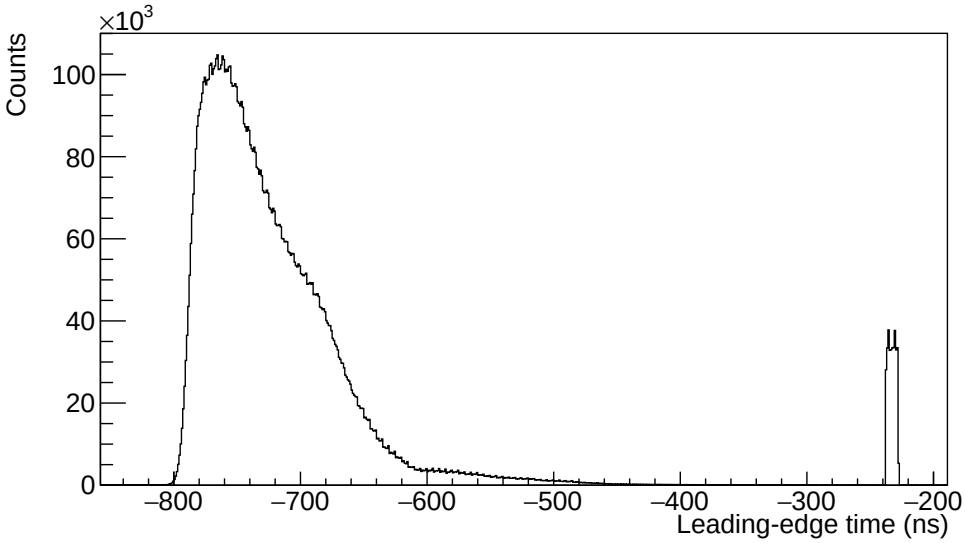

Figure 4.7: The leading-edge time plot from raw data. The window between −800 and −550 ns corresponds to the signal, while the peak at ∼ −240 ns is the reference time.

It is important to mention that both leading-edge and TOT times need to be calibrated. The first step is the calibration (time-offset correction) of the leading-edge times. The method used is based on the value of the maximum bin filled in the leading leading-edge time spectrum per channel. A "threshold" value is calculated based on this value, and a "correction" value is calculated based on the start and end of the leading-edge time spectra as well as accounting for the choice of binning. At the end, the leading-edge time spectra per channel are shifted by this threshold value in order to have all channels starting at 0 ns. These calibrated leading-edge times, are also called drift times. Figure 4.8 shows the distribution of the leading-edge times before and after the calibration.

The group in Krakow developed an automatic procedure for the TOT calibration [98]. This method results in obtaining the individual baseline levels for the channels and thus, set these values for the whole measurement period. This method calculates the mean TOT from all events and channels, and then by iterating several times, simply moves by a step of several ns the TOT value of each channel closer to the mean value of TOT. After several iterations, most of the channels have the same mean TOT. The results after calibration can be seen in figure 4.9.

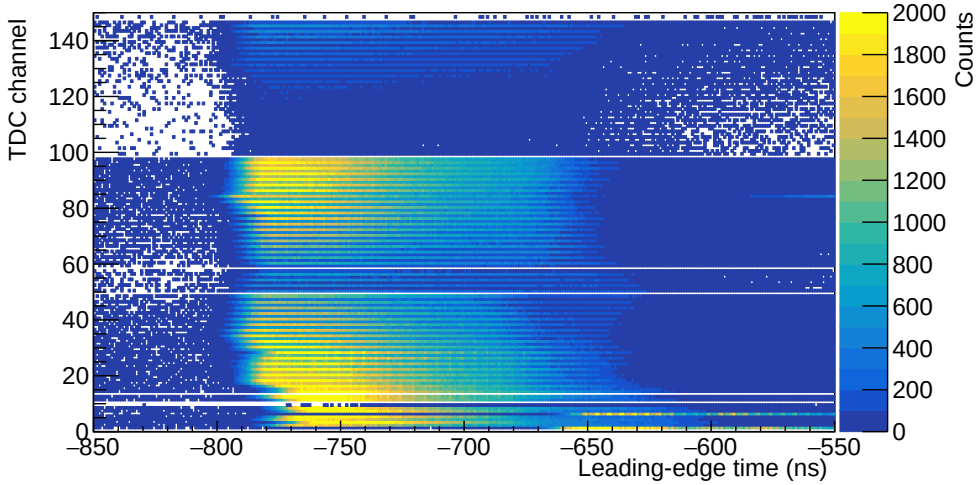

(a)

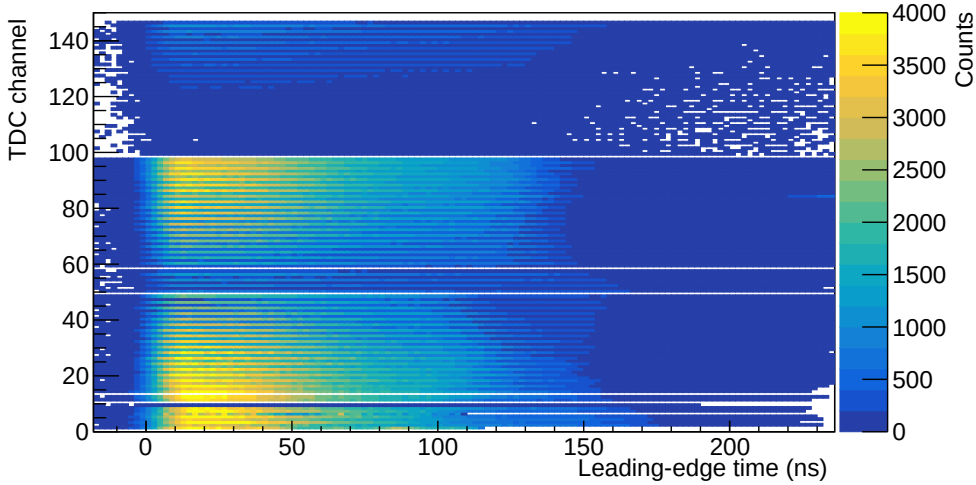

(b)

Figure 4.8: (a) TDC channel number versus non-calibrated leading-edge times. (b) TDC channel number versus calibrated leading-edge times. The starting point for all channels is set to 0 ns by design. After TDC channel #100, no hits are present since the beam did not travel through that part of the detector.

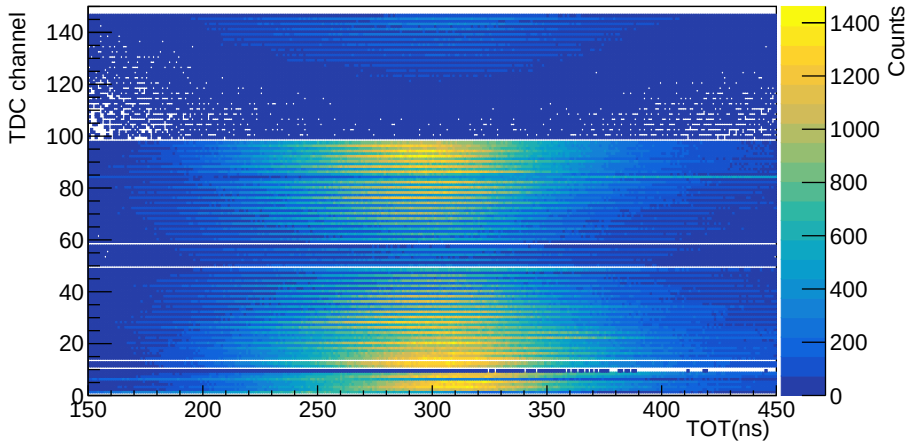

Figure 4.9: TDC channel number versus calibrated TOT times. Good alignment of the mean values of the individual channels is seen.

In figure 4.10, the calibrated TOT times are shown versus the calibrated leading-edge times. The bulk of the data follows the expected correlation between the calibrated TOT and leading-edge times, and the noise levels are below 10%. During the tests, the setup was tilted with respect to the beam, in order to cover all radial distances inside the straws. As seen in figure 4.11, the beam enters the setup from the upper-left part of the prototype and exits from the middle-right part. The last two rows, are barely hit from the beam, while some channels in the first three rows are broken.

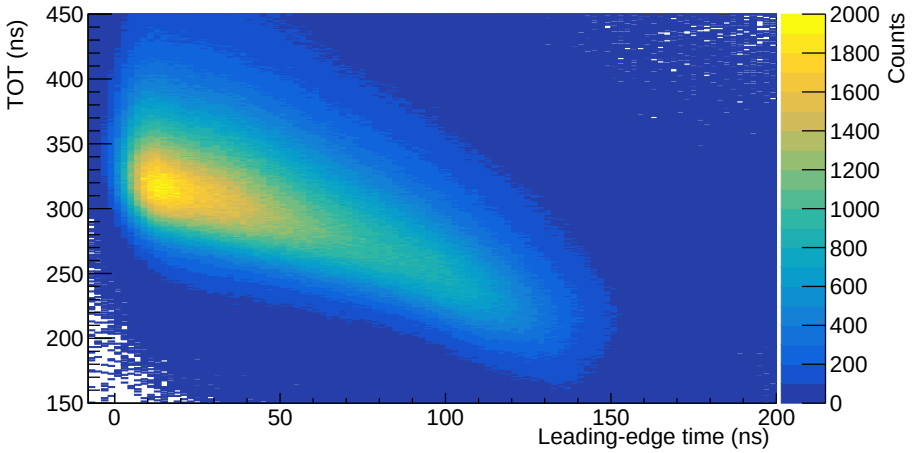

Figure 4.10: Calibrated TOT times versus calibrated leading-edge times.

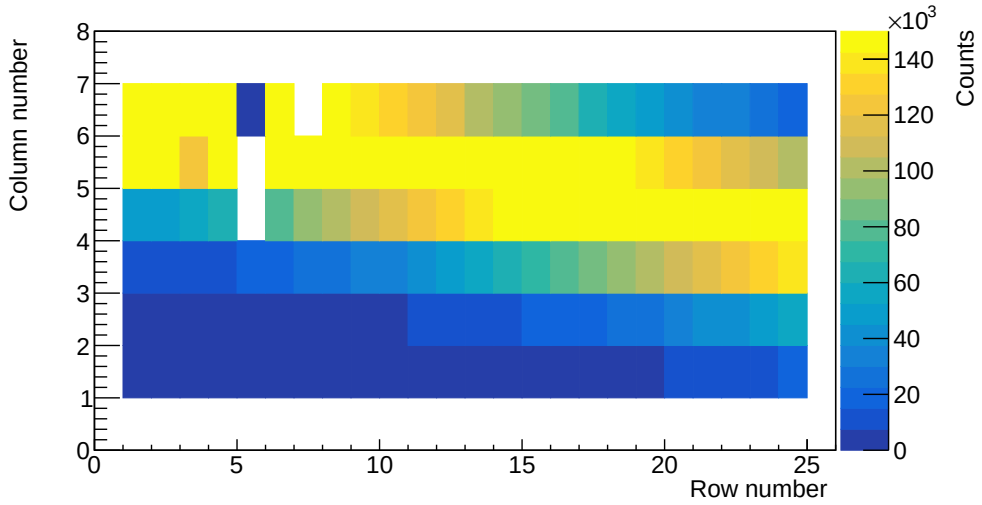

Figure 4.11: Hitmap of one data file. Each individual rectangle box is a tube. The beam enters from the left and exits from the right. The white rectangle boxes represent broken channels.

4.3.2 Event and hit selection in track reconstruction

After the calibration of both leading-edge and time-over-threshold times, the next step is the extraction of the isochrone radius *r(t)* from the drift times *t*. This is done by using equation 4.1, which is based on the hypothesis of a uniform illumination of the tube and a constant efficiency over the tube volume [68]:

$$r(t) = \frac{R_{tube}}{N_{total}} \int_0^t n(t')dt' \ , \tag{4.1}$$

where $n(t')$ is the number of tracks with drift times t' within interval dt', N_{total} is the total number of tracks and R_{tube} is the tube radius.

Taking the finite TDC resolution (bin size) and the wire radius R_{wire} into account, equation 4.1 becomes

$$r(t_i) = (R_{tube} - R_{wire})\frac{\Sigma_i N_i}{N_{total}} + R_{min,a} \ , \tag{4.2}$$

where N_{total} is the sum of all bin entries (N_i) and $R_{min,a}$ is the avalanche radius.

The "avalanche circle" is the area around the anode wire where the electric field is large enough to affect the quality of the signal. In our case this radius is of the order of 100 μm. The obtained results are then parametrized with a 4^{th}-order polynomial, as shown in figure 4.12. The space-time relation will be used to calculate the isochrone radius per hit, which is needed for the track reconstruction and the calculation of the spatial resolution. It is important to mention here that the space-time relation is not entirely accurate for our prototype since the conditions do not fully comply with the requirements for using it, namely, a uniform illumination of the tube and a constant efficiency over the tube volume. The measured drift times have also errors which affect the *r(t)* calculation. In the coming paragraphs, a more accurate and realistic calculation of the *r(t)* relation will be discussed.

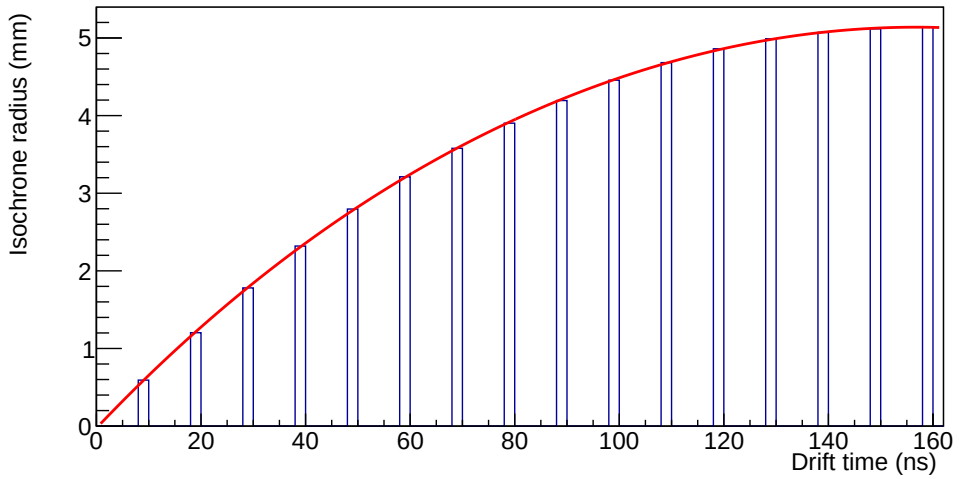

Figure 4.12: The *r(t)* calculation based on equation 4.2. The red line indicates a 4^{th}-order polynomial that has been fit to the data to obtain the parameters of the *r(t)* relation. A tube radius of 5 mm, a wire radius of 20 μm, and an avalanche radius of 100 μm were used.

In every step of the analysis, starting from the raw-data filtering to the final obtained results, at least 12 hits per event/track are required for the event selection. The logic behind this explicit cut is that on average we have 24 hits per track, and thus we require to have a hit efficiency of at least 50% for our final track reconstruction and at the same time avoid spurious hit events. This will lead to a calculation of the spatial resolution which will only be affected by the resolution of the tubes and not the tracking procedure itself.

The steps during the track reconstruction are summarized below.

- Calculation of the isochrone from the measured drift times using the calibrated space-time relation.
- If the isochrone calculation gives values between -200 μm and 0, then the value is set to 200 μm. This is to allow time deviations to negative values up to 5-10 ns and to make sure that the value of the isochrone radius is far from the avalanche area (located approximately at 100 μm).
- For the determination of the pre-track, we take the following analysis steps. Since there is no magnetic field, only straight tracks are passing through the detector. The first and the last channel of an event are considered first. These two channels would be the entrance and exit tubes that were on the path of the beam. For these two, after the calculation of the isochrones, there are four possible positions of the track, two for each tube. Thus, in total four tracks are possible candidates to be the "real" track. All four possibilities are considered as valid track candidates as shown in figure 4.13. Subsequently, all the intermediate tubes are taken into account by calculating the distance of the isochrones to the track candidates. A fit is performed to each of these tracks, and the one giving the lowest χ^2, or in other words, the one that has the smallest mean distance between the track and the isochrones, is the final pre-track.

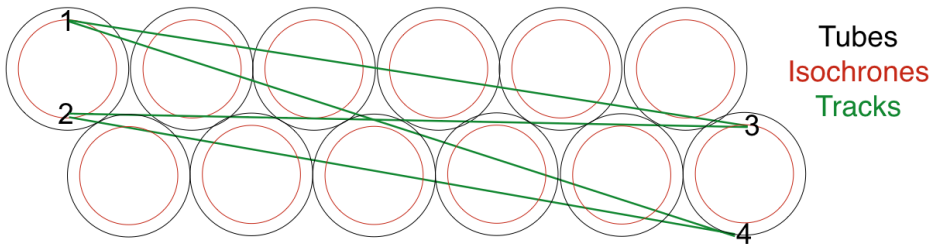

Figure 4.13: Schematic representation of the selection of the pre-track.

- In the final pre-track, the distance between the track and the wire of the tube, is calculated. If this distance is larger than 6 mm, then the hit is excluded from the calculations. This filter is called "outlier 1". The use of this filter is to ensure that no second track hits are taken into consideration.
- After the removal of the hits that do not comply with the first filter, a minimization function called TMinuit is applied. TMinuit is the realization of a minimization function, which tries to find local minima by iterating many times. In our case, the isochrone-radii information together with the slope and intercept of the track, are the key elements for the minimization.

- The new "minimized" track is fitted and the distance between the track and the isochrones is calculated. If this distance is larger than 600 μm, this hit is excluded from the analysis. This filter is called "outlier 2".
- As a next step, a minimization function is applied to the track, with the hits that survived the first and the second filter.
- With the new track, the residual for each hit is calculated. The residual is simply the distance of the track to the calculated isochrones. If this value is larger than 2.5 times the isochrone error (more details about the calculation of the error will be given later), this hit is also skipped. This last filter is called "outlier 3". Filters two and three are rough cuts, whose values are based on a balance between spatial resolution and efficiency. We require that the event efficiency is at least 80%.
- A minimization function is applied for a third and final time. The track calculated this time is the final "best" track, and the calculation of the spatial resolution and the PID are based on this track.

The number of outliers per event and the total number of outliers is shown in figure 4.14. The total number shown is calculated by the addition of the three different outliers per event. For example, if one assumes 2 outliers from the first filter, three from the second and 1 from the third, this will give 6 in total. What is seen in figure 4.14 is that most of the events have a low number of total outliers while the ones that have a relatively large number ($>$ 10-15) are most likely indicating events with more than one track. This can be also seen in figure 4.15 where the number of hits per track before the filtering from the track reconstruction is relatively high. The cut on the required minimum number of hits per event ($>$ 12) is clearly visible.

The steps described above have to be repeated several times since for the first determination of the pre-track the *r(t)* information derived from equation 4.2 was used. At the same time a constant isochrone error of 250 μm was also used. To improve the fit, a data-driven and iterative procedure was performed to find a better estimate of the isochrone error as a function of the isochrone radius. Close to the wire, the error should be larger than close to the tube wall, since the avalanche effects influence our resolution and worsen the errors in the calculation of the isochrones. The isochrone radius is allowed to take values between 0 - 5.4 mm (a maximum value of 5.4 mm is used in the analysis, since there could be small deviations due to the pressurized tubes). After the selection of the final track, the residuals from all channels are computed. Afterwards, the isochrone radius is divided in 10 equals segments of 540 μm and the residuals are calculated in each of these segments. We fit a Gaussian to the distributions, and we take the standard deviation to be the error. A 2^{nd}-order polynomial is then

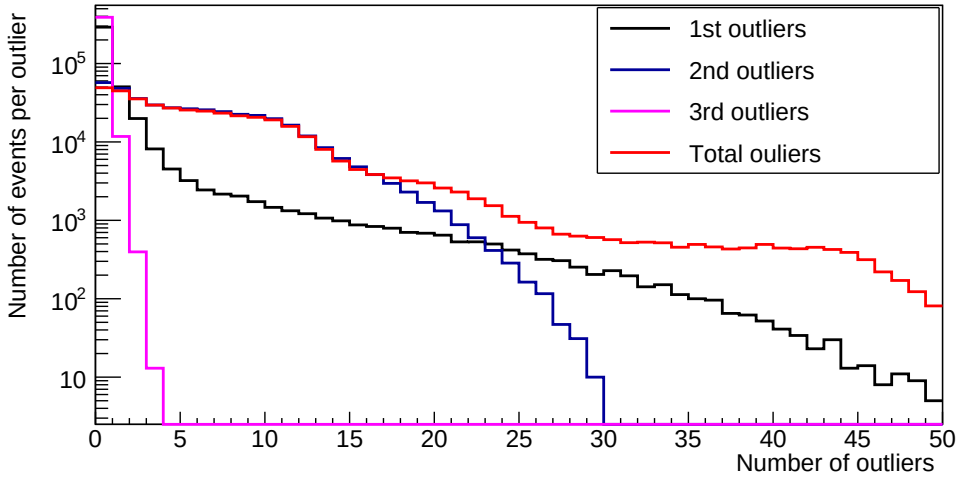

Figure 4.14: Number of outliers per event during "filtering". The total number of outliers shown is calculated as a cumulative variable.

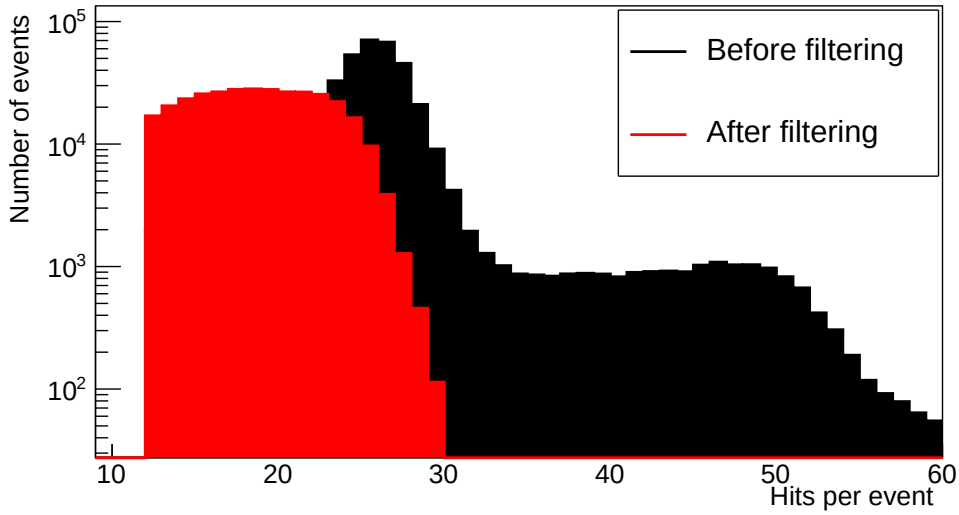

Figure 4.15: Number of hits per track before and after event filtering. Black distribution shows the number of hits per before filtering. Few events have a higher number of hits per track (>40), which indicates that there is a second track present. Red distribution shows the multiplicity after filtering. The steps are discussed in more detail in the text.

fitted to these errors as a function of isochrone radius. The parameters obtained in the fit are used to calculate the isochrone errors. It is also worth mentioning that close to the wire, the avalanche effects are visible, since the calculation of the isochrone error is not realistic in the vicinity of the wire. This is the reason why we do not consider the first segment in the fit. Figure 4.16 shows the isochrone error calculation after track reconstruction for the 1^{st} (where a constant error was used as well as the *r(t)* information from 4.2) and last (3^{rd}) iteration.

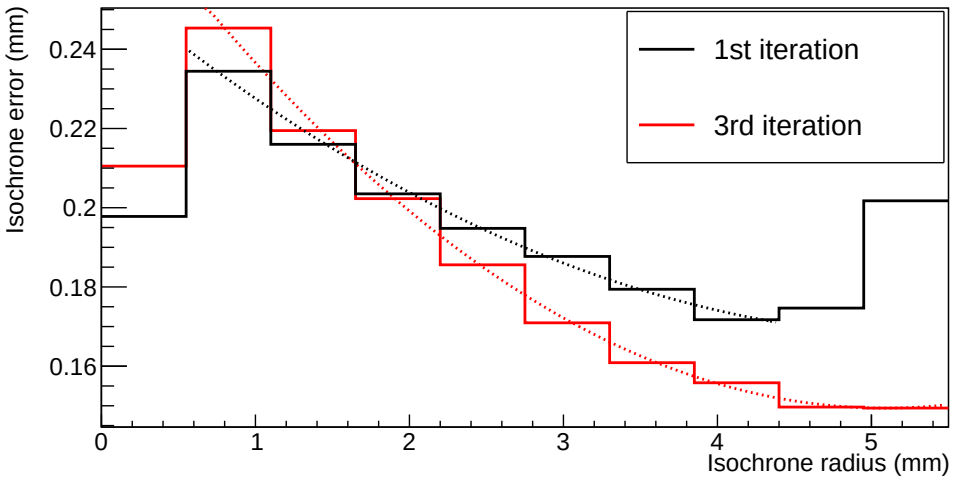

Figure 4.16: Isochrone error versus isochrone radius. The black histogram corresponds to the distribution obtained after 1^{st} iteration and the red histogram after 3^{rd} iteration. The dotted black and red lines represent a 2^{nd}-order polynomial fit through all values of the isochrone radius except the first segment.

The probability distributions of the track fitting of these two scenarios are shown in figure 4.17. It can be seen that the calculation of the isochrone error is more realistic after the iteration procedure, as it becomes smaller when one gets closer to the tube wall. The iterative procedure is also used for the recalculation of the *r(t)*-function from the data. An additional (4^{th}) iteration gives no significant effect on the result and no further improvement was found.

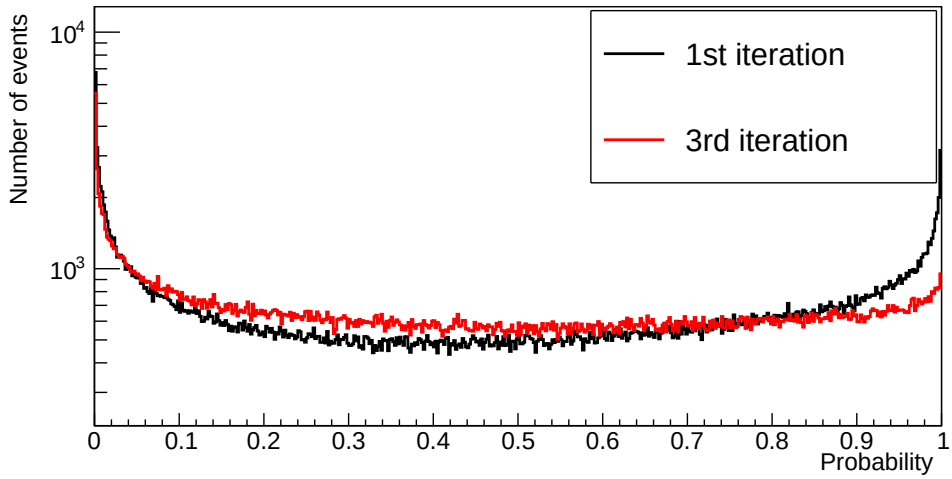

Figure 4.17: Probability distributions of the track fitting. The black and red histograms show the distribution after the 1^{st} iteration and 3^{rd} iteration, respectively. For the latter case, the distribution is closer to what is expected for a Gaussian error distribution of width given by the isochrone error in figure 4.16.

Figure 4.18 shows the final *r(t)* distribution after the 3^{rd} iteration. The parameters obtained from a 4^{th}-order polynomial fit through this distribution, are used for the final track fitting.

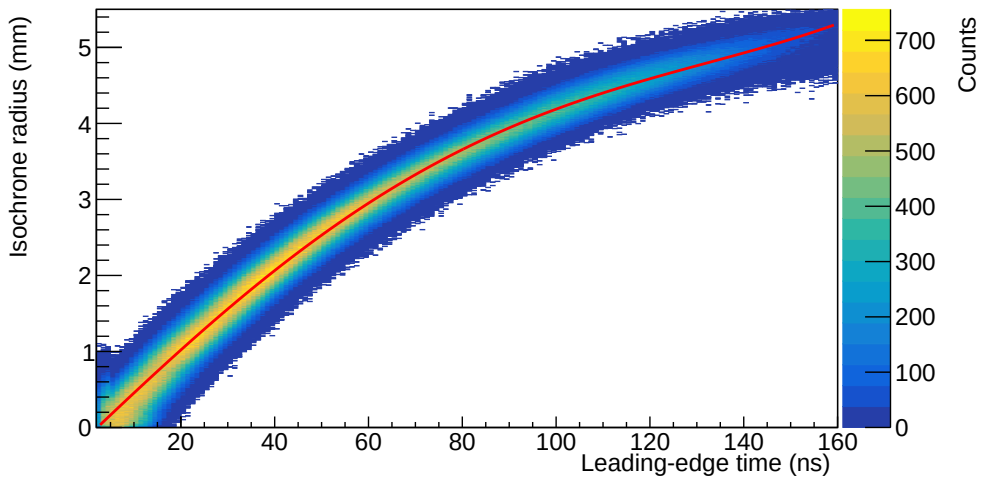

Figure 4.18: The final *r(t)* calculation. Red line indicates a 4^{th}-order polynomial that has been fit to the data to obtain the parameters used for the final track fitting.

4.3.3 Performance study of the spatial resolution

In this section, the results obtained for the spatial resolution from both tests are shown. The distance between tracks and isochrones, which we call residual, will give us a measure of the spatial resolution. The Full-Width-at-Half-Maximum (FWHM) divided by 2.355 (we will call this value σ_{FWHM}) is used to estimate the spatial resolution. This value is used to mimic the standard deviation of a Gaussian distribution. In total, there are 7 spatial resolution values calculated for the different beam momenta of the two tests. In three of them, the value of the standard deviation of a Gaussian fit agrees with the σ_{FWHM} value. In the remaining four, there is a deviation between 3 to 20 μm.

Figure 4.19 shows the final result for the spatial resolution for the 0.55 GeV/c proton beam. The σ_{FWHM} is found to be of the order of 195 μm, which is larger than the expected value of 150 μm obtained from simulations [68]. This value is based on Garfield simulations, where all the relevant aspects (readout, gas mixture, voltage, size of tubes, etc.) were taken into account. Figure 4.20 shows the residual calculated per channel, where it can be clearly seen that several channels have large residual values and that the mean of the distributions is not centered around zero. This is also a strong sign of mechanical imperfections of the prototype and it could be related to problems with the readout.

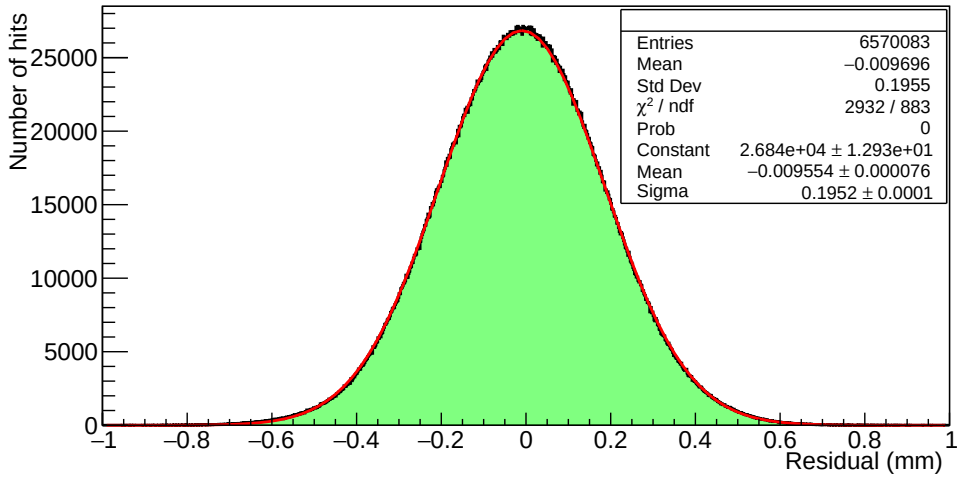

Figure 4.19: Spectrum of the residuals for the 0.55 GeV/c proton beam. The σ_{FWHM} is 195 μm.

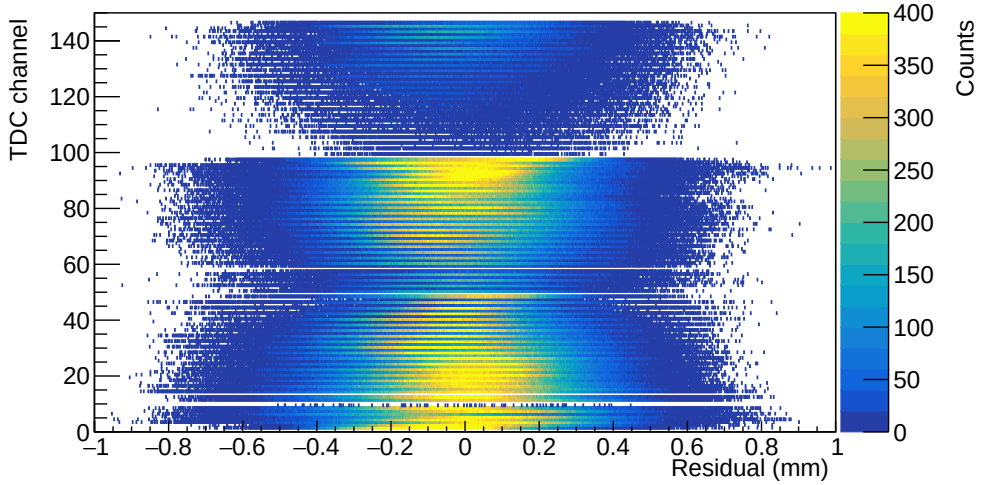

Figure 4.20: TDC channel number versus residuals for the 0.55 GeV/c proton beam.

Figures 4.21 and 4.22 show the residual distribution and the channel versus residual distribution for the 0.6 GeV/c deuteron beam, respectively. A σ_{FWHM} of 177 μm is obtained for the 0.6 GeV/c deuteron beam.

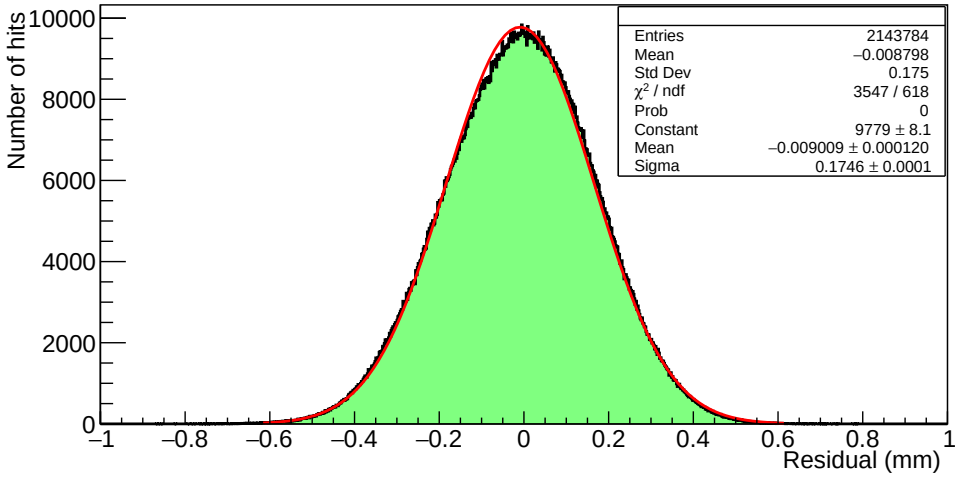

Figure 4.21: Spectrum of the residuals for the 0.6 GeV/c deuteron beam. The σ_{FWHM} is 177 μm.

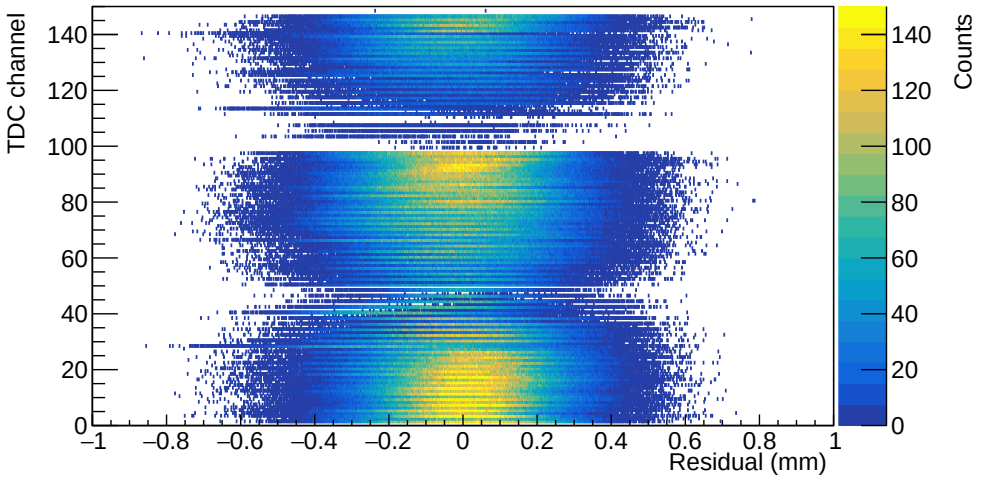

Figure 4.22: TDC channel number versus residuals for the 0.6 GeV/c deuteron beam.

It is important to mention here, that there are noticeable deviations between channels regarding the spatial resolution. Figure 4.23 shows channel 92 which has a σ_{FWHM} of the order of 157 μm, from the 0.55 GeV/c proton beam. The value of this channel is significantly better than the one obtained for the whole prototype (195 μm). The reason for this behavior is investigated and discussed in section 4.3.4.

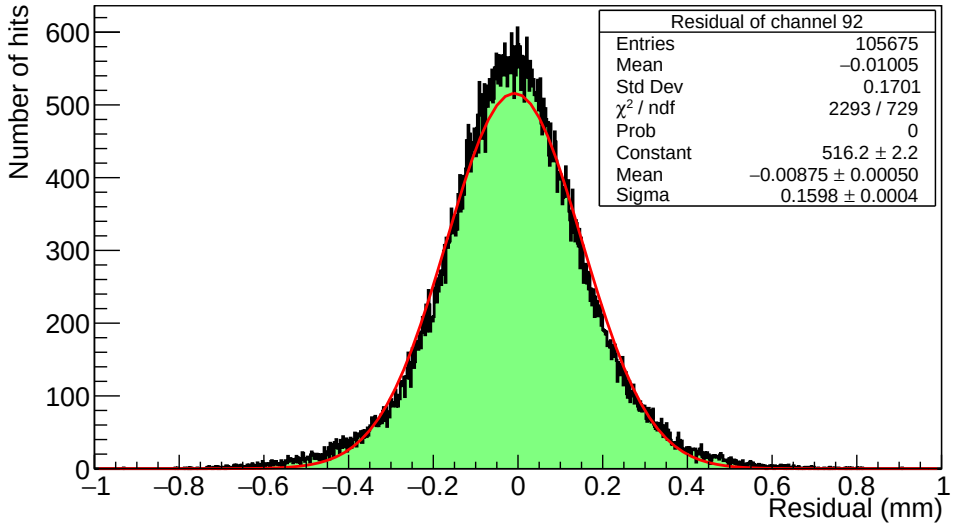

Figure 4.23: Spectrum of the residuals for the 0.55 GeV/c proton beam for channel 92. The σ_{FWHM} is 155 μm.

It is worth mentioning that, the values of the spatial resolution are not only affected by the possible mechanical imperfections but also from the information obtained from the "avalanche" area. In figure 4.24 the spectrum of the residuals for the 0.65 GeV/c deuteron beam for the region between 0 and 300 μm around the wire is shown. The obtained value for the spatial resolution is of the order of 195 μm, which is worse that the one shown in figure 4.21. On the other hand, if the isochrone radius is selected to be between 0.5 mm and 5 mm, the spatial resolution is of the order of 160 μm as shown in figure 4.25, which is better than the 177 μm shown in figure 4.21.

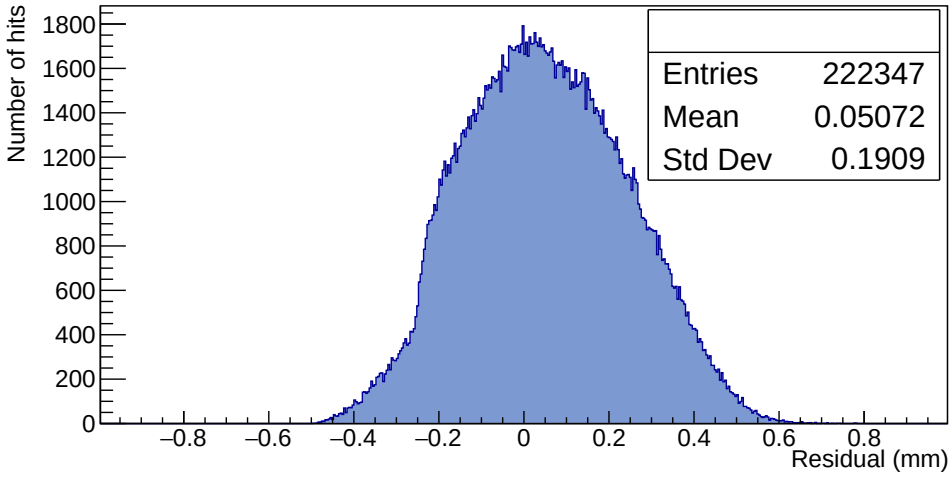

Figure 4.24: Spectrum of the residuals for the 0.6 GeV/c deuteron beam for isochrone radii between 0 and 300 μm. σ_{FWHM} is 195 μm.

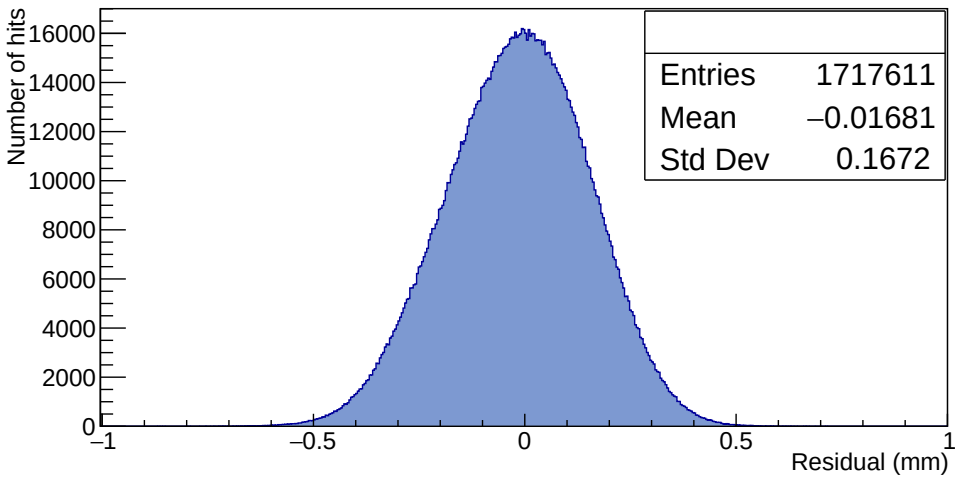

Figure 4.25: The spectrum for the residuals for the 0.6 GeV/c deuteron beam for isochrone radii between 0.5 and 5 mm. σ_{FWHM} is 160 μm.

4.3.4 Investigation of the prototype behavior

During the data analysis of the proton beam, several channels were found to have unreasonable leading-edge time and TOT distributions. Figure 4.26 shows a channel with a reasonable leading-time spectrum.

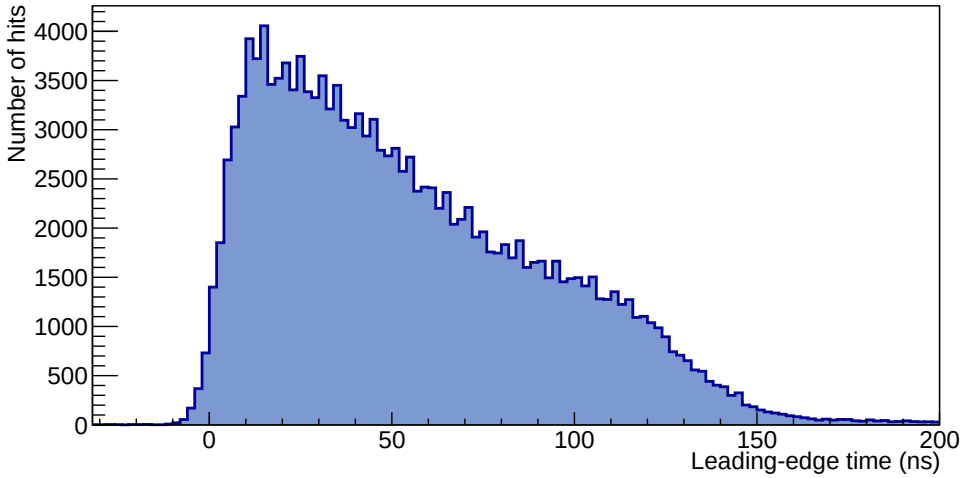

Figure 4.26: Leading-edge time distribution for channel 34 for the proton beam of 0.55 GeV/c momentum. The shape of the distribution is as expected.

The signal shape is similar to the one obtained from simulations [68]. Figure 4.27 shows two channels with a strange behavior. The upper one has a completely unreasonable distribution with a sharp cut at 115 ns and several peaks, while the lower has a "second" leg at 120 ns. The shape of the upper one is most probably due to problems with the readout and the ASIC chip, while for the second one the most probable cause is an imperfection on the position of the wire inside the tube. For example, if the wire inside the tube is placed lower than it should be, then there will be a lot of short leading-edge times for cases when the beam passes through the lower part of the tube, and many unreasonable long leading-edge times when the beam passes through the upper part of the tube. Problematic cases while studying the TOT distributions were also observed. Figure 4.28 shows a channel with a reasonable TOT distribution while figure 4.29 depicts a channel with an unusual spectrum. In total 24 channels out of 144 were found to have a strange behavior. These channels were removed from the analysis presented here. It has also been shown that changes in the behavior of the readout system were observed during data taking [103]. This means that the measuring conditions were not stable. The source of this problem is still under investigation.

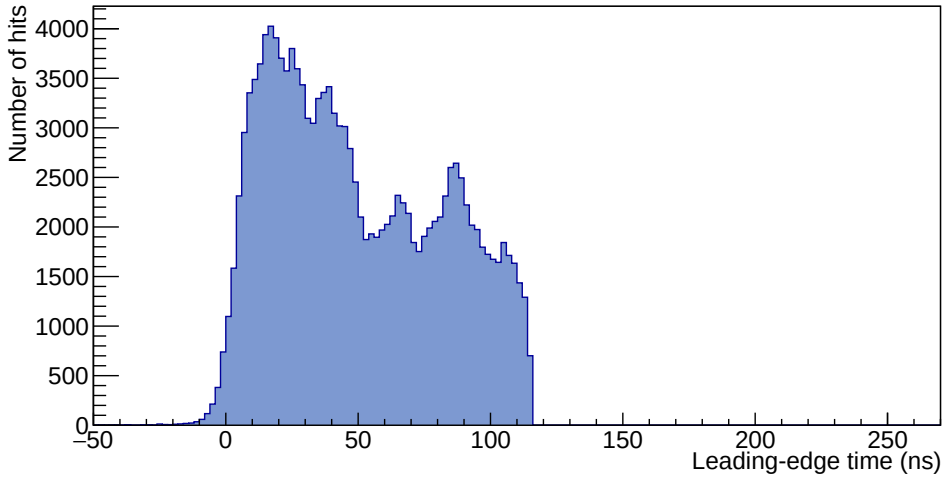

(a)

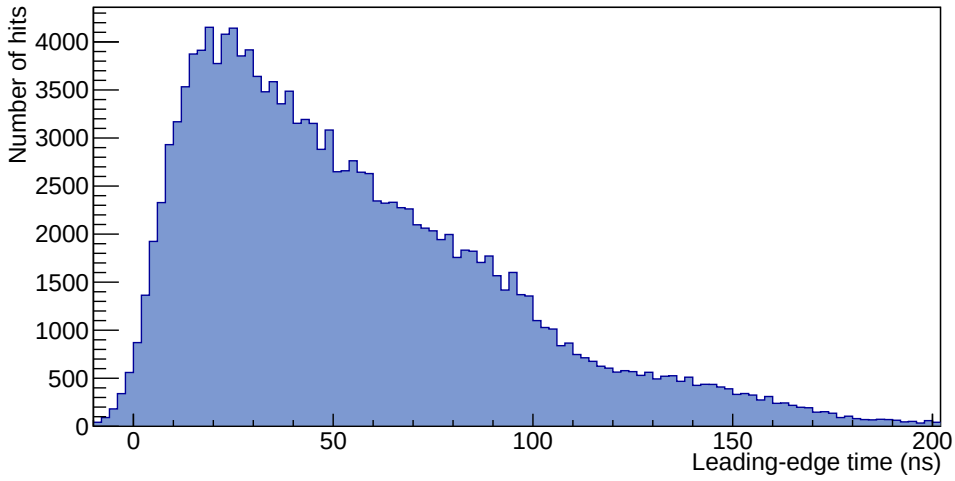

(b)

Figure 4.27: Channels with problematic leading-edge time distributions for the proton beam of 0.55 GeV/c momentum. (a) Channel 6 has a sharp cut at 110 ns together with an unreasonable behavior with several peaks. (b) Channel 75 has a "second" leg effect.

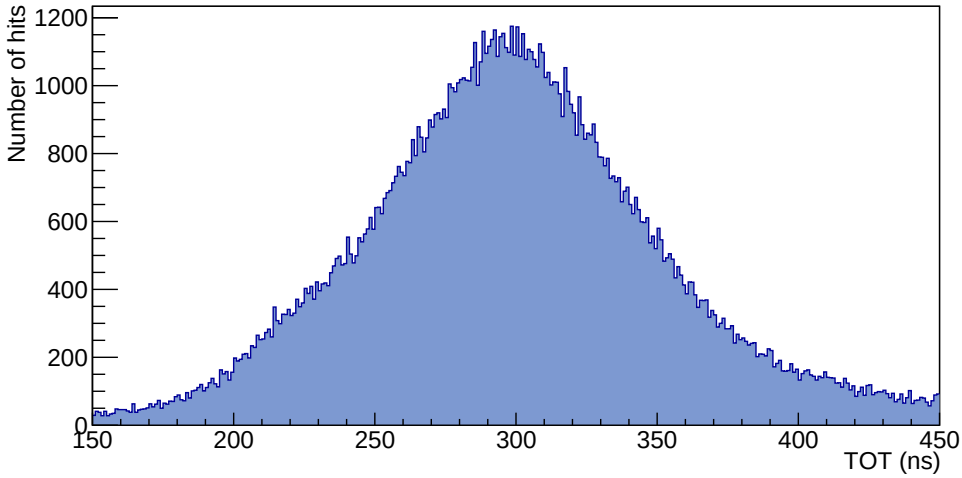

Figure 4.28: TOT distribution of channel 78. The shape of the distribution is reasonable.

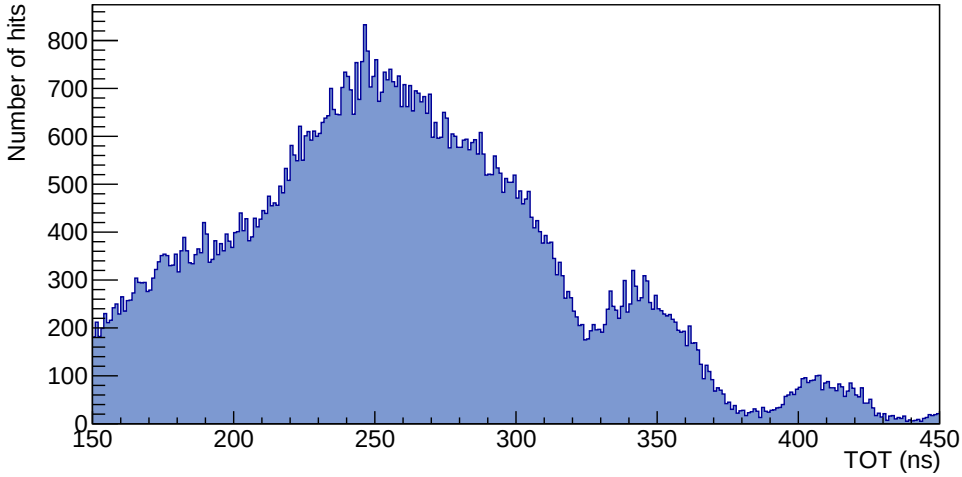

Figure 4.29: TOT distribution of channel 6. An unusual shape is visible.

After the "cleanup" of the channels, the same analysis is performed to check whether the results are better than before. The steps followed are exactly the same as in the previous section and the same cuts have been applied. The only difference is that the hits from the problematic channels are not taken into account for the calculations. Figure 4.30 shows the final result for the 0.55 GeV/c proton beam. The spatial resolution obtained now is 172 μm which is

better than the result (195 μm) presented in the previous section. It is clear that the imperfections of the prototype and the problems with the readout and the electronics affect our results. These problems have to be fixed in order to assure that the results obtained are clean from any "external" sources.

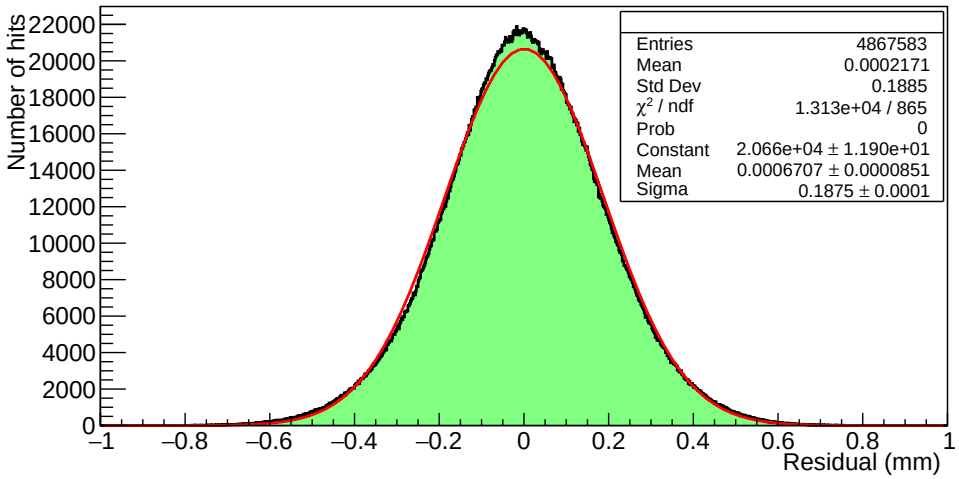

Figure 4.30: Spectrum of the residuals for the 0.55 GeV/c proton beam after the "cleanup". The obtained resolution is 172 μm.

4.4 Particle-identification performance

The ASIC readout will use the TOT information for the PID. More specifically, the TOT/dx information, where dx is the distance traveled by a particle within our prototype, will determine the PID capability of the prototype. From the final track, the TOT/dx value is calculated for each hit. The value used for the evaluation of the PID performance is called *pidf* and it equals to

$$pidf = \frac{\Sigma_i TOT_i}{\Sigma_i dx_i} \ , \tag{4.3}$$

where i refers to the number of hits.

In order to get the best separation power between different momenta and particle species, we optimised the resolution using a truncation method per hit. Figure 4.31 shows the *pidf* values for the 0.55 GeV/c proton beam with different truncation factors while figure 4.32 shows the results for the 0.6 GeV/c

deuteron beam. For all momenta and particle types, the best resolution, is given by applying 30% truncation to the right side of the distribution (removal of large TOT/dx values). The achieved resolution for the *pidf* is between 6 to 8%. A summary of the results for all momenta for both beams will be shown in the last section.

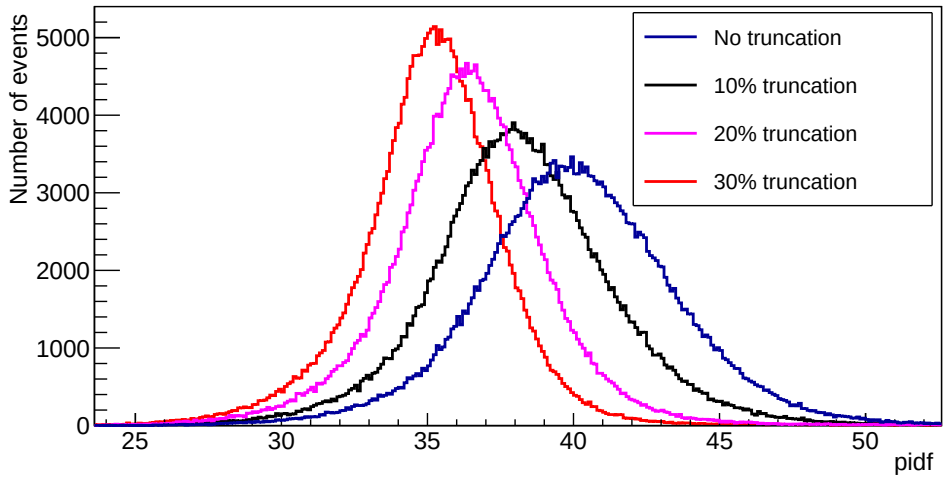

Figure 4.31: *pidf* distributions for the 0.55 GeV/c momentum proton beam. Each histogram corresponds to cases in which a different truncation factor has been applied.

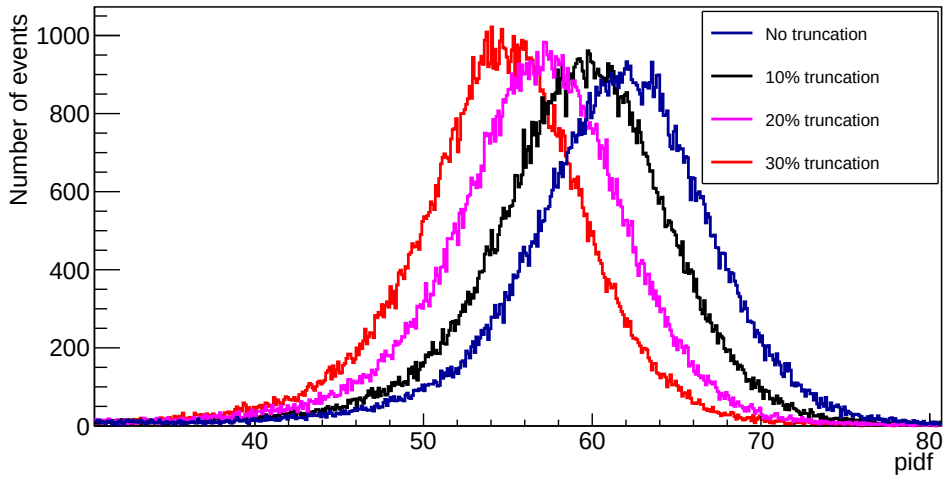

Figure 4.32: *pidf* distributions for the 0.6 GeV/c momentum deuteron beam. Each histogram corresponds to cases in which a different truncation factor has been applied.

4.5 Summary and discussion

In this section, the performance of a prototype STT detector was studied extensively during two beam tests, one using a proton beam and one a deuteron beam. In both tests, the same prototype was used together with the same readout and electronic systems.

The final results for the spatial resolution and the PID capability through the TOT/dx method were presented. The readout system worked as expected, while some problems encountered during the tests (problematic ASIC chips or FEEs) were solved or can be solved in future experiments. The main goal of the tests was to examine the PID capability of the prototype, i.e how well it can separate particles of different species. The second main goal was to calculate the spatial resolution that can be obtained and compare it with the value calculated from simulations. The results obtained have shown that both goals have been achieved to a great extent (spatial resolution is 10% far from the design goal, while PID performance is also quite close to the design goal as explained below).

Improvements on the analysis methods can help us to achieve or even surpass the design goals. One can perform an even more detailed investigation of the individual channels. This should include position alignment of each tube and wire re-positioning inside the tubes. Moreover, an individual estimation of the *r(t)* for each channel could provide a more accurate calculation of the isochrones which will lead to a better spatial resolution. The ideal performance of the electronics and the readout elements will also contribute to better and more reliable results. Last but not least, the mechanical imperfections of the prototype setup must be corrected as much as possible.

Table 4.1 summarizes the spatial resolution values obtained for all different momenta and both beam particle species. It can be seen that the results for the deuteron beam are much better than those of the proton beam. There is a momentum dependence on the values of the spatial resolution. When reaching the minimum ionizing momentum, the sensitivity of the readout to the first clusters of electrons reaching the wire is less, and thus, the resolution becomes worse. The "cleanup" approach performed in the proton beam data gives slightly better results than without the "cleanup". However, the results for the deuteron beam are still much better. This is expected, since during the proton beam time, more problems were encountered, both with the setup and the readout system and electronics. Many of these problems were solved before the deuteron beam test, which is reflected in the final results.

Spatial resolution		
Momentum (GeV/c)	Proton with "clean up" (μm)	Deuteron (μm)
0.55	172	—
0.60	—	177
0.75	198	170
1.00	223	—
1.50	—	188
2.95	265	—

Table 4.1: Values obtained for spatial resolution obtained for all momenta and beam types. The value used for the calculation is the FWHM divided by 2.355.

The PID performance of the prototype can be rigorously tested since we used two different particle types (protons and deuterons) at similar momenta. One can see from figure 4.33 that the separation between protons and deuterons at 0.75 GeV/c is quite satisfactory.
Usually, the separation power S between two particles of type "1" and "2" characterizes the performance of an identification technique. It is obtained from the following equation [68]:

$$S = \frac{|pidf_2 - pidf_1|}{\sigma_1/2 + \sigma_2/2}, \tag{4.4}$$

where *pidf* is the value used for the PID and σ is the FWHM value of the distribution divided by 2.355. For the proton and deuteron beam at 0.75 GeV/c, the separation power calculated is equal to 6.3. Figure 4.34 shows simulated data of the separation power that were performed in the past [68]. Unfortunately, the simulations did not include the separation power for proton with respect to deuterons, and, hence, a solid comparison with our results cannot be made. However, one could compare the separation value obtained at 0.75 GeV/c between protons and deuterons with the separation power calculated from simulations between protons and kaons at 0.375 GeV/c (deuteron has almost 4 times the mass of a kaon and thus the corresponding momentum investigated should be 0.75 (GeV/c)/$\sqrt{4}$, i.e. 0.375 GeV/c). The separation power for the p/K is around 8 at 0.375 GeV/c, and the one obtained from the tests for the p/d at 0.75 GeV/c is 6.3, which is close to the design goal.

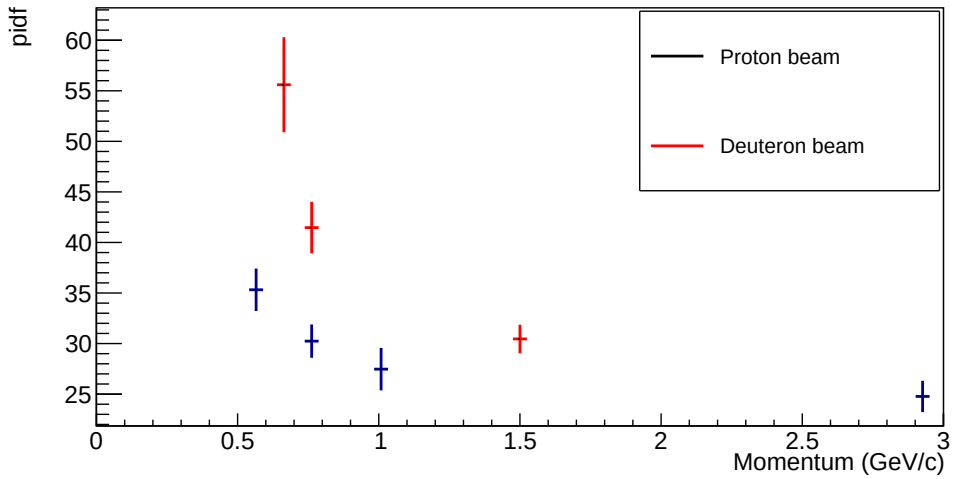

Figure 4.33: *pidf* values with 30% truncation for all momenta and beam types. The size of the vertical error bars represent the FWHM/2.355 values.

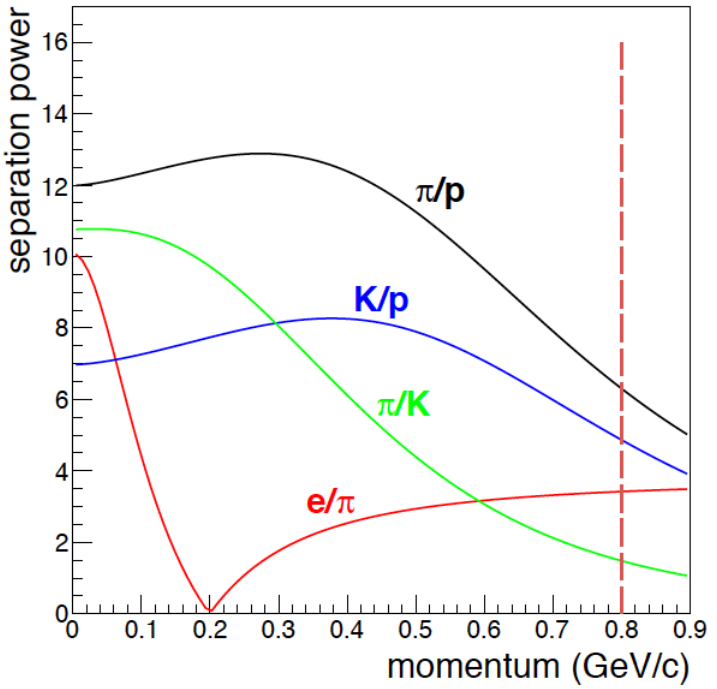

Figure 4.34: Separation power of the STT obtained from simulations [68]. The vertical red-dashed line represents the upper limit in momentum for which the STT can perform PID.

Chapter 5

Feasibility studies for the observation of open-charm mesons with $\bar{\mathrm{P}}$ANDA

In this chapter, the feasibility of studying the decay chain $\overline{\mathrm{p}}\mathrm{p} \rightarrow \mathrm{D}^0\overline{\mathrm{D}}^0 \rightarrow \pi^+\mathrm{K}^-\pi^-\mathrm{K}^+$, is presented and discussed. The process has been studied using Monte Carlo (MC) simulations. The chapter is structured as follows. First, the motivation for investigating the open-charm production is outlined. Then, the event generation is presented followed by the event reconstruction and the study of the detector performance. The reconstruction is performed in two different ways, namely, inclusively (single D-meson reconstruction) and exclusively (D-meson pair reconstruction). Subsequently, the background studies are discussed and presented and finally, the feasibility for the observation of the open-charm mesons with $\bar{\mathrm{P}}$ANDA is examined. The last section is allocated to a summary and discussion.

5.1 Motivation

Open-charm physics is one of the topics of the $\bar{\mathrm{P}}$ANDA physics program (see section 3.1). The spectrum of these states is very interesting and mysterious at the same time. Many of the open-charm states that have been discovered have masses far from the theoretical predictions. Moreover, the mass splitting in the nuclear medium for these states is also of great interest. Last but not least, there are several interesting resonances which mainly decay to a pair of open-charm (more specifically, D) mesons. To investigate these phenomena, a large

number of open-charm states needs to be produced whereby a huge background yield has to be suppressed. $\bar{\text{P}}$ANDA's capability to identify pairs of open-charm mesons has to be investigated. The challenge lies in whether the production is large enough and whether $\bar{\text{P}}$ANDA will be able to suppress the background sufficiently enough to allow the study. The production mechanism of D mesons from $p\bar{p}$ collisions (figure 5.1) is unknown, as discussed in section 2.3. Depending on the degrees of freedom that play a role in the production of D-meson pairs, different cross sections are predicted. Figure 5.1 illustrates a possible production mechanism.

The decay of the D mesons to a charged $K\pi$ pair was selected which eases the reconstruction compared to other decays. In particular, the absence of neutral final-state particles optimises the mass resolution and the low multiplicity of tracks keeps the efficiency relatively high. In addition, the branching ratio of this specific decay is relatively large ($3.87 \pm 0.05\%$) [31].

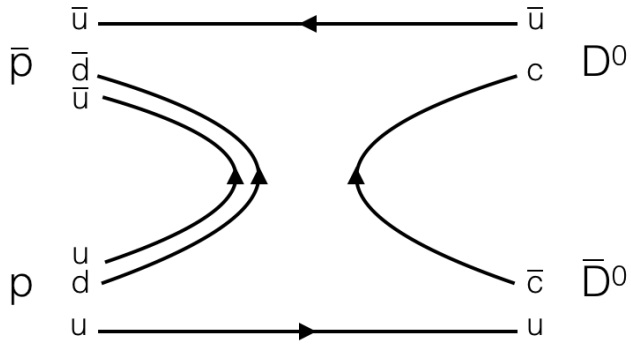

Figure 5.1: Quark-line diagram of the production of a $D^0\bar{D}^0$ meson pair from $p\bar{p}$ collisions.

The following list summarizes the parameters and assumptions used for the MC production of signal and background events, their propagation through the $\bar{\text{P}}$ANDA detector, and the momentum reconstruction and Particle IDentification (PID). The revision number of PandaRoot used was 30163.

- The beam momentum is set at 6.5 GeV/c, i.e. 40 MeV/c above the production threshold. The reason for this choice was to be as close to the production threshold as possible in order to achieve the best absolute mass and momentum resolution. Moreover as seen in figure 2.8, at 6.5 GeV/c the cross section has a maximum value, if the $\psi(3770)$ resonance is not taken into account. If we go closer to the production threshold, the cross section will drop drastically.

- The corresponding masses of all particles participating in the reaction are: $M_{D^0,\bar{D}^0} = 1.8648$ GeV/c^2, $M_{K^-,K^+} = 0.49368$ GeV/c^2, $M_{\pi^-,\pi^+} = 0.13957$ GeV/c^2, $M_{p,\bar{p}} = 0.93827$ GeV/c^2 [31].
- The $\bar{\text{P}}$ANDA detector components have been implemented in PandaRoot [81] which uses GEANT4 [87] to model the interaction of the final-state particles with matter.
- For the identification of the final-state particles, information from the STT, MVD, EMC, DIRC, RICH, TOF is used. The final probabilty is calculated as follows. The multiplication of probabilities of each detector is first calculated. This number is normalised and used as classifier. Then, a cut (> 0.1) is placed on it.
- For the presentation of the analysis steps and the cuts applied, 35000 signal (EvtGen) and 10^7 background (DPM) events were used. For the EvtGen, we assume a uniform S-wave phase-space distribution.

5.2 Event generation

The EvtGen generator (introduced in section 3.3.2) in PandaRoot is used for the simulation of the physics channel studied in this chapter. The production of the D mesons is performed by using a decay file where the desired decay to a $K\pi$ pair is also included. Figure 5.2 shows the complete reaction chain that has been studied in this thesis. Figure 5.3 shows the analysis strategy of the reaction studied. It includes both methods of reconstruction (inclusive and exclusive).

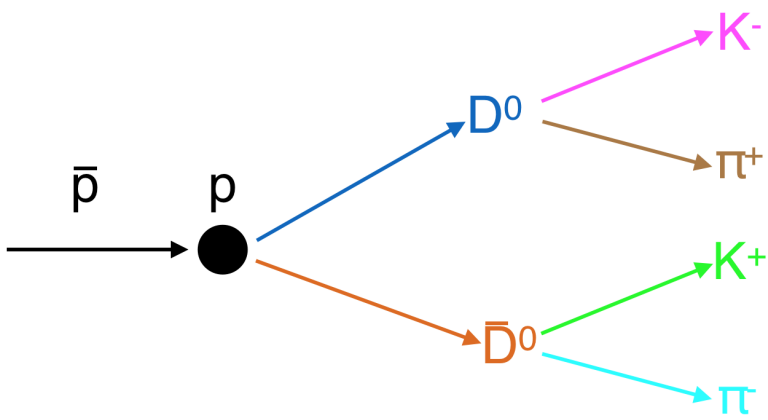

Figure 5.2: Sketch of the complete reaction chain studied.

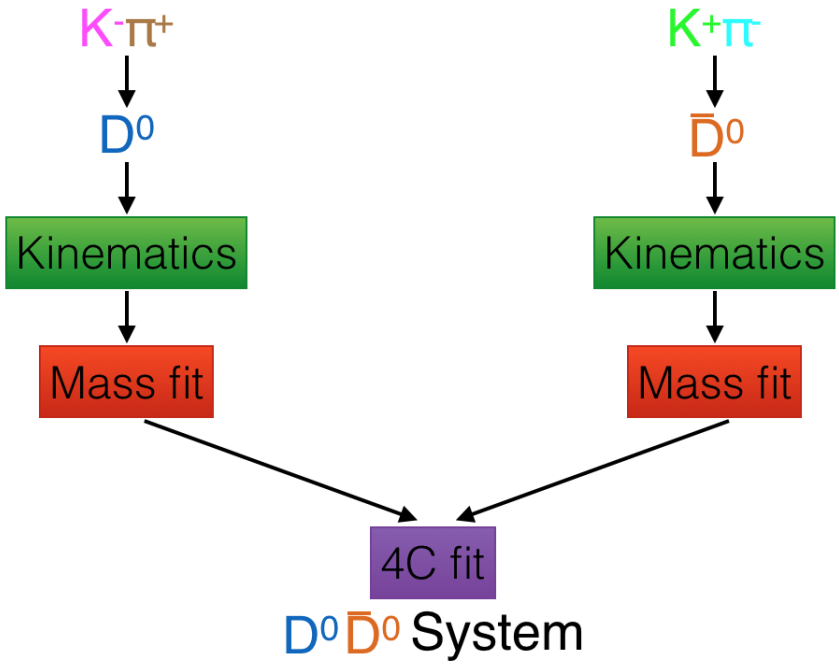

Figure 5.3: Sketch of the analysis strategy used during the reconstruction of the $D^0\bar{D}^0$ mesons.

Figures 5.4 - 5.9 present various distributions of generated events related to the D^0 branch. The corresponding histograms for the $\bar{D}^0$ are similar. The pions reach a higher polar angles than the kaons, due to their lower mass. The angular range of the pions extends to 180°. The D^0 meson on the other hand, reaches very small angles, up to 4°. The transversal momentum of the D^0 meson is much lower than the longitudinal momentum due to the large Lorentz boost of the interaction in the longitudinal (beam) direction (see figure 5.9). The longitudinal momentum distribution of the D mesons is uniform while the transversal momentum distribution has a maximum value of 210 MeV/c, which is defined by the excess energy of the phase-space of the interaction.

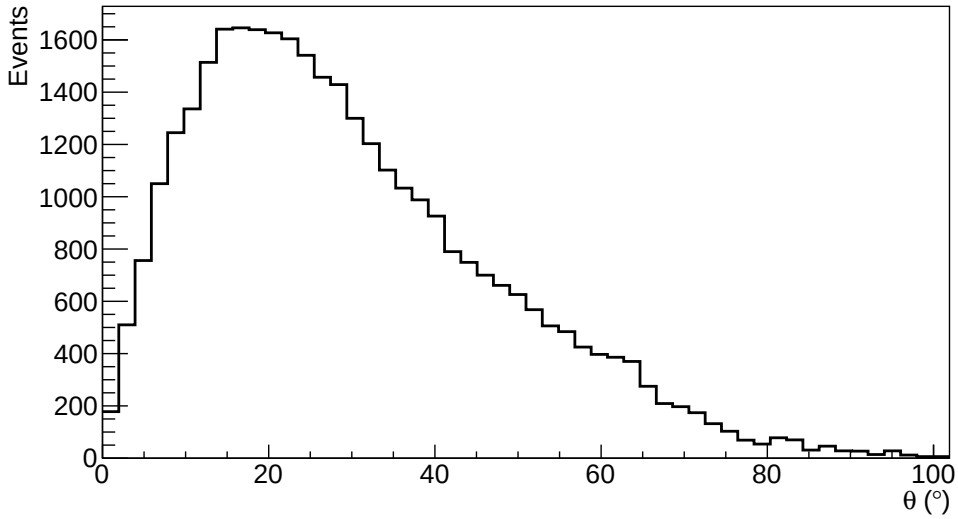

Figure 5.4: The polar distribution for the generated K^-.

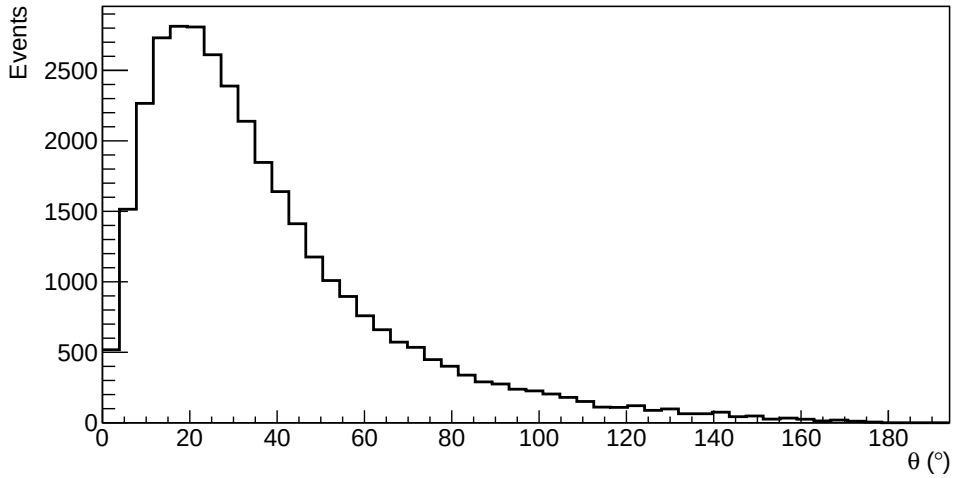

Figure 5.5: The polar distribution for the generated π^+.

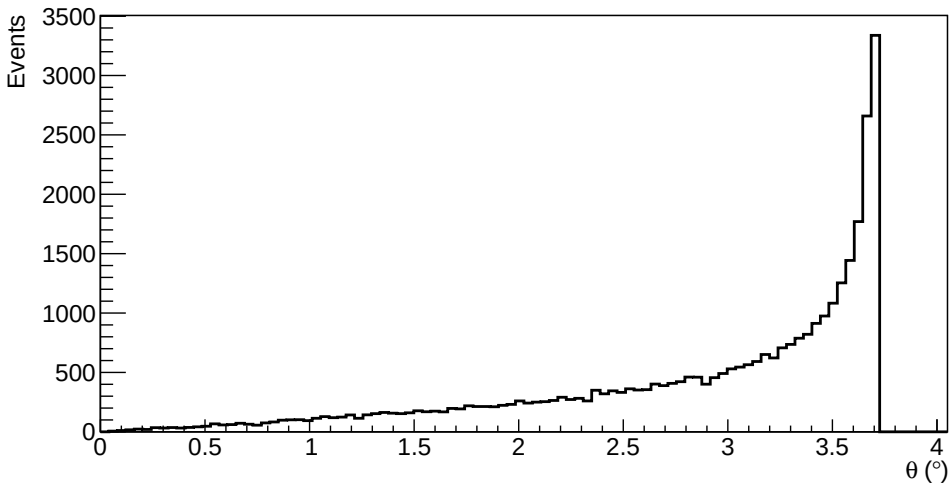

Figure 5.6: The polar distribution for the generated D^0.

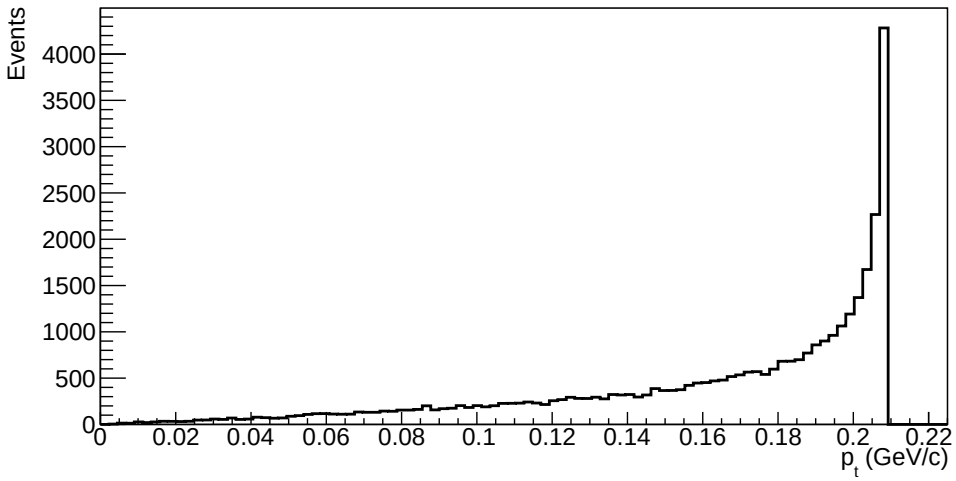

Figure 5.7: The transversal momentum distribution for the generated D^0.

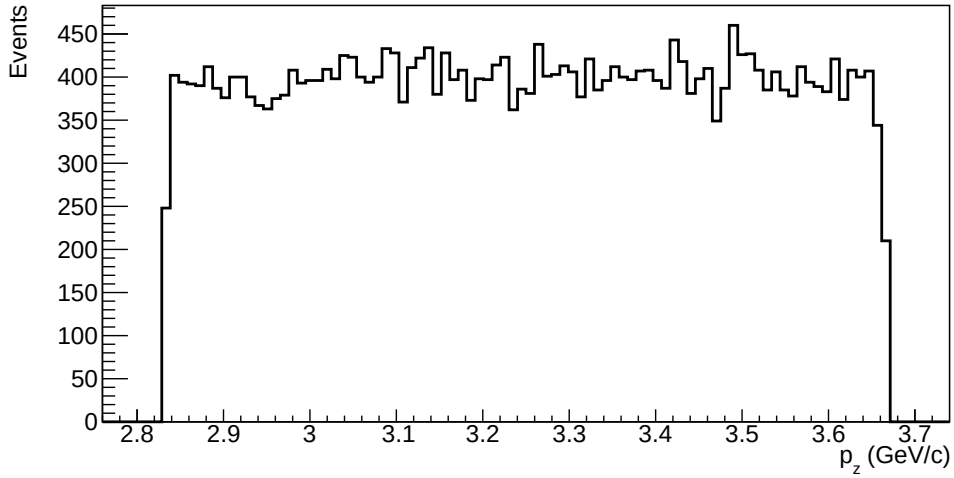

Figure 5.8: The longitudinal momentum distribution for the generated D^0.

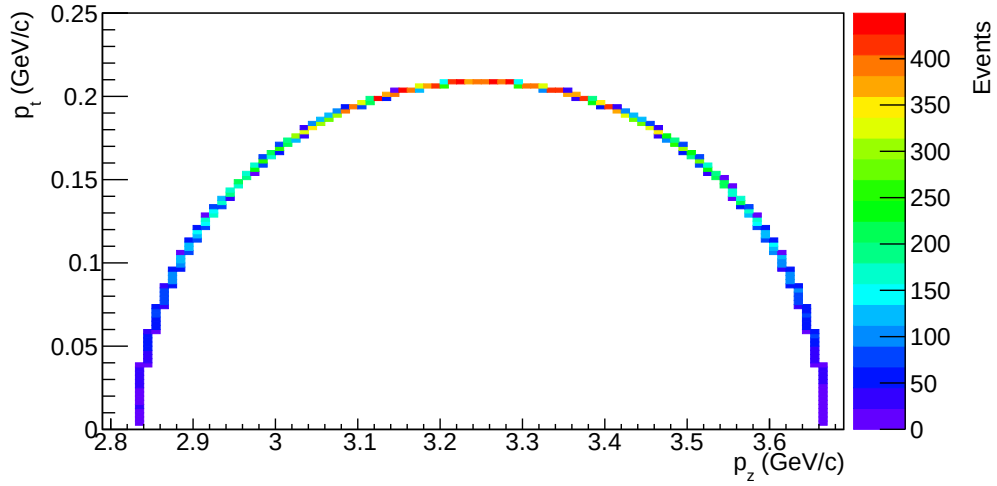

Figure 5.9: Transversal versus longitudinal momentum distribution for the generated D^0.

5.3 Particle identification

For the reconstruction of the events, the identification of the final-state particles is important in order to minimise the combinatorial background. As mentioned in section 5.1, several detectors were used for the PID. Since each of the D mesons decay into two charged particles, the track reconstruction and the PID are the two crucial elements in our analysis. For this reason, an investigation of the hits in two of the main tracking detectors, the STT and the MVD, will be performed. Moreover, a connection with the work presented in chapter 4 will be sought for. Figure 5.10 shows the STT hits for each of the K^- and π^+ tracks, while figure 5.11 shows the MVD hits for the same tracks. The number of hits in both tracking detectors, is the one expected for this momentum range and particle types [68], [71]. The low number of hits corresponds to low momentum particles. The hit multiplicities for the K^+ and π^- are very similar.

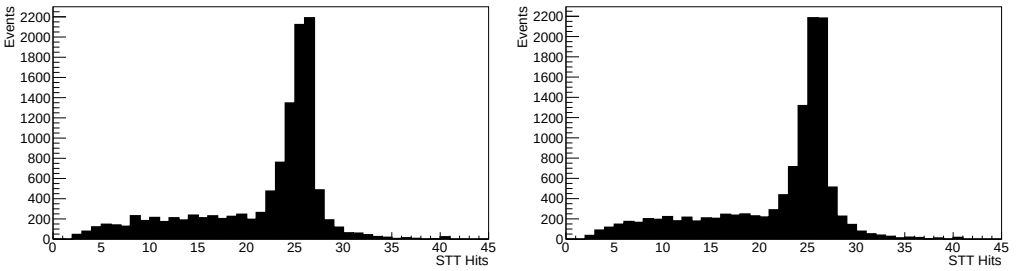

(a) (b)

Figure 5.10: (a) Hit multiplicity distribution in the STT detector for the K^- (a) and the π^+ (b).

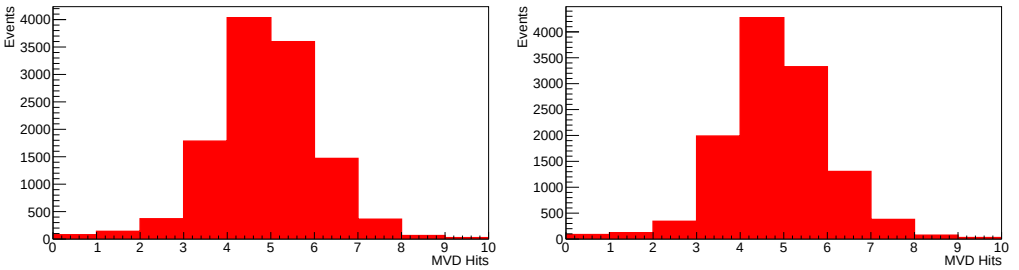

(a) (b)

Figure 5.11: (a) Hit multiplicity distribution in the MVD detector for the K^- (a) and the π^+ (b).

An investigation of the contribution of each of the PID detectors was performed in order to check which detectors play the most important role in our channel. For this reason, multiplicity spectra for the K^- for different combinations of PID detectors are presented in figure 5.12. The first combination is when the STT detector does not contribute to the PID. The second is when the DIRC detector does not contribute to the PID. The last one is when the PID information comes only from the STT detector. The situation in which all PID detectors contribute is also shown. One can see that for our channel, the STT has a small contribution in the PID, since most of the final-state particles have high momenta. On the other hand, the DIRC detector is quite important, since it performs the PID in the high momentum region. This is clearly seen in figure 5.12, where the efficiency loss is quite high. Multiplicities of zero candidates imply that the reconstruction did not succeed or K^- tracks were assigned as π^- tracks leading to inefficiencies. The cases in which the number of reconstructed K^- mesons is larger than one correspond to π^- tracks wrongly assigned as K^-. In a higher-multiplicity decay of the D mesons, in which there will be particles with very low momenta, the STT will play an important role. This can be seen in figure 5.13, where the separation between the K^- and the π^- for momentum less than 0.8 GeV/c^2 is quite clear.

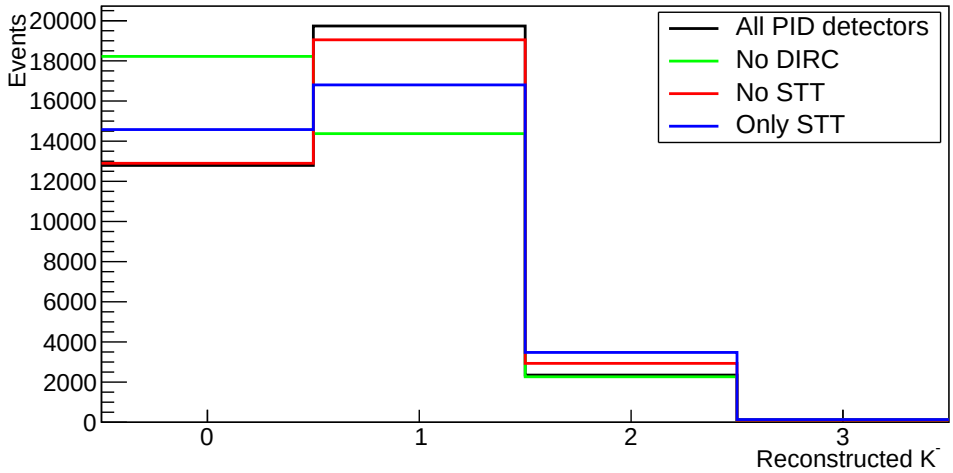

Figure 5.12: Multiplicity spectrum for the reconstructed K^- for different PID scenarios.

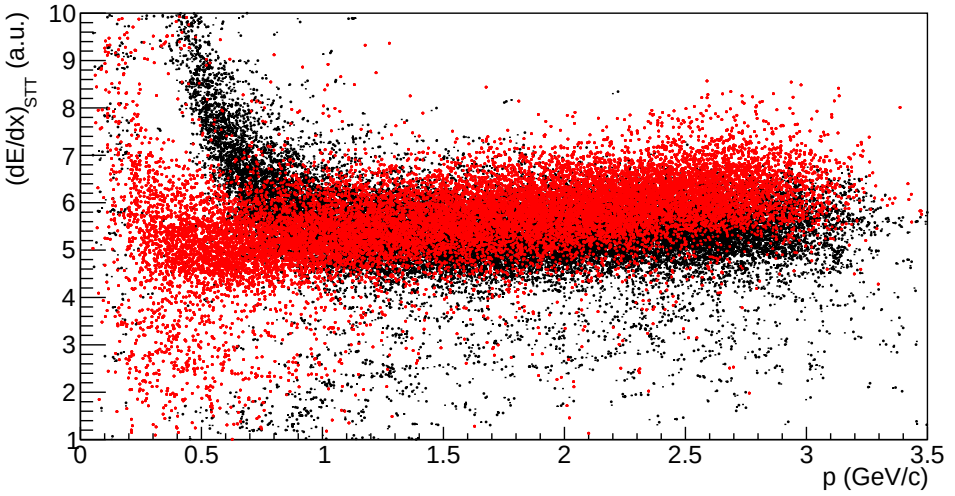

Figure 5.13: dE/dx from the STT versus momentum for the decay products $K^-\pi^+$ of the D^0 meson. Black dots indicate the K^- and red dots the π^+.

5.4 Event reconstruction

This section presents the reconstruction of the events for which the PID information of all available detectors has been used. First, the reconstruction of the final-state particles takes place, followed by the reconstruction of the D mesons. In figures 5.14, 5.15, 5.16, the multiplicity of reconstructed K^+, K^-, π^+, π^-, D^0 and $\bar{D}^0$ is presented. It can be seen that for all final-state particles there are many events that were not properly reconstructed. A systematic difference between the positive and the negative particles is observed. This affects the number of generated D^0 and $\bar{D}^0$ mesons which is seen in figure 5.16. There are also some events with more than one K^- or π^+, and this leads to the reconstruction of more than one D^0 per event. This behaviour effects the detection efficiency for the specific decay chain.

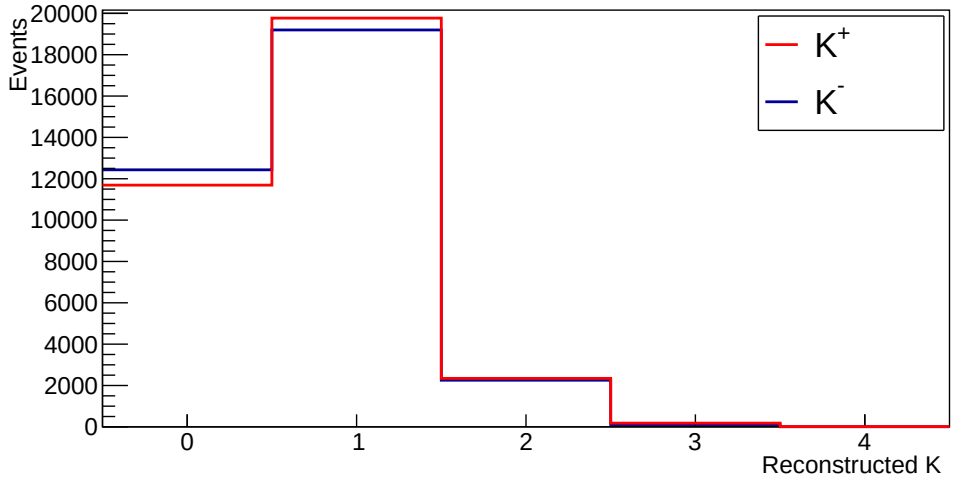

Figure 5.14: Multiplicity spectrum for the reconstructed K^+ and K^-.

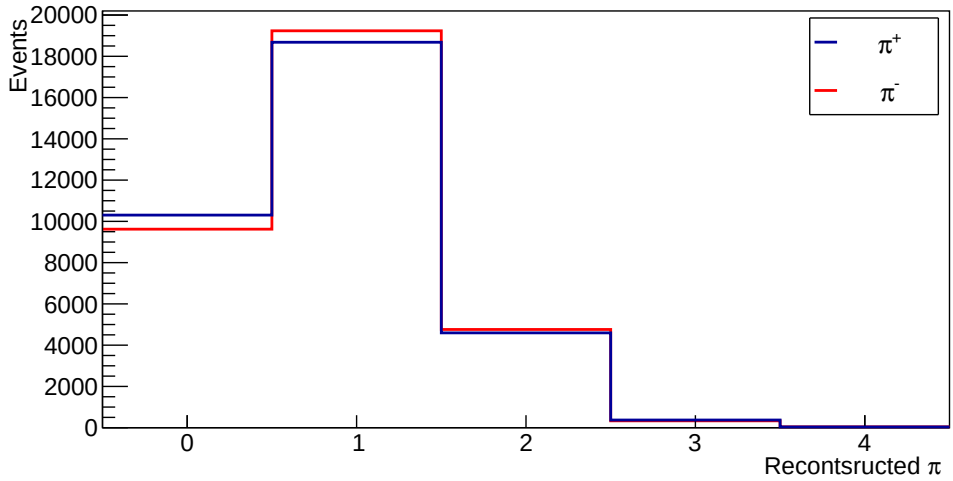

Figure 5.15: Multiplicity spectrum for the reconstructed π^+ and π^-.

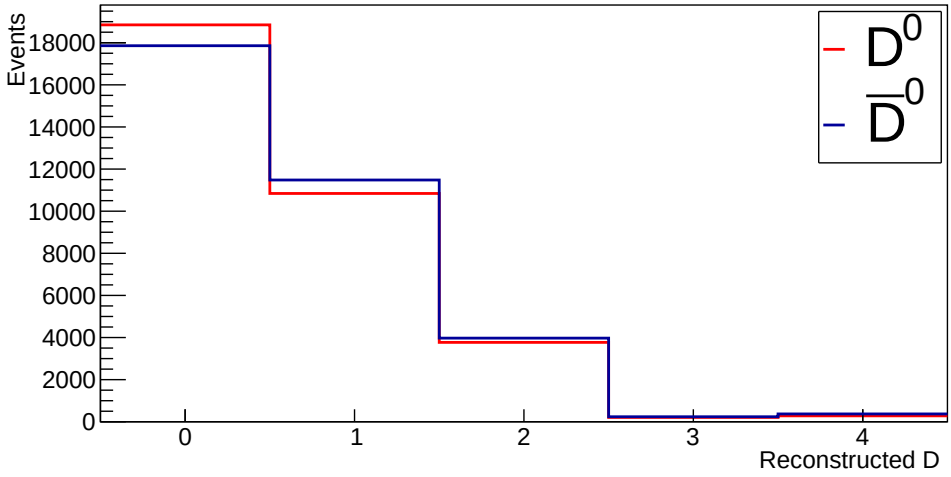

Figure 5.16: Multiplicity spectrum for the reconstructed D^0 and $\bar{D}^0$.

In order to compare the momentum and angular distributions of the reconstructed particles participating in the decay with the corresponding distributions coming from the generated particles, we concentrate on the distributions corresponding to an inclusive reconstruction of only one of the D-meson decays. This implies that two charged tracks, namely that of the kaon and pion candidates, have been detected. We note that the distributions from the exclusive analysis, in which all final-state particles are detected, exhibit similar features. Moreover, only events which are MC-truth matched are presented (i.e. reconstructed events which have a true MC counterpart). This means that only events that have been matched with the generated ones are used. For example, we are not considering events that have zero D^0 candidates (see figure 5.16) since these are not MC-truth matched.

Figure 5.17 shows the angular distributions of the reconstructed K^- and π^+. It can be seen that the π^+ reaches higher angles than the K^-. The same argument holds for the daughter particles of the $\bar{D}^0$ meson. Their angular distributions are similar to the ones shown in figure 5.17. It can be seen that the daughter particles of the reconstructed mesons reach lower angular range than those of the generated mesons (see figures 5.4 and 5.5). Both daughter particles show a drop at an angle of 10°, which is due to the lack of detection volume in very small angles in the target spectrometer. This will add an extra reduction on the detection efficiency we obtain during the analysis of the events. The momentum and angular distributions of the reconstructed D^0 mesons are shown in figure 5.18. The distributions for the $\bar{D}^0$ are similar. The corresponding distributions coming from the generated particles are identical (see figures 5.6 and 5.9).

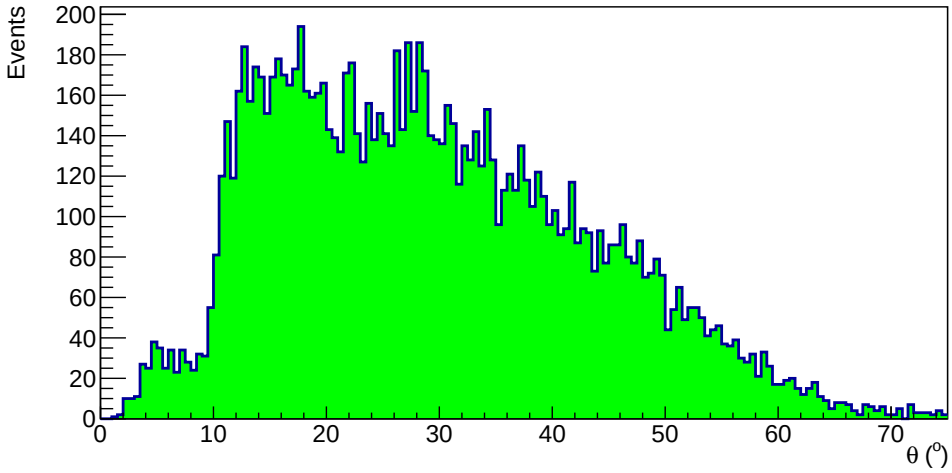

(a)

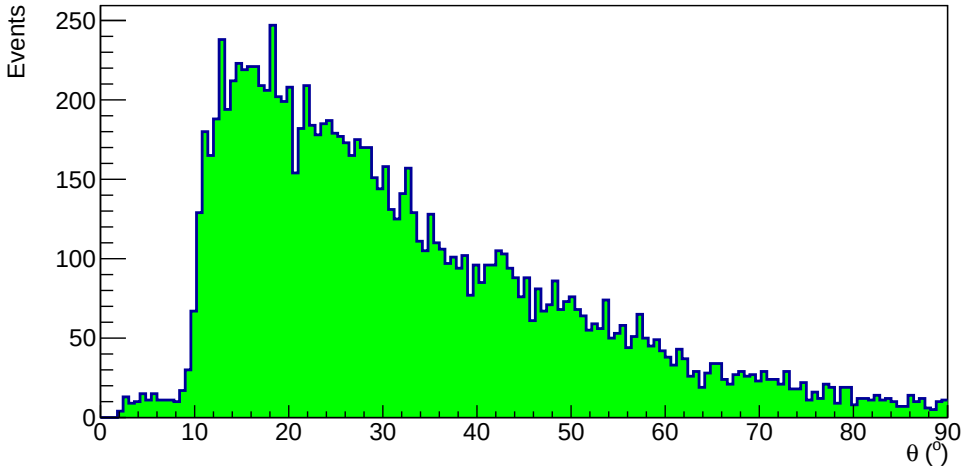

(b)

Figure 5.17: Polar distributions for the K^- (a) and the π^+ (b) of the reconstructed D^0 MC-truth matched candidates.

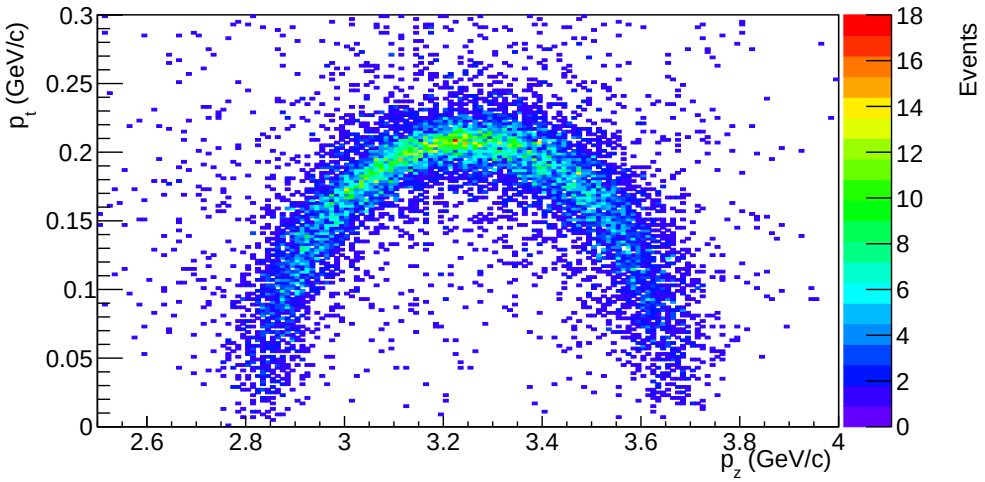

(a)

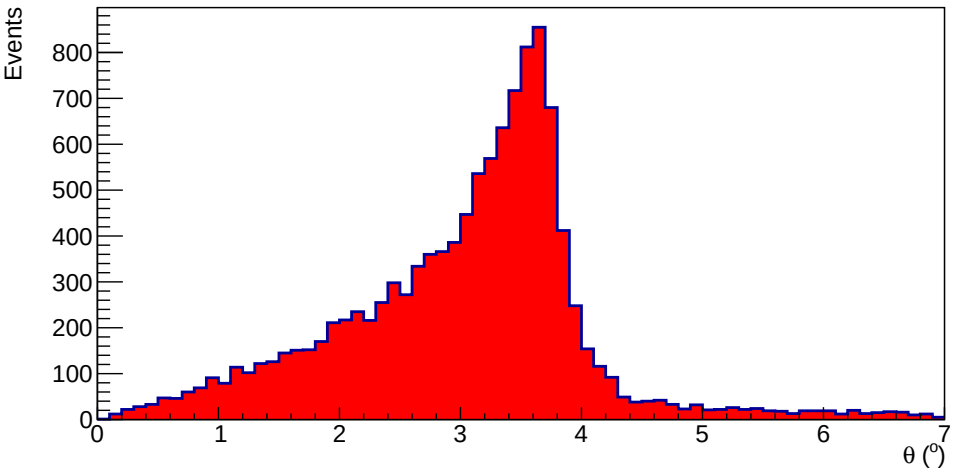

(b)

Figure 5.18: (a) Correlation between the transverse versus the longitudinal momentum of the reconstructed D^0 MC-truth matched candidates. (b) The polar distribution of the reconstructed D^0 MC-truth candidates.

Figure 5.19 shows the momentum distribution of the reconstructed D^0 meson. Longitudinally, a uniform momentum distribution is observed, while for the transverse momentum a peak is seen at about 210 MeV/c. The distributions are very similar with those shown in figures 5.7 and 5.8.

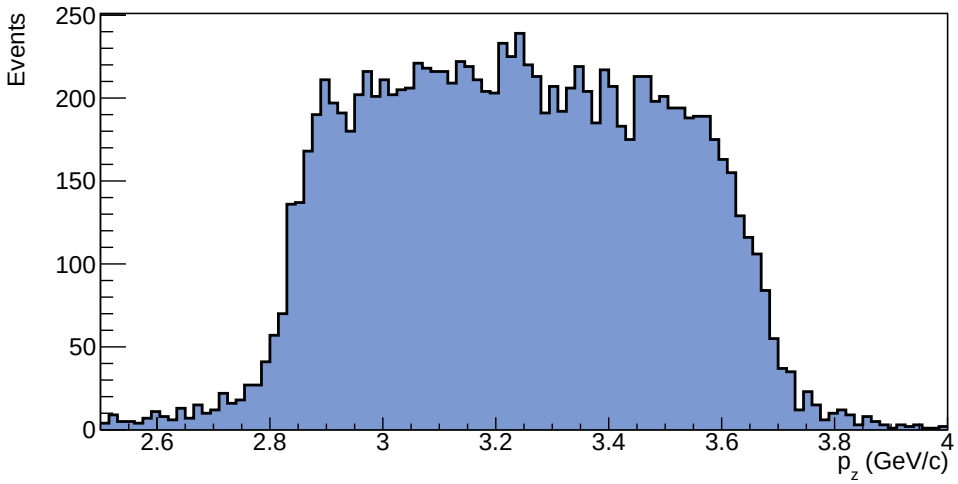

(a)

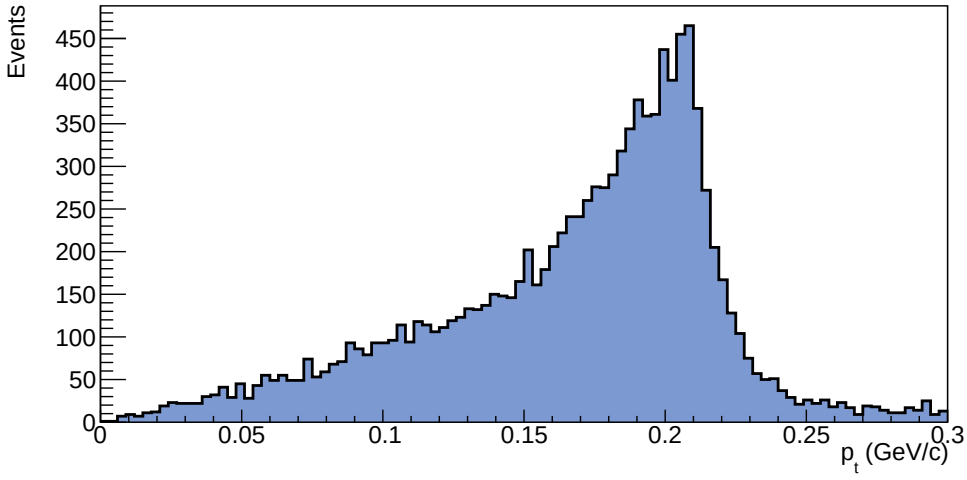

(b)

Figure 5.19: (a) Longitudinal momentum distribution of the reconstructed D_0 MC-truth matched candidates. (b) Transversal momentum distribution of the reconstructed D_0 MC-truth matched candidates.

In order to give an impression of the effect of the MC-truth match filter, in figure 5.20 the longitudinal momentum of all the reconstructed D^0 mesons is shown. It can be seen that the distribution is different with the MC-truth matched result (figure 5.19). Moreover, the distribution starts to look more different than the corresponding one coming from the generated D^0 mesons (figure 5.8).

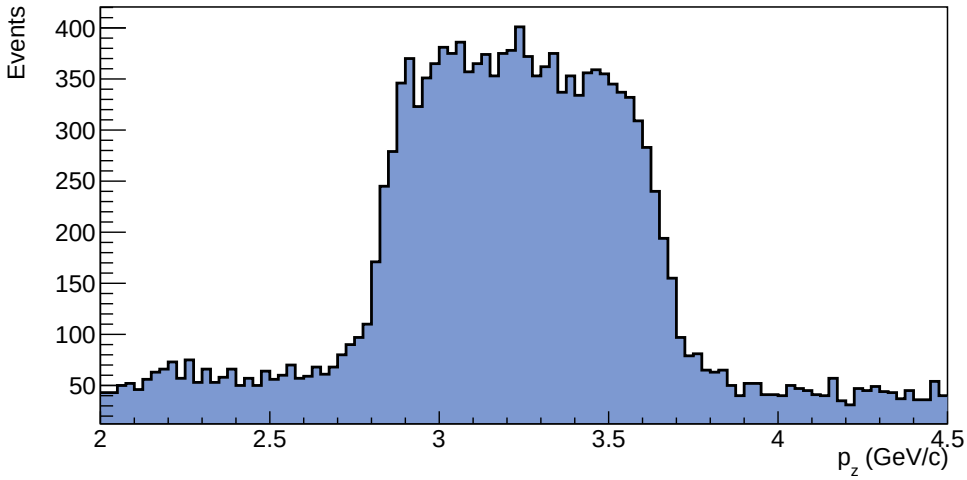

Figure 5.20: The longitudinal momentum distribution for all reconstructed D^0.

The D mesons have a decay length of 120 μm. In $\bar{\text{P}}$ANDA, it will be quite difficult to determine the $\bar{p}p$ interaction point for each event. This will not allow us to precisely determine the absolute decay length of the D mesons and as a consequence, this information cannot be used for the signal identification. Another option is to use the distance R between the two decay vertices of the D mesons. Figure 5.21 shows the distributions of the longitudinal and transversal distance between the decay vertices of the two D mesons. For the first case, the decay positions are symmetrically arranged in space, while for the second, the separation of the decay vertices is generally less than 100 μm, which is below the spatial resolution of $\bar{\text{P}}$ANDA. The conclusion is that we will not be able to use any of the information coming from the position of the D mesons to separate the signal from the background events.

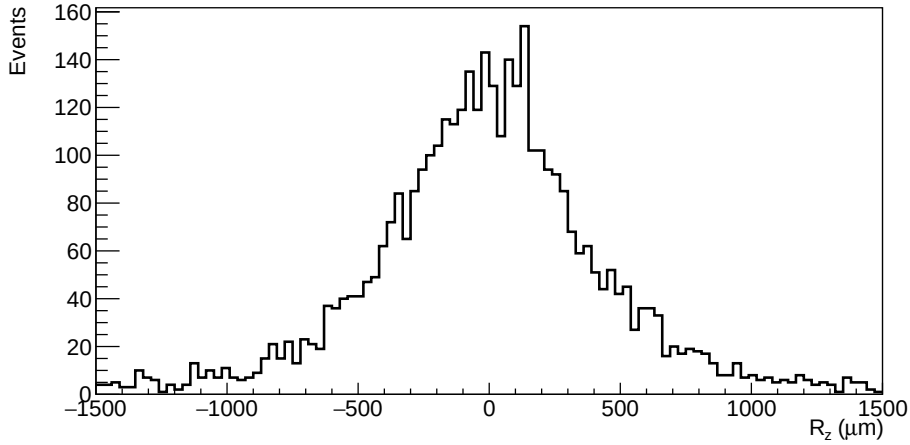

(a)

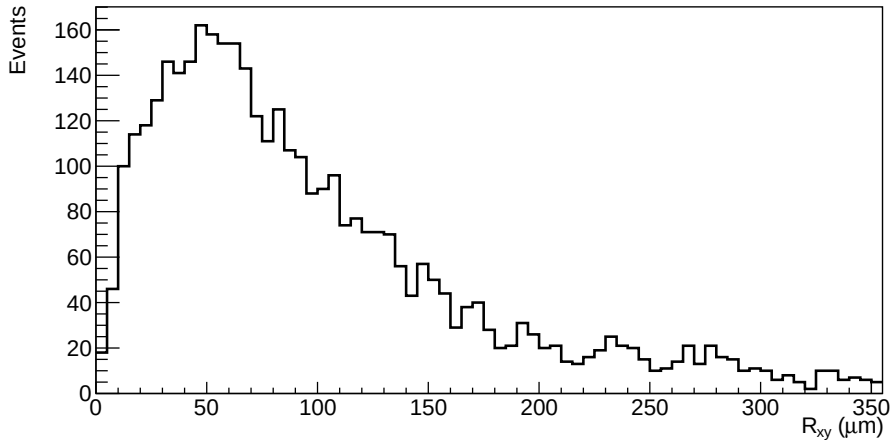

(b)

Figure 5.21: Longitudinal (a) and transversal (b) distance of the reconstructed decay vertices between the D_0 and $\bar{D}^0$ MC-truth matched candidates. The position of the vertices is calculated using a vertex fit.

5.5 Event analysis

In this section, the detection of the D mesons is studied extensively. As mentioned before, the kaons and pions are combined together to form the composite D mesons. The analysis uses both inclusive (single D meson) and exclusive (D-meson pair) reconstruction of the final state. The parameters and assumptions used are summarized in section 5.1. For the event analysis, the Rho package available in PandaRoot is used. Figure 5.3 shows the two different ways of reconstruction. During the analysis, two fits are used to constrain the events to those coming from the D mesons. Both of these fits are members of the PndKinFitter class of PandaRoot [81, 83]. The first one is called "mass-constraint fit", or just "mass fit", and it is used to change the momenta of the pion and kaon that originate from the decay of the D^0 meson in such a way that its invariant mass matches the nominal mass of the D^0 meson ($M_{D^0,\bar{D}^0} = 1.8648$ GeV/c^2). In other words, it constrains the invariant mass of the $K\pi$ system to match the D^0 nominal mass [104]. The second fit used is called "4-constraint fit", or "4C fit", and it can be only used for the reconstruction of the exclusive events. This is due to the fact that this fit, modifies the momenta of all the final-state particles in such a way that the total energy and momenta are precisely conserved [104].

During the analysis steps presented later in this chapter, both results from the signal channel and the background are shown to make the comparison and justify the cuts applied during the event selection. The final goal of this analysis is to test the feasibility of $\bar{\text{P}}$ANDA to detect the D-meson events and separate them from the background events. To evaluate this, we use the following Figure-Of-Merit (FOM):

$$FOM = \frac{S}{\sqrt{S+B}}, \tag{5.1}$$

where S represents the number of signal events that can be obtained from

$$S = L \times t \times CS_s \times BF_s \times E, \tag{5.2}$$

and B is the number of background events, calculated by

$$B = \frac{L \times t \times CS_b}{Sup}. \tag{5.3}$$

In the equations 5.2 and 5.3, L is the luminosity (2×10^{30} to 2×10^{32} cm^{-2} s^{-1}), t is the time of the data taking, CS_s is the signal cross section, BF_s is the branching fraction of the decay we use ($2 \times 3.87\%$ for the inclusive and $3.87\% \times 3.87\%$ for the exclusive reconstruction), E is the efficiency which includes the detector acceptance and reconstruction efficiency, CS_b is the background cross section (50 mb) [14] and Sup is the suppression factor we obtain for the background after our analysis. The desired value for the FOM is to reach a significance of 5σ in order to be able to make a firm statement about the measurement of the production of the D meson pairs.

For the reconstruction of one of the D mesons, one kaon and one pion reconstruction is needed. On the other hand, two pairs of $K\pi$ are needed for the reconstruction of both D mesons. In this section, the results obtained from both reconstruction methods are presented. For every step of the analysis, all cuts are explained and compared with the background events. The cuts applied are the same for both inclusive and exclusive reconstructions as well as for both signal and background events. At the end of this section, a table containing all the relevant values for resolution and efficiency are presented for both reconstruction methods and for all the different cuts and fits applied.

Kinematic cuts

The first cuts applied are related to the kinematics of our reaction. A cut on the energy and emission angle of the D mesons is applied together with a cut on the center-of-mass energy. The plots presented are for the D^0 meson, but the corresponding histograms for the $\bar{D}^0$ meson are similar. The purpose of the cuts is mainly to reduce the number of the background events mixing with our signal events. Figures 5.22 and 5.23 show the correlation between the energy versus emission angle and the center-of-mass energy of the D^0 meson for the signal and background events, respectively. It can be seen that a huge number of background events is outside the cut ($> 80\%$), which means a large suppression factor for the background. On the other hand, one has to be careful when selecting the values of several cuts, since one would aim for as large a value of efficiency as possible for the signal events. The optimization of the FOM is the main criterion when selecting the cuts.

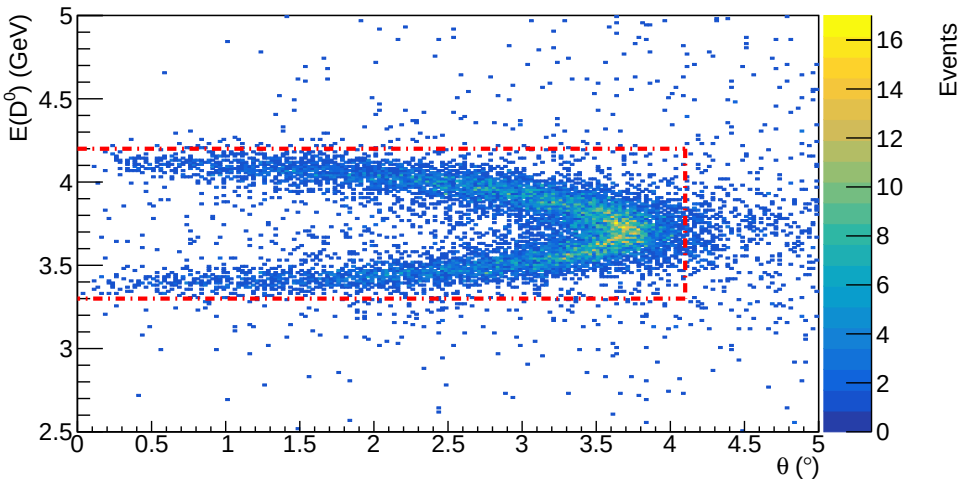

(a)

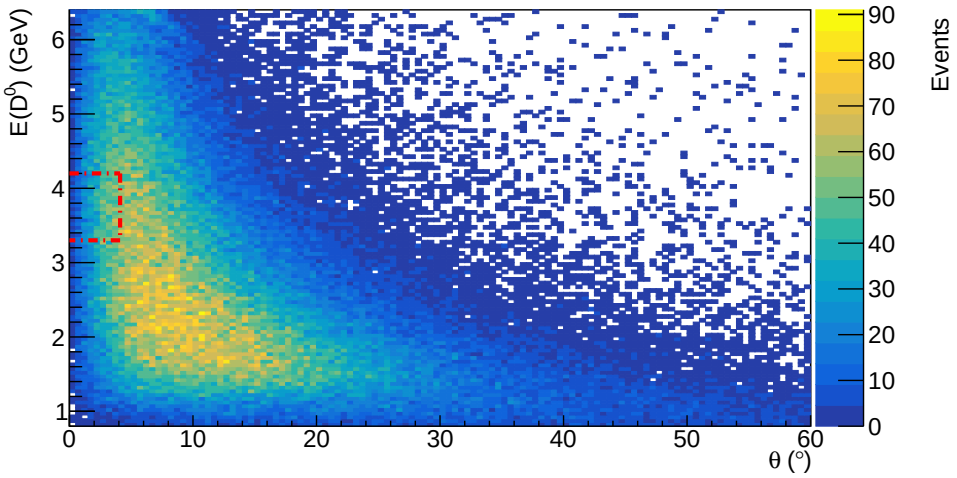

(b)

Figure 5.22: (a) Energy versus production angle of the D^0 meson candidates for the signal events. (b) Energy versus production angle for the D^0 meson for the background events. In both histograms the red line indicates the cuts applied for the analysis.

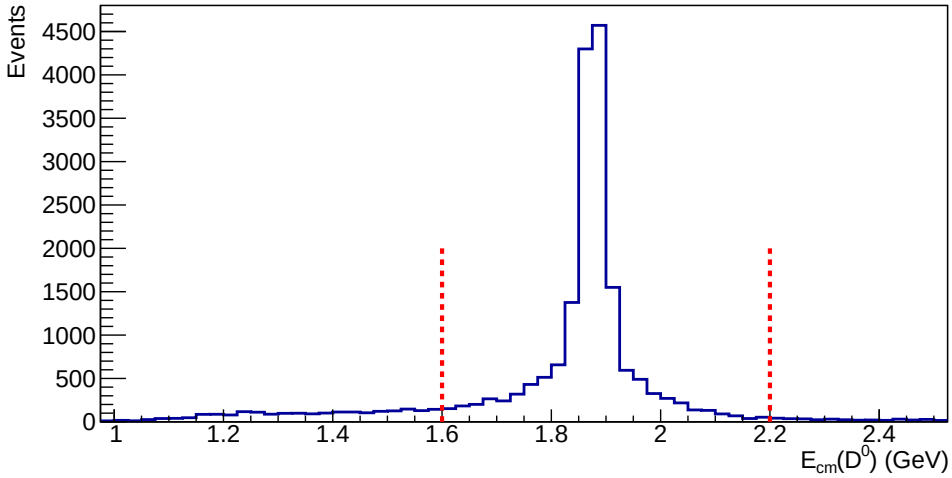

(a)

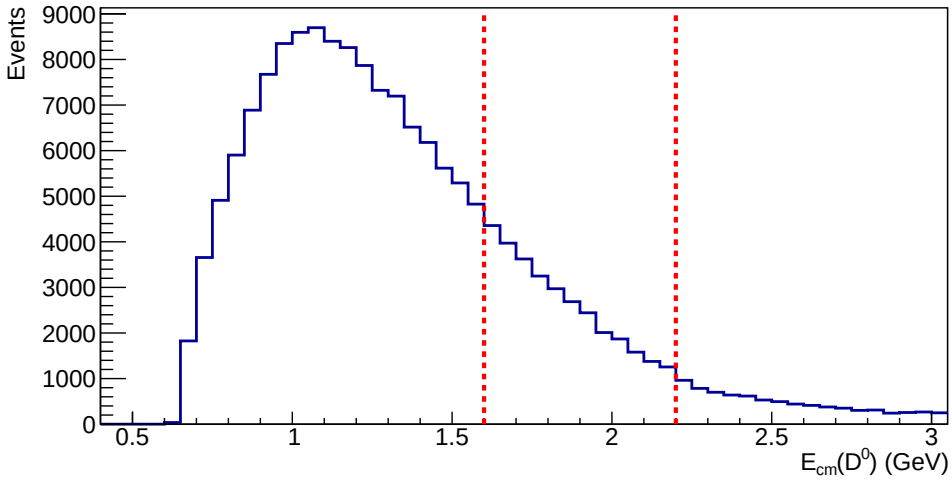

(b)

Figure 5.23: (a) Center-of-mass energy of the D^0 meson candidates for the signal events. (b) Center-of-mass energy of the D^0 meson candidates for the background events. In both plots the red lines indicate the cut values applied for the analysis.

Mass constraint and 4C fit

The mass-constraint fit can be applied for both the inclusive and the exclusive analysis, while the 4C fit can be applied only in the exclusive analysis. A cut on the probability function in both fits is applied. This was optimized for maximum signal to background ratio. Figure 5.24 shows the probability distributions, i.e. the integral of the χ^2, of both fits for the signal and background events. The reason why we observe an increase in the probability distribution at values close to one is that the error matrix that represents the detector resolutions is not perfectly optimised in the software. In both cases, we exclude from the analysis events with a probability value below the cut of 0.1.

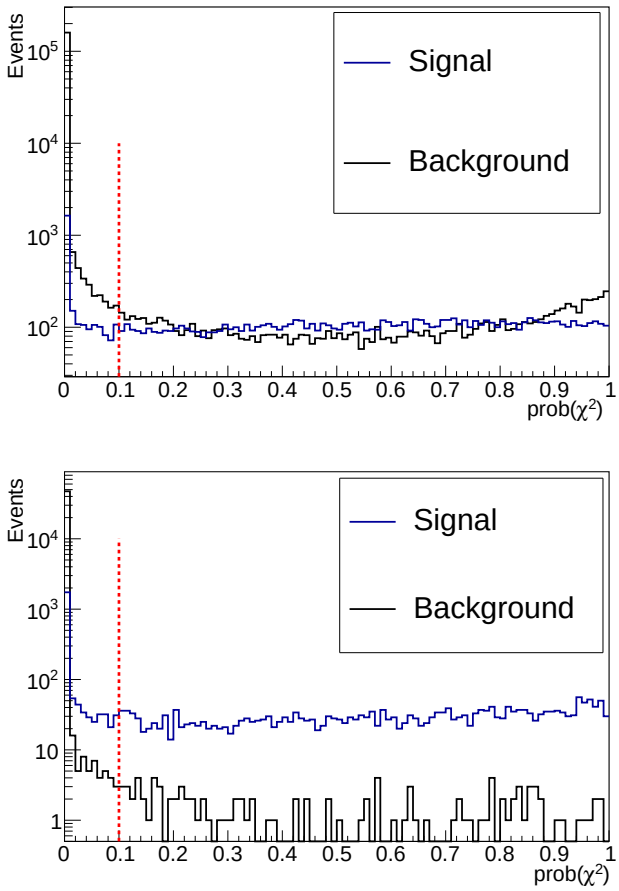

Figure 5.24: Upper panel: Probability distribution of the mass constraint fit applied to the D^0 meson. The red dashed line indicates the cut applied. Lower panel: Same as upper panel but for the 4C fit.

Results after cuts

The impact of the previous discussed cuts on the invariant-mass distribution of the two D mesons is presented here. Figure 5.25 shows the recoil invariant-mass distributions for the signal and background events in the case of the inclusive reconstruction, while figure 5.26 presents the same quantity for the exclusive reconstruction. For both cases, the recoil mass of the $K^-\pi^+$ pair is shown.

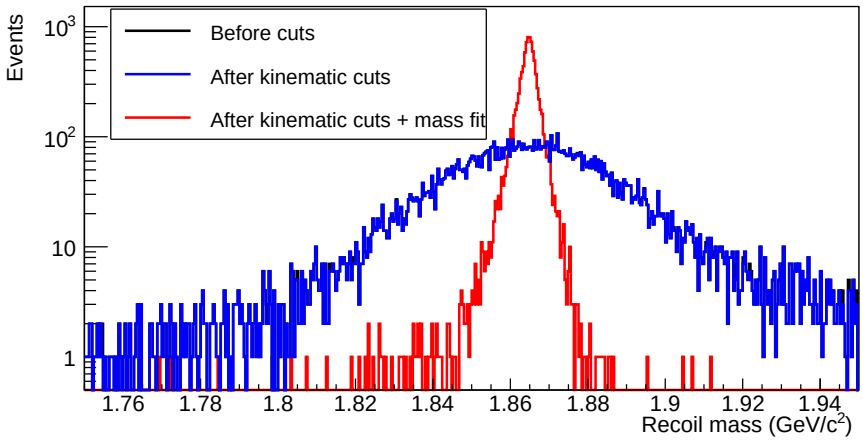

(a)

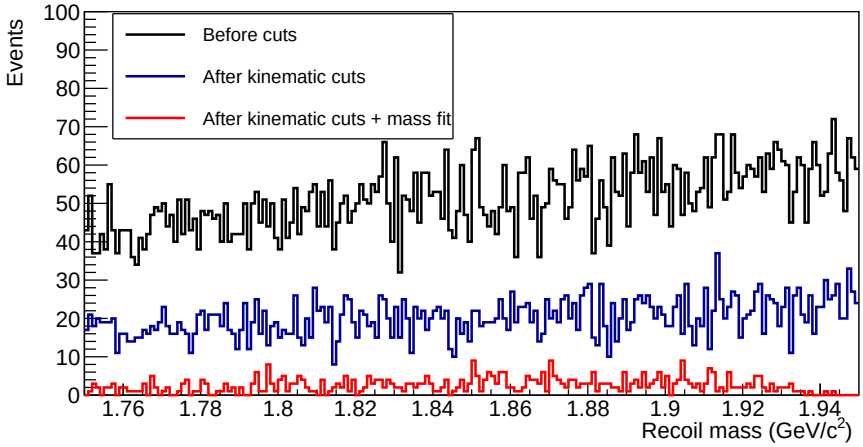

(b)

Figure 5.25: Reconstructed recoil mass distribution for the $K^-\pi^+$ pair from the signal (a) and background (b) events in the inclusive reconstruction after each stage of the event "filtering".

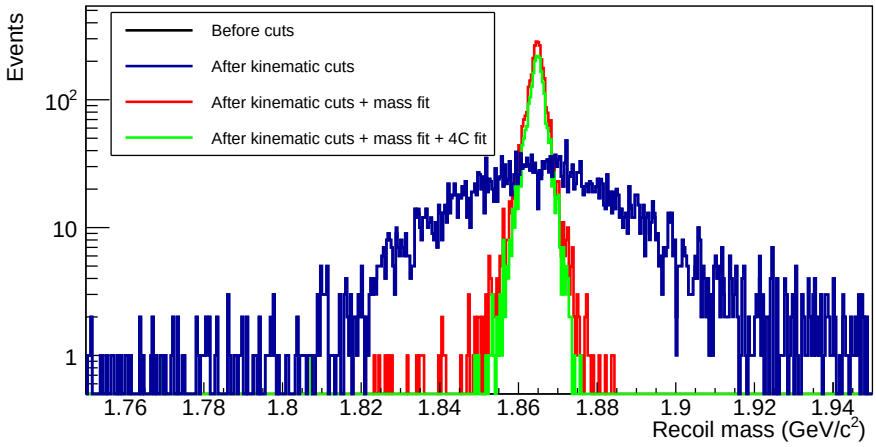

(a)

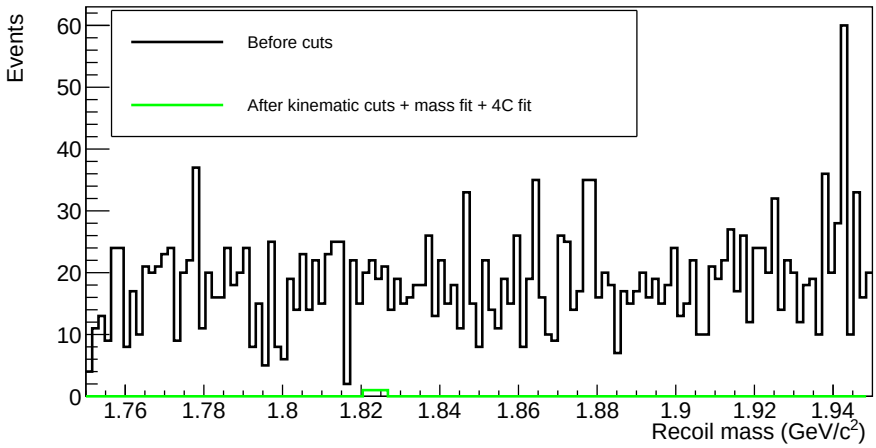

(b)

Figure 5.26: Same as figure 5.25 but for the exclusive reconstruction.

As seen from figures 5.25 and 5.26, the number of background events is strongly reduced after applying the cuts. The combination of the kinematic cuts with the "mass fit" scales down the number of background events by a factor of 10, while the addition of the "4C fit" in the case of the exclusive reconstruction leaves very few background events in the mass range of the D mesons. For a mass range of $\pm 5\sigma$ of the mass resolution obtained, the number of background events left after all cuts for the inclusive analysis is 78 while for the exclusive analysis no event survives the cuts. This means that a background suppression factor of 10^5 for the inclusive and at least 10^7 for the exclusive analysis is reached, respectively.

Table 5.1 contains the information about the mass and momentum resolutions, as well as the efficiencies of the reconstruction procedures.

	D^0			$\bar{D}^0$		
	N %	σ_M MeV/c^2	σ_p MeV/c	N %	σ_M MeV/c^2	σ_p MeV/c
Inclusive						
Before cuts	29.5	21.1	50.5	29.6	20.9	50.4
Kinem. cuts	29.3	20.6	50.1	29.3	20.6	50.1
Kinem. cuts + mass fit	26.8	2.1	14.8	26.9	2.2	14.9
Exclusive						
Kinem. cuts + mass fit + 4C fit	7.1	1.8	12.7	7.2	1.9	12.8

Table 5.1: Overview of the reconstruction efficiencies and mass and momentum resolutions for the D^0 and $\bar{D}^0$ mesons obtained in the different stages of the analysis. The resolutions are calculated using the FWHM divided by 2.355.

In order to obtain the sensitivity for the signal cross section for which we can reach a 5σ statistical significance for the FOM, we consider a 30-day measurement, the whole range of the foreseen luminosity (2×10^{30} to 2×10^{32} cm^{-2} s^{-1}), a branching fraction of $2 \times 3.87\%$ for the inclusive and $3.87\% \times 3.87\%$ for the exclusive analysis, reconstruction efficiencies from table 5.1, a background cross section of 50 mb and finally the background suppression factors obtained earlier (10^5 and 10^7). Figure 5.27 shows the result obtained for the FOM. It can be seen that in the case of the inclusive analysis, the minimum signal cross section we would be able to observe with 5σ significance with the luminosity available at the "phase-1" of $\bar{\text{P}}$ANDA is 25 nb. This value agrees with the values calculated from the theoretical predictions shown in section 2.3. For the same value of the signal cross section, much less than 1σ significance is reached for the exclusive analysis. This means that the inclusive reconstruction can be used for the specific decay since it can reach a much lower sensitivity for the signal cross section. It must be noted that the 10^7 suppresion factor for the exclusive analysis is an upper limit. If we assume that the background is flat, the suppresion factor can be normalised. The obtained result would be then 10^8. Even with this number, the inclusive analysis still reaches lower sensitivity for the signal cross section.

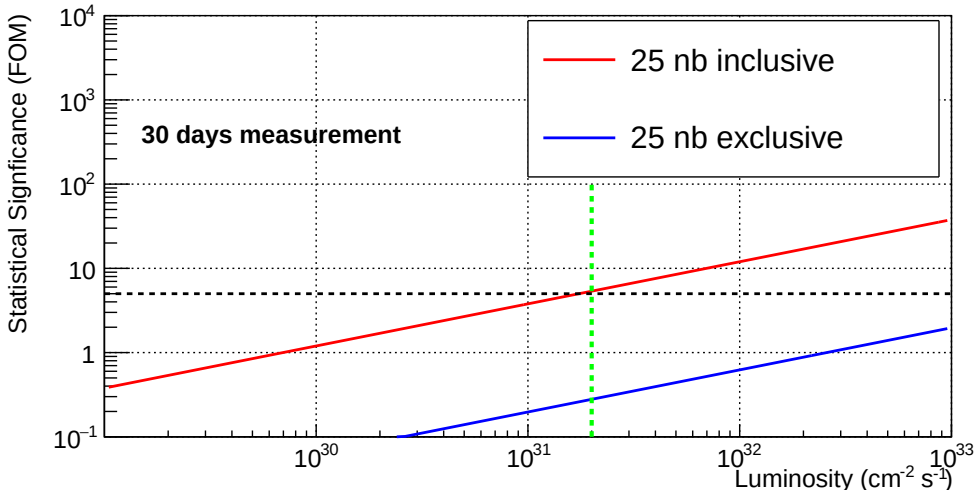

Figure 5.27: Calculation of the *FOM* for the inclusive and exclusive reconstruction method for a 30-day measurement. The horizontal black dashed line indicates the statistical significance and the vertical green dashed line indicates the luminosity value of the "phase-1" of $\bar{\text{P}}$ANDA.

5.6 Summary and discussion

In this chapter, the physics channel $\bar{p}p \rightarrow D^0\overline{D}^0 \rightarrow \pi^+K^-\pi^-K^+$ was studied extensively using MC simulations. The goal of the work was to investigate the feasibility to study open-charm mesons with $\bar{\text{P}}$ANDA. In addition to this, the detector performance concerning the mass, energy and momentum resolution was also investigated and presented. The role of the STT, one of the main tracking detectors of $\bar{\text{P}}$ANDA and the contribution to the PID via the dE/dx information was studied as well.

In the first part, the event topology was presented. Both D mesons are emitted at small angles, while their daughter particles are produced with high momenta and large-range angular distributions. The pions are emitted at larger angles than the kaons due to their lower mass. The distance between the decay vertices of the two mesons is also studied, where it is seen that for the transversal plane, it is well below the spatial resolution resolving capability of the $\bar{\text{P}}$ANDA detector. Moreover, since the two mesons decay into a pair of charged particles, the hit multiplicity in the STT and MVD was investigated. The number of hits per daughter particle is as expected for the momentum range and the particle type.

The event reconstruction of the signal events was studied in two different ways, inclusively (single D-meson reconstruction) and exclusively (D-pair reconstruction). Together with the signal events, the background events were studied simultaneously. The kinematic cuts applied in both cases, along with the two constraint fits available for use in PandaRoot were described. The final results for the efficiency, the mass and momentum resolution are presented in table 5.1. The feasibility for the open-charm production with $\bar{\text{P}}$ANDA is studied via the Figure-Of-Merit (FOM) where a significance of 5σ is important in order to draw safe conclusions. To achieve a 5σ signal, a cross section minimum of 25 nb is required for the inclusive reconstruction method for the "phase-1" of $\bar{\text{P}}$ANDA, i.e. the HR mode of the HESR. The exclusive reconstruction, even though it reaches higher background suppression, suffers from the low efficiency (7.2% compared to the 26.9% of the inclusive).

The role of the STT in the PID and the event reconstruction was also studied. The contribution of the STT for the channel studied in this work is not significant, since the final-state particles have momenta higher than the region where the STT can efficiently perform PID. It was shown that DIRC is the detector that performs PID best for this channel. In the case of a different D-meson decay, where the final-state multiplicity is higher (e.g. decay to $K_s\pi^+\pi^-$), the STT will play an important role to the PID, since the momenta of these particles will be much lower.

Chapter 6

Conclusions and Outlook

In this thesis, the PID capability of a prototype STT detector for the $\bar{\text{P}}$ANDA experimental facility has been studied together with the investigation of the feasibility for the observation of open-charm mesons via the production and decay channel $\bar{p}\,p \rightarrow D^0\,\overline{D}^0 \rightarrow \pi^+ K^- \pi^- K^+$.

6.1 Test of the particle-identification capability of a prototype STT detector

The tracking and the PID are vital parts in the event reconstruction of $\bar{\text{P}}$ANDA, since in many decays the daughters particles are charged particles. Moreover, due to the presence of a huge background, the detector system should be able to distinguish between the events coming from the physics channel of interest and those coming from the background. Thus, a good track reconstruction and PID is needed. The STT, one of the main tracking detectors of $\bar{\text{P}}$ANDA, will play an important role in these two aspects, since it is located around the interaction point and most of the charged particles will travel through it.

A prototype STT has been built and its performance, regarding the spatial resolution and the PID, was extensively studied. Moreover, the readout performance was tested, in order to gain the information required to decide between the two candidate options for the STT readout currently being considered. The focus was given to test whether the existing candidates can cope with the "phase-1" luminosity of $\bar{\text{P}}$ANDA. One is using an ASIC readout and the other an ADC readout. This work presents the results from the ASIC readout concept. Two beam tests were performed, one using a proton beam and one using a deuteron beam. The main motivation behind this was to examine the separation power

between the different particle types. In both tests, the experimental setup was identical and in each test several beam momenta were considered. During the tests, some problems with the electronics and the mechanical setup of the prototype detector were observed which affected our final results. Some of these problems were solved (for example by changing the FEEs) and others have to be further investigated. The calculation of the spatial resolution is sensitive to the momentum of the particles traveling through the tubes. When reaching the minimum ionizing momentum, there are fewer clusters reaching the wire in the center of the tubes, thus the randomness introduced because there is more uncertainty on the distance of the nearest cluster to the wire for a given track-wire distance will be larger. This leads to a worse resolution. The best spatial resolution obtained is in the order of 170 μm for the 0.75 GeV/c deuteron beam. This value is 10% more than the expected one (150 μm) obtained from the simulations. The value of the spatial resolution reached is considered quite satisfactory, if one takes into account the problems encountered during the beam tests. In many cases, it is common practice to use a probability cut to the final track fitting. In this work no cut was applied, since the idea was to optimize the methods before applying any cuts. As a result, the value obtained for the spatial resolution in this work is not biased due to the cut in the probability value. Moreover, the track reconstruction efficiency during the analysis is always kept above 80% which is important in order to get a good track recognition. The values obtained from the different particle types and momenta are summarized at table 4.1. In order to test the PID capability of the prototype STT, the separation power value S was used and defined in equation 4.4. As shown in sections 4.4 and 4.5, the separation power is 6.3 between protons and deuterons with momentum 0.75 GeV/c. This value is very close to the value obtained from simulations for the 0.375 GeV/c momentum between kaons and protons (for more details see figure 4.34). This shows that the current analysis and methods used are good enough to reach agreement with the results obtained from simulations.

Several modifications and steps can be performed in order to get more accurate and improved results. Garfield simulations on the updated STT setup and the existing readout concept have to be performed in order to be able to compare the new simulation results with those obtained from the beam tests. The existing simulations have been performed with slightly different dimensions (length of the tubes and thickness of the tube wall) but most importantly they were performed with an ADC readout. Moreover, the analysis methods and techniques used can be improved. The focus should be towards the following two aspects. The extraction of the isochrone from the drift time ($r(t)$) based on each individual tube will provide a more accurate isochrone calculation since the method used in this thesis takes into account the whole setup and performs the isochrone

calculation based on all tubes of the STT. As seen in figure 4.23 there are individual tubes which give a spatial resolution of the order of 150 μm. This can be seen as a sign that the calculation of the isochrones for each individual tube could improve our results. In addition, a more detailed investigation of the individual tubes regarding the tube and wire position should improve the spatial resolution that can be reached with the existing setup. Ideally, the presence of an automatic re-alignment procedure of the positions of the tubes and wires would make the analysis more accurate and prevent the results from suffering from mechanical imperfections. Performing tests using cosmic rays will provide useful information and insight about the performance and possible imperfections of the mechanical setup and/or analysis methods. Muons, are minimum ionizing particles, but they leave "clean" tracks to the STT and thus, they are easier to reconstruct. Last but not least, as mentioned in section 4.1, the existing TRB readout will not be sufficient for the High-Luminosity (HL) mode of HESR. An upgraded readout system will be needed. Possible modifications to the current system can be the increase of the TDC time resolution to a value of more than 20 ps, or the decrease of the number of channels per TRB3, which will double the number of hits per second per tube that can be stored in our readout system. However, all the proposed changes have to be benchmarked in hardware, using beam tests and incorporated in software. The optimum has to determined based on its performance, cost and energy consumption.

6.2 Feasibility studies for the observation of open-charm mesons with $\bar{\text{P}}$ANDA

The study of hadron spectroscopy is one of the main physics goals of $\bar{\text{P}}$ANDA. Of particular interest, are the open-charm states. The mass spectrum of these states is quite interesting and mysterious at the same time which raises many questions that need to be answered. Many of the open-charm states that have been experimentally discovered have masses far from the theoretical predictions. Moreover, the mass splitting in the nuclear medium for these states is also of great interest in view of observing signatures of chiral-symmetry breaking. Last but not least, there are many exotic, not yet well understood, states observed above the open-charm threshold (XYZ states). A measurement of the partial decay width of these states into open-charm mesons is important since it provides decisive information that will clarify their nature. To investigate these phenomena, high statistics of open-charm states is needed. Hence, it is important to reconstruct D mesons with high efficiency and resolution. $\bar{\text{P}}$ANDA will add a major contribution in producing and detecting open-charm mesons with its high-precision resonance scans, luminosity, and detector capabilities.

In chapter 5 of this thesis, the investigation of the feasibility for open-charm mesons was presented, and in particular the production of a pair of $D^0\bar{D}^0$ mesons. The selected decay of these two mesons is to a pair of $K\pi$ particles which makes the reconstruction of the decay easier and more reliable. The absence of neutral final-state particles allows for better resolution and the low multiplicity of tracks keeps the efficiency high, since for every additional track a reduction in the efficiency will be observed. The goal of the study is to determine how well $\bar{\text{P}}$ANDA will be able to measure these states in terms of mass and momentum resolution, and at the same time investigate how well these states can be separated from the huge background events coming from the $p\bar{p}$ interaction. For the latter, we use the Figure-Of-Merit (FOM) to evaluate the statistical significance of our measurement. The goal is to study the cross section sensitivity $\bar{\text{P}}$ANDA will be able to reach at the various phases of its operation.

For the feasibility study, we made use of the PandaRoot simulation and analysis framework. The Monte Carlo simulations incorporate the interaction of particles with matter, the electronic response of the detectors, and the track finding, fitting, and particle identification methods that will also be foreseen for the actual experiment. The reconstruction of the decay is performed in two separate ways, inclusively (single D-meson reconstruction) and exclusively (both D-mesons reconstructed). Several cuts and kinematic fits were applied with the aim to optimise the FOM for the channel of interest. To identify the channel of interest, we reconstructed the invariant mass of one of the D mesons. The mass resolution obtained is 2.1 MeV/c^2 for the inclusive and 1.8 MeV/c^2 for the exclusive reconstruction, respectively. The corresponding efficiencies are 26.8% and 7.1%, respectively. The efficiencies are relatively low for just two charged tracks. It has been shown that the main source for this problem is the PID performance of the software (see figure 5.16). This means that an improvement in the PID framework is needed. The beam momentum was chosen to be slightly above the open-charm production threshold at which theoretical calculations predict a saturation of the production cross section when ignoring a possible contribution of the $\psi(3770)$ resonance. The signal cross-section sensitivity obtained with significance of 5σ is 25 nb with the inclusive reconstruction for the luminosity available during "phase-1" of $\bar{\text{P}}$ANDA ($L = 2 \times 10^{31}$ cm^{-2} s^{-1}). This value agrees with the values calculated from the theoretical models shown in section 2.3. For the exclusive reconstruction and the same signal cross-section value the significance obtained is much less than 1σ (see figure 5.27). In addition to that, the contribution of the STT to the PID was also studied. The results have shown that for the specific D-meson decay, the STT will not play an important role, since most of the final-state particles have high momenta. In contrast, the DIRC detectors are the most effective PID detectors for the studied channel (see figure 5.12). If one wants to examine the contribution of the STT to the

PID, D-meson decays with higher final-state multiplicity are more suitable (e.g. decay to $K_s\pi^+\pi^-$).

The analysis of the production and decay $\bar{p}\,p \rightarrow D^0\,\overline{D}^0 \rightarrow \pi^+K^-\pi^-K^+$ and the calculation of the FOM have shown that in this specific physics channel, the inclusive reconstruction is the most favorable procedure to measure the production cross section. The high efficiency of this way of reconstruction seems to be the key element to reach the statistical significance we aim to have. Even though the exclusive analysis reaches a higher background suppression, it suffers from the very low efficiency (of the order of 7%). In order to study the dynamics of the process and the possible coupling of resonances, it is also very important to study the angular distributions. This would imply that one needs to measure the cross section as a function of angle, and hence, it would require more statistics. The study of different decays of the D mesons will also improve our knowledge about the capabilities of $\bar{\text{P}}$ANDA in the "phase-1" mode. Moreover, a more systematic study on the cuts and the fits applied could probably improve the existing results. Last but not least, the study of the same decay with a higher antiproton momentum should be performed, since one can then reach the production threshold of the $\psi(3770)$ resonance where the cross section is expected to be much higher. However, the mass and momentum resolution should be investigated in that case, as it is expected to be worse than when choosing a momentum that is just slightly above the D-meson production threshold.

Nederlandse Samenvatting

Minstens 2500 jaar geleden begon de mensheid vragen te stellen over hoe de natuur werkt en in elkaar zit. Tot zo ongeveer 50 jaar geleden werden protonen, neutronen en elektronen gezien als de meest fundamentele deeltjes in ons universum. Er was toen echter een groot verschil tussen de observaties en het begrijpen van de natuur. Mede hierom werden quarks ingevoerd als kleinste massadragende bouwsteen van materie. Dit was het moment voor het tot stand brengen en ontwikkelen van een theorie die alle elementaire deeltjes en hun interacties in ons universum beschrijft: het Standaard Model (SM). Het SM is zeer succesvol in het beschrijven van veel fysische fenomenen, in het bijzonder bij zeer hoge energieën dat overeenkomt met systemen veel kleiner dan de grootte van het proton. Echter, het SM geeft een beperkt inzicht in het beschrijven en doorgronden van deeltjes, zoals het proton, die zijn opgebouwd uit elementaire bouwstenen (quarks en gluonen) en onderhevig aan de zogenaamde sterke wisselwerking. Om deze systemen te kunnen interpreteren en hier theorieën voor te formuleren is het nodig om uitgebreide experimenten uit te voeren. Op dit moment vinden deze experimenten plaats in grootschalige opstellingen met geavanceerde apparatuur die in staat zijn om deeltjes te detecteren, hun eigenschappen en processen te bestuderen en ons uiteindelijk helpen om de natuur om ons heen beter te begrijpen.

Het "antiProton ANnihilation in Darmstadt" ($\bar{\text{P}}$ANDA) experiment, die in Darmstadt, Duitsland, wordt geplaatst is een grensverleggend experiment voor hadron fysica. Het is onderdeel van de grotere Faciliteit voor Antiproton en Ion Onderzoek (FAIR) die een breed scala aan fysische experimenten zal faciliteren. De focus van het $\bar{\text{P}}$ANDA experiment is hadron fysica, met als doel antwoorden te geven op de vele vragen over sterke interacties en de fysica zoals beschreven door kwantumchromodynamica (QCD). Het experiment zal gebruik maken van botsingen tussen antiprotonen en protonen of ionen met een maximale massamiddelpuntsenergie van 5.5 GeV. De energiebereik geeft toegang tot het produceren van hadronen met een "charm" vrijheidsgraad. Open-charm mesonen, een charm quark is gebonden aan een lichte (up, down of strange)

quark, zijn bijzonder interessant. Een brede scala van dit soort toestanden zijn experimenteel ontdekt of theoretisch voorspeld, maar vele zijn voorspeld en nog niet gevonden in het experiment of vice versa. Bovendien zijn er nog veel onbeantwoorde vragen over de dynamica van zulke systemen, hun geëxciteerde toestanden en hun massa's en levensduur. $\bar{\text{P}}$ANDA zal een overvloed aan open-charm toestanden kunnen produceren die, samen met het geavanceerde detector systeem en de hoge resolutie van de straal antiprotonen, uitgebreide en precieze metingen mogelijk maken.

Het $\bar{\text{P}}$ANDA experiment bestaat uit verschillende subdetectoren. Elke subdetector speelt een belangrijke rol in het detecteren van de relevante eigenschappen van een botsing. Een van de onderdelen van PANDA zijn de zogenaamde baandetectoren, welke de afgelegde baan van geladen deeltjes in een magnetisch veld zullen reconstrueren. De prestatie van dit type detector speelt een centrale rol in dit proefschrift. De Straw Tube Tracker (STT), een cilindervormige detector bestaande uit buizen gevuld met gas, zal één van de belangrijkste baandetectoren zijn. De STT zal het interactiepunt omringen en zijn hoofdtaken zijn baanreconstructie van geladen deeltjes en het identificeren van het type deeltje (PID). In het energiebereik waarin $\bar{\text{P}}$ANDA zal werken zullen de fysisch interessante processen sterk met elkaar vermengd zijn met een groot aantal achtergrond processen, omdat ze in veel opzichten vergelijkbaar met elkaar zijn. Hierom is het vermogen om het signaal te filteren van deze enorme achtergrond van cruciaal belang.

Het Institut für KernPhysik (IKP) of Forschungszentrum Jülich (FZJ) en de Akademia Gorniczo Hutnicza University in Krakow (AGH) hebben hun krachten gebundeld en een prototype STT gebouwd. Een rechthoekige prototype is langs de antiprotonenstraal geplaatst en bestaat uit 144 afzonderlijke buizen, geordend in 6 lagen met elk 24 buizen. Twee series testen zijn uitgevoerd, één met een protonenstraal met een impuls 0.55, 0.75, 1 en 2.95 GeV/c en de ander met een deuteronenstraal met een impuls van 0.6, 0.75, 1.5 GeV/c. Een toepassingsspecifiek geïntegreerd circuit (ASIC) is gebruikt voor de uitlezing tijdens de tests. De tijd-over-drempelwaarde (TOT) techniek is gebruikt om het energieverlies in de buizen met behulp van de signaalbreedte te meten voor PID. De beste waarde verkregen door ruimtelijke resolutie was 170 μm voor de 0.75 GeV/c deuteronenstraal. Deze waarde is 10% meer dan de verwachte waarde (150 μm) verkregen door simulaties. Om de PID bekwaamheid van de prototype STT te testen is de scheidingskracht gebruikt. De scheidingskracht gemeten tussen protonen en deuteronen was 6.3 voor een impuls van 0.75 GeV/c. Deze waarde ligt heel dichtbij de gesimuleerde waarde wanneer deze wordt vergeleken met de 0.375 GeV/c impuls tussen kaonen en protonen.

De haalbaarheid van $\bar{\text{P}}$ANDA voor open-charm mesonen via het kanaal $\bar{p}\,p \rightarrow D^0\,\overline{D}^0 \rightarrow \pi^+ K^- \pi^- K^+$ is ook onderzocht. Het doel was om te bepalen hoe goed $\bar{\text{P}}$ANDA van deze toestanden de massa en energieresolutie zou kunnen meten, terwijl tegelijkertijd werd gekeken hoe goed deze toestanden gescheiden kunnen worden van de enorme hoeveelheid achtergrond afkomstig van de $\bar{p}p$-botsing. Voor het laatste hebben we een "Figure-Of-Merit" (FOM) gebruikt om de statistische significantie te beoordelen. Bij een 5σ statistische significantie kunnen we degelijke conclusies trekken uit onze metingen. De reconstructie van de data is op twee verschillende manieren uitgevoerd, inclusief (één D meson gereconstrueerd) en exclusief (beide D mesonen gereconstrueerd). De verkregen massaresoluties zijn 2.1 MeV/c^2 voor de inclusieve reconstructie en 1.8 MeV/c^2 voor de exclusieve reconstructie. De bijbehorende efficiënties zijn respectievelijk 26.8% en 7.1%. In het geval van een inclusieve analyse en met de "phase-1" helderheid van $\bar{\text{P}}$ANDA ($L = 2 \times 10^{31}$ cm^{-2} s^{-1}) is de bereikte gevoeligheid van de werkzame doorsnede van het signaal 25 nb bij een 5σ significantie. De bijdrage van de STT aan de PID is ook onderzocht en liet zien dat voor het specifieke kanaal de STT geen belangrijke rol speelt (in tegenstelling tot de DIRC die de voornaamste bron is voor de PID) omdat de meeste eindtoestand-deeltjes een grote impuls hebben. Aan de andere kant zal de STT significant bijdragen aan de PID voor D meson verval met hogere multipliciteit in de eindtoestand.

List of abbreviations

ADC Analog-to-Digital Convertion

AGH Akademia Gorniczo Hutnicza

APPA Atomic Plasma Physics and Applications

ASIC Application-Specific-Integrated Circuit

BEMC Barrel ElectroMagnetic Calorimeter

BESIII BEijing Spectrometer III

BG Box Generator

BTOF Barrel Time-Of-Flight

CB Concentrator Board

CBM Compressed Baryonic Matter

COSY COoler SYnchotron

CR Collector Ring

DAQ Data Acquisition

DB Digital Board

DIRC Detection of Internally-Reflected-Cherenkov light

DPM Dual Parton Model

DWBA Distorted Wave Born Approximation

EFT Effective Field Theory

EvtGen Event Generator

EWT ElectroWeak Theory

FAIR Facility for Antiproton and Ion Research

FEE Front-End Electronics

FEMC Forward ElectroMagnetic Calorimeter

FMS Forward Muon System

FOM Figure-Of-Merit

FPGA Field-Programmable-Gate Array

FTOF Forward Time-Of-Flight

FTS Forward Tracking System

FWHM Full-Width-at-Half-Maximum

FZJ Forschungszentrum Jülich

GDA Generalised Distribution Amplitudes

GEANT3 Geometry and Tracking v3

GEANT4 Geometry and Tracking v4

GEM Gas Electron Multiplier

GPD General Parton Distributions

GSI GSI Helmholtz Center for Heavy Ion Research

HESR High Energy Storage Ring

HL High-Luminosity

HR High-Resolution

HV-MAPS High-Voltage-Monolithic-Active-Pixel Sensors

IKP Institut für KernPhysik

LHC Large Hadron Collider

LMD Luminosity Detector

LQCD Lattice Quantum ChromoDynamics

LVDS Low-Voltage-Differential-Signaling

MC Monte Carlo

MDT Mini-Drift Tubes

MVD Micro Vertex Detector

NUSTAR Nuclear Structure Astrophysics and Reactions

p-LINAC Proton LInear ACcelerator

PANDA antiProton ANnihilation in DArmstadt

PASTTRECv1 PAnda-STT-REadout-Chip-v1

PDG Particle Data Group

PID Particle IDentification

QCD Quantum ChromoDynamics

RICH Ring Imaging Cherenkov

SM Standard Model

SODA Synchronization-Of-Data Acquisition

STT Straw Tube Tracker

TDC Time-to-Digital Convertion

TOT Time-Over-Threshold

TRB Time-Readout Board

UNILAC UNIversal Linear ACcelerator

UrQMD Ultrarelativistic Quantum Molecular Dynamics

List of Figures

List of Tables

Bibliography

[1] S. Godfrey and N. Isgur. Mesons in a relativized quark model with chromodynamics. *Phys. Rev. D 32, 189*, 1985.

[2] M. Di Pierro and E. Eichten. Excited heavy-light systems and hadronic transitions. *Phys. Rev. D 64, 114*, 2001.

[3] P. Gianotti. Results and perspectives in hadron spectroscopy. *Phys. Scr. T150*, 2012.

[4] F. Englert and R. Brout. Broken symmetry and the mass of gauge vector mesons. *Phys. Rev. Lett. 13, 321*, 1964.

[5] P. W. Higgs. Broken symmetries and the masses of gauge bosons. *Phys. Rev. Lett. 13, 508*, 1964.

[6] G. S. Guralnik C. R. Hagen and T. W. Kibble. Global conservation laws and massless particles. *Phys. Rev. Lett. 13, 585*, 1964.

[7] The ATLAS collaboration. Observation of a new particle in the search for the standard model higgs boson with the ATLAS detector at the LHC. *Phys. Lett. B 716, 1*, 2012.

[8] The CMS collaboration. Observation of a new boson at a mass of 125 GeV with the CMS experiment at the LHC. *Phys. Lett. B 716, 30*, 2012.

[9] The ATLAS collaboration. Evidence for the spin-0 nature of the higgs boson using ATLAS data. *Phys. Lett. B 726, 120*, 2013.

[10] D. J. Gross and F. Wilczek. Ultraviolet behavior of non-abelian gauge theories. *Phys. Rev. Lett. 30, 1343*, 1973.

[11] D. J. Gross and F. Wilczek. Asymptotically free gauge theories I. *Phys. Rev. D 8, 3633*, 1973.

[12] D. J. Gross and F. Wilczek. Asymptotically free gauge theories II. *Phys. Rev. D. 9, 980*, 1974.

[13] H. D. Politzer. Reliable perturbative results for strong interactions. *Phys. Rev. Lett. 30, 1346*, 1973.

[14] C. Amsler et al. Review of particle physics. *Chin. Phys. C 38, 090001*, 2014.

[15] B. Holzenkamp K. Holinde and J. Speth. A meson exchange model for the hyperon-nucleon interaction. *Nucl. Phys. A 500, 485*, 1989.

[16] T. Hippchen J. Haidenbauer K. Holinde and V. Mull. Meson-baryon dynamics in the nucleon-antinucleon system: I. The nucleon-antinucleon interaction. *Phys. Rev. C 44, 4*, 1991.

[17] J. Haidenbauer K. Holinde T. Hippchen and V. Mull. Meson-baryon dynamics in the nucleon-antinucleon system: II. Annihilation into two mesons. *Phys. Rev. C 44, 4*, 1991.

[18] J. Haidenbauer. Reaction $p\bar{p} \to \bar{\Lambda}\Lambda$ in the meson exchange picture. *Phys. Rev. C 45, 3*, 1992.

[19] V. Mull and K. Holinde. Combined description of $N\bar{N}$ scattering and annihilation with a hadronic model. *Phys. Rev. C 51, 5*, 1995.

[20] J. Haidenbauer W. Melnitchouk and J. Speth. Meson-exchange model for the YN interaction. *Nucl. Phys. A 663, 549*, 2000.

[21] J. Haidenbauer and G. Krein. The reaction $p\bar{p} \to \bar{\Lambda}_c^- \Lambda_c^+$ close to threshold. *Phys. Lett. B 687, 314*, 2010.

[22] J. Haidenbauer and G. Krein. Production of charmed pseudoscalar mesons in antiproton-proton annihilation. *Phys. Rev. D 64, 114003*, 2014.

[23] R. Machleidt K. Holinde and Ch. Elster. The Bonn meson-exchange model for the nucleon-nucleon interaction. *Phys. Rep. 149, 1*, 1987.

[24] J. Haidenbauer K. Holinde and M. B. Johnson. Folded-diagram nucleon-nucleon potential for application to the many-body problem. *Phys. Rev. C 45, 2055*, 1992.

[25] J. Haidenbauer and G. Krein. The $\psi(3770)$ resonance and its production in $p\bar{p} \to D\bar{D}$. *Phys. Rev. D 91, 114022*, 2015.

[26] A. Khodjamirian Ch. Klein Th. Mannel and Y. M. Wang. How much charm can $\bar{P}$ANDA produce. *Eur. Phys. Jour. 48, 31*, 2012.

[27] K. G. Wilson. Confinement of quarks. *Phys. Rev. D 10, 2445*, 1974.

[28] C. Davies. Lattice QCD. *arXiv:0205181 [hep-ph]*, 2002.

[29] J. van der Heide. The pion form factor from lattice QCD. *PhD thesis, University of Amsterdam*, 2004.

[30] G. K. C. Cheung et al. Excited and exotic charmonium, D_s and D meson spectra for two light quark masses from lattice QCD. *arXiv:1610.01073 [hep-lat]*, 2017.

[31] C. Patrignani and others (Particle Data Group). The review of particle physics. `http://pdg.lbl.gov/`, 2017.

[32] J. Dudek et al. Toward the excited meson spectrum of dynamical QCD. *arXiv:1004.4930 [hep-lat]*, 2010.

[33] L. Liu et al. Excited and exotic charmonium spectroscopy from lattice QCD. *arXiv:1204.5425 [hep-lat]*, 2012.

[34] Institute of High Energy Physics (IHEP). The BESIII experiment. `http://bes3.ihep.ac.cn/`, 2017.

[35] The $\bar{\text{P}}$ANDA collaboration. Physics performance report for: $\bar{\text{P}}$ANDA strong interaction studies with antiprotons. *arXiv:0903.3905 [hep-ex]*, 2009.

[36] The $\bar{\text{P}}$ANDA collaboration. Technical progress report for: $\bar{\text{P}}$ANDA strong interaction studies with antiprotons. `http://www-panda.gsi.de/archive/public/panda_tpr.pdf`, February 2005.

[37] The BaBar collaboration. Observation of a narrow meson state decaying to $D_s^+\pi^0$ at a mass of 2.32 GeV/c^2. *Phys. Rev. Lett. 90, 242*, 2003.

[38] N. Isgur R. Kokoski and J. Paton. Gluonic excitations of mesons: Why they are missing and how to find them. *Phys. Rev. Lett. 54, 869*, 1985.

[39] J. Aubert et al. Experimental observation of a heavy particle J. *Phys. Rev Lett. 33, 1404*, 1974.

[40] J. Augustin et al. Discovery of a narrow resonance in e^+e^- annihilation. *Phys. Rev. Lett. 33, 1406*, 1974.

[41] J. Messchendorp for the BESIII collaboration. Physics with charmonium - A few recent highlights of BESIII. *arXiv:1306.6611 [hep-ex]*, 2013.

[42] The BES collaboration. Measurements of the mass and full-width of the η_c meson. *Phys. Lett. B 555, 174*, 2003.

[43] The BaBar collaboration. Measurements of the mass and width of the η_c meson and of an $\eta_c(2S)$ candidate. *Phys. Rev. Lett. 92, 142*, 2004.

[44] I. Zychor et al. Evidence for an excited hyperon state in pp $\rightarrow$ K^+Y^{0*}. *Phys. Rev. Lett. 96, 012002*, 2006.

[45] M. I. Adamovich et al. Observation of a resonance in the K_sp decay channel at a mass of 1765 MeV/c^2. *Eur. Phys. Jour. C 50, 535*, 2007.

[46] S. L. Olsen. QCD exotics. *arXiv:1403.1254 [hep-ex]*, 2014.

[47] D. Thompson et al. Evidence for exotic meson production in the reaction π^-p $\rightarrow$ $\eta\pi^-$p at 18 GeV/c. *Phys. Rev. Lett. 79, 1630*, 1997.

[48] G. Adams et al. Observation of a new $J^{PC} = 1^{-+}$ exotic state in the reaction π^-p $\rightarrow$ $\pi^-\pi^-\pi^+$p at 18 GeV/c. *Phys. Rev. Lett. 81, 5760*, 1998.

[49] A. Abele et al. Exotic $\eta\pi$ state in $\bar{p}$d annihilation at rest into $\pi^-\pi^0\eta p_{spectator}$. *Phys. Lett. B 423, 175*, 1998.

[50] J. Reinnarth et al. Evidence for an exotic partial wave in $\pi\eta'$. *Nucl. Phys. A 692, 268*, 2001.

[51] C. Amsler et al. $\eta\eta'$ threshold enhancement in antiproton proton annihilations into $\pi^0\eta\eta'$ at rest. *Phys. Lett. B 340, 259*, 1994.

[52] C. Amsler et al. A high-statistics study of $f_0(1500)$ decay into $\pi^0\pi^0$. *Phys. Lett. B 342, 433*, 1995.

[53] C. Amsler et al. Coupled channel analysis of antiproton proton annihilation into $\pi^0\pi^0\pi^0$, $\pi^0\pi^0\eta$, $\pi^0\eta\eta$. *Phys. Lett. B 353, 571*, 1995.

[54] C. Amsler et al. Observation of $f_0(1500)$ decay into K_LK_L. *Phys. Lett. B 385, 425*, 1996.

[55] C. Amsler et al. Study of $f_0(1500)$ decays into four neutral pions. *Eur. Phys. Jour. C 19, 667*, 2001.

[56] C. Morningstar and M. Peardon. Efficient glueball simulations on anisotropic lattices. *Phys. Rev. D 56, 4043*, 1997.

[57] C. Morningstar and M. Peardon. Glueball spectrum from an anisotropic lattice study. *Phys. Rev. D 60, 034509*, 1999.

[58] M. Danysz and J. Pniewski. Delayed disintegration of a heavy nuclear fragment. *Phil. Mag. 44, 348*, 1953.

[59] M. Danysz et al. The identification of a double hyperfragment. *Nucl. Phys. A 49, 121*, 1963.

[60] A. Sanchez Lorente. Hypernuclear physics studies of the $\bar{P}$ANDA experiment at FAIR. *Hyperfine Interact. 229, 45*, 2014.

[61] K. Suzuki et al. Precision spectroscopy of pionic 1s states of Sn nuclei and evidence for partial restoration of chiral symmetry in the nuclear medium. *Phys. Rev. Lett. 92, 072302*, 2004.

[62] J. G. Messchendorp et al. In-medium modifications of the $\pi\pi$ interaction in photon-induced reactions. *Phys. Rev. Lett. 89, 222302*, 2002.

[63] R. Barth et al. Subthreshold production of kaons and antikaons in nucleus-nucleus collisions at equivalent beam energies. *Phys. Rev. Lett. 78, 4007*, 1997.

[64] F. Laue et al. Medium effects in kaon and antikaon production in nuclear collisions at subthreshold beam energies. *Phys. Rev. Lett. 82, 1640*, 1999.

[65] F. Klingl et al. Masses of J/ψ and η_c in the nuclear medium: QCD sum rule approach. *Phys. Rev. Lett. 82, 3396*, 1999.

[66] Y. Golubeva et al. In-medium spectral functions of charmonia studied by $\bar{\text{p}}$A reactions. *Eur. Phys. Jour. A 17, 275*, 2003.

[67] A. Sibirtsev et al. On studying charm in nuclei through antiproton annihilation. *Eur. Phys. Jour. A 6, 351*, 1999.

[68] The $\bar{\text{P}}$ANDA collaboration. Technical design report for: $\bar{\text{P}}$ANDA straw tube tracker. *Eur. Phys. Jour. A 49, 2*, 2013.

[69] The $\bar{\text{P}}$ANDA collaboration. Technical design report for: $\bar{\text{P}}$ANDA internal targets: The cluster-jet target and the developments for the pellet target. `http://www-panda.gsi.de/archive/TargetTDR/Targets_TDR.pdf`, March 2012.

[70] P. Wintz. A large tracking detector in vacuum consisting of self-supporting straw tubes. *AIP Conference Proceedings 698, 789*, 2004.

[71] The $\bar{\text{P}}$ANDA collaboration. Technical design report for: $\bar{\text{P}}$ANDA micro vertex detector. *arXiv:1207.6581 [physics.ins-det]*, 2012.

[72] O. Merle et al. Development of an endcap DIRC for $\bar{\text{P}}$ANDA. *Nucl. Instrum. Meth. A766, 96*, 2014.

[73] G. Kalicy et al. Status of the $\bar{\text{P}}$ANDA Barrel DIRC. *JINST, Volume 9, C05060*, 2014.

[74] The $\bar{\text{P}}$ANDA collaboration. Technical design report for: $\bar{\text{P}}$ANDA electromagnetic calorimeter. *arXiv:0810.1216 [physics.ins-det]*, 2008.

[75] D. A. Bremer et al. Performance of prototypes for the $\bar{\text{P}}$ANDA barrel EMC. *Jour. of Phys.: Conf. Ser. 587, 012052*, 2015.

[76] A. Herten. GPU-based online track reconstruction for $\bar{\text{P}}$ANDA and application to the analysis of $\text{D} \to \text{K}\pi\pi$. *PhD thesis, Ruhr University of Bochum*, 2015.

[77] The $\bar{\text{P}}$ANDA collaboration. Technical design report for: $\bar{\text{P}}$ANDA muon system. `http://www-panda.gsi.de/archive/MuonTDR/Muon_TDR.pdf`, September 2012.

[78] The $\bar{\text{P}}$ANDA collaboration. Technical design report for: $\bar{\text{P}}$ANDA luminosity detector (*In preparation*), 2015.

[79] A. Zambanini. Development of a free-running readout ASIC for the $\bar{\text{P}}$ANDA micro vertex detector and investigation of the performance to reconstruct $\text{p}\bar{\text{p}} \to \Xi^+\Xi^-(1690)$. *PhD thesis, Ruhr University of Bochum*, 2015.

[80] I. Konorov et al. SODA - time distribution system for the $\bar{\text{P}}$ANDA experiment. *Nucl. Sc. Symp. IEEE Transactions, 1863*, 2009.

[81] M. Al-Turany et al. The fairroot framework. *Jour. of Phys.: Conf. Ser. 396, 022001*, 2012.

[82] R. Brun and F. Rademarkers. ROOT — an object oriented data analysis framework. *Nucl. Instrum. Meth. A389, 81*, 1997.

[83] S. Spataro for the $\bar{\text{P}}$ANDA collaboration. The pandaroot framework for simulation, reconstruction and analysis. *Jour. of Phys.: Conf. Ser. 331, 032031*, 2011.

[84] D. J. Lange. The EvtGen particle decay simulation package. *Nucl. Instrum. Meth. A462, 152*, 2001.

[85] A. Capella et al. Dual parton model. *Phys. Rep. 236, 225*, 1994.

[86] S. A. Bass. Microscopic models for ultrarelativistic heavy ion collisions. *Prog. in Part. and Nucl. Phys. 41, 255*, 1998.

[87] J. Allison et al. Geant4 developments and applications. *Nucl. Sc. Symp. IEEE Transactions, 270*, 2006.

[88] J. Rauch and T. Schluter. GENFIT: a generic track-fitting toolkit. *Jour. of Phys.: Conf. Ser. 608, 012042*, 2015.

[89] A. Fontana et al. Use of GEANE for tracking in virtual monte carlo. *Jour. of Phys.: Conf. Ser. 119, 032018*, 2008.

[90] FAIR – Facility for Antiproton and Ion Research. The modularized start version. http://www.fair-center.eu/fileadmin/fair/publications_FAIR/FAIR_GreenPaper_2009.pdf, October 2009.

[91] GSI – Helmholtzzentrum für Schwerionenforschung. The FAIR complex. http://www.fair-center.eu, 2017.

[92] FAIR – Facility for Antiproton and Ion Research. FAIR baseline technical report. http://www.fair-center.eu/for-users/publications/fair-publications.html, September 2006.

[93] FAIR – Collector Ring Working Group. Technical design report on the collector ring. http://indico.gsi.de/event/2200/material/slides/7.pdf, November 2013.

[94] GSI – Helmholtzzentrum für Schwerionenforschung. Technical report of subproject HESR. http://www.gsi.de/fair/reports/btr-e.html, 2006.

[95] R. Toelle et al. HESR at FAIR: Status of technical planning. In *Proceedings of PAC07, New Mexico, USA, 1442*, 2007.

[96] H. Stockhorst et al. Stochastic cooling developments for the HESR at FAIR. In *Proceedings of EPAC08, Genoa, Italy, 3490*, 2008.

[97] D. Reistad et al. Calculations on high energy electron cooling in the HESR. In *Proceedings of COOL07, Bad Kreuznach, Germany, 44*, 2007.

[98] P. Strzempek. Development and evaluation of a signal analysis and a readout system of straw tube detectors for the $\bar{\text{P}}$ANDA spectrometer. *PhD thesis, Jagiellonian University Krakow*, 2016.

[99] T. Akesson et al. Particle identification using the time over threshold method in the ATLAS transition radiator tracker. *Nucl. Instrum. Meth. A474, 172*, 2001.

[100] D. Przyborowski et al. Development of a dedicated front-end electronics for straw tube trackers in the $\bar{\text{P}}$ANDA experiment. *JINST, Volume 11, P08009*, 2016.

[101] A. Neiser et al. TRB3: a 264 channel high precision TDC platform and its applications. *JINST, Volume 8, C12043*, 2013.

[102] P. Strzempek. $\bar{\text{P}}$ANDA straw tube detectors and readout. *Nucl. Instrum. Meth. A824, 359*, 2016.

[103] P. Strzempek. Straw Tube Tracker readout and FT performance in april beam time. In *STT Readout Workshop, Krakow*, 2017.

[104] P. Avery. Kinematic fitting algorithms and lessons learned from KWFIT. In *Proceedings of CHEP2000, Padua, Italy, 135*, 2000.

Acknowledgements

As many people are aware of, I am not the usual normal person, especially when it comes to rules or standards. That's why I will start by thanking my family first.

Lary, my beloved father, you left us early so you didn't get the chance to see me become a doctor. I will always thank you for everything you did for me, your support, advice and kindness. I hope you are proud of me.

Mother, thank you for your strength, love, and support especially during the hard times we had. Thank you for the so many hours of Skype spent together. You are the foundations of our family.

Brother you know I do not have to say much for you. You are the best brother I could have wished. If I start describing all the moments we have shared together, this thesis will never end. Thanks Mpampi.

Matina, my other half in this life. Thank you for your support, patience and smile during all these years we are in the Netherlands. Without you, it would be impossible for me to be at this position now.

Giannis, Chara, Christiana, thank you for your support, love and the many hours spent talking on Skype. You are my second family.

Chara, Maria, Stefania, Argyrw, Wana, Argyri, Wasili, Stavro thank you for everything that you have done for me and Matina. You are really good friends and you have made our lives in the Netherlands easier and nicer.

Thanks to all my friends and relatives in Greece. Each of you have supported me through this very demanding period of my life.

Λάρυ, πολυαγαπημένε μου πατέρα, μας άφησες νωρίς και δεν είχες την ευκαιρία να με δεις να γίνομαι ένας δόκτωρας. Θα σε ευγνωμονώ πάντοτε για όλα όσα έκανες για μένα, για την στήριξη, τις συμβουλές και την ευγένεια σου. Ελπίζω να είσαι περήφανος για μένα.

Μητέρα, σε ευχαριστώ για την δύναμη, την αγάπη και την υποστήριξη σου, ιδιαίτερα κατά την διάρκεια των δύσκολων στιγμών που περάσαμε. Σε ευχαριστώ και για τις τόσες πολλές ώρες που περάσαμε μαζί στο Σκάιπ. Είσαι τα θεμέλια της οικογένειας μας.

Αδερφέ, ξέρεις ότι δεν πρέπει να πω πολλά για σένα. Είσαι ο καλύτερος αδερφός που θα μπορούσα να έχω. Αν αρχίσω να περιγράφω τις στιγμές που έχουμε περάσει μαζί, δεν θα τελειώσει ποτέ αυτή η διδακτορική διατριβή. Ευχαριστώ Μπάμπι.

Ματίνα, το άλλο μου μισό στην ζωή. Σε ευχαριστώ για την στήριξη, την υπομονή και το χαμόγελο σου όλα αυτά τα χρόνια που είμαστε στην Ολλανδία. Χωρίς εσένα θα ήταν απίθανο για μένα να βρίσκομαι εδώ που είμαι σήμερα. Σε αγαπώ Ματινέλα.

Κύριε Γιάννη, κυρία Χαρά, Χριστιάνα, σας ευχαριστώ για την στήριξη και την αγάπη σας. Είστε η δεύτερη μου οικογένεια.

Χαρά, Μαρία, Στεφανία, Αργυρώ, Βάνα, Αργύρη, Βασίλη, Σταύρο, σας ευχαριστώ για όλα όσα έχετε κάνει για μένα. Είστε πολύ καλοί φίλοι σε μένα και την Ματίνα. Κάνετε την ζωή μας στην Ολλανδία ευκολότερη και ομορφότερη.

Ευχαριστώ όλους τους φίλους και συγγενείς μου στη Ελλάδα. Ο κάθε ένας από εσάς με βοήθησε και με στήριξε κατά την διάρκεια της απαιτητικής αυτής περιόδου της ζωής μου.

Nasser, there are not enough words to express my gratitude to you. Thanks for everything. Thanks for giving me the opportunity to work at KVI-CART, your supervision, the nice ideas, the whiskey nights, the barbecues etc. I enjoyed our discussions (private or not) about politics. It was a privilege for me to discuss things with you and exchange ideas (I think we agreed on most of things). I hope we can continue our discussions in the future.

Johan, everything I told about Nasser, holds for you too. Thanks for giving me the opportunity to work at KVI-CART and thanks for being such a good supervisor and person. I will not forget our discussions about work, politics and the nice time we had during trips, barbecues, whiskey nights etc. I have become a better person thanks to you. I will always admire your bright mind and your opinion on many subjects (on most of them we agreed, I think). I really hope we will keep in touch.

Peter, thank you for your supervision during my time in Germany. I will always remember our fruitful discussions about work. I really enjoyed all the beam times we had together as well as the trips in Poland. Your contribution to my thesis is more than valuable. I will always remember how calm and kind you were at all times.

Jim, you are probably the busiest person I have ever met in my whole life. However, I enjoyed the time during the weekly meetings where you always had nice (or nasty) questions and solutions to everyone's problems. Thank you for the nice time during the barbecue you hosted at your house.

Zahra, you are the best officemate ever. One of the most hard-working and kind persons I have ever met. Thanks for the company in the afternoon breaks, the discussions in our office and the time we spent together outside working hours. I am glad that we are friends and that we will keep seeing each other.

Ali, you are one of the persons I came closer with. Thanks for all the nice talks in my/your office. The coffee breaks in the afternoon, the whiskey nights, the barbecues and many other things that I cannot recall at the moment. Your presence made my time at KVI-CART nicer. We will keep in touch for sure.

Marcel, thanks for everything. You are one of the persons that I really enjoyed to spent time with. Your jokes, comments, and the time we spend together during the $\bar{\text{P}}$ANDA meetings will remain unforgettable to me. I think I can call you my friend too.

Ali and Brankica (my lovely paranymphs), even though you are relatively new to the group, I think we managed to have a nice time together. Thank you for all the funny moments and the company especially during the last months of my Ph.D period. You are both awesome.

Soumya (we had many nice moments together and a lot of fun), Mohammad (Babai, thanks for your help with programming and all the nice moments we shared), Josbert (I will miss the time during lunches), Karol (our amazing barbeque chef), Ikechi (do not drink coctails), Catherine, Myroslav, Julia, Christiaan, Mohammad, Maisam, Solmaz, Reza, Hajar, Brian, Gia, Stefano, Aleksandra, Olaf, Peter, Muhsin, Herbert, Gita, Olga, Olena, Oliver, Roza (special thanks for the dutch summary) thank you all for making my time at KVI-CART unforgettable and for all the nice moments we shared. Each one of you has given me something valuable to take with.

Michael, Artur, Florian, Daniel thank you for everything. You made my time in Germany so easy. Without you, I would have probably asked to leave after a few weeks there. Thank you all for the nice time at work, the darts, the help with any kind of problem.

Michael, my favorite American friend, thanks for all your valuable help, for answering all the questions I asked, for the weekly barbecues or pizzas, the beers, the night out in Cologne, the nice time in Vienna, the dinner at your place with your wonderful family, the Xletix and many more.

Artur, my friend, thanks for all the help. I will never forget the preparations before the beam times, the lunches, the Xletix, the pizzas, the running and for sharing so many moments together. Florian, my working out buddy, thanks for all the afternoons we spent for our daily work out, the help with my work, the dinners at your place. I enjoyed the time in the pub watching football, eating burgers or chicken wings and tasting whiskeys.

Daniel, thanks for sharing your office room for darts. That was awesome. Thanks for your help, the barbecues, the pizzas, the lunch we had at MacDonald's with Michael, the crazy night out in Cologne, the Xletix experience. Thanks buddy.

Harout, Tobias, Frank, Huagen, Lu, Andreas, Andre, Jennifer, Elisabetta, Ludovico, Maria, Alessandra, Albrecht, thank you all for your help, kindness and company. It would be different without you in Germany.

Last but not least, I would like to thank Prof. Ad van der Berg, Prof. Piotr Salabura and Prof. Xiaoyan Shen for reading my thesis and for sending valuable feedback.

I do hope I did not forget anyone. If so, please forgive me. Thank you all again!!